Master's thesis

NTNU
Norwegian University of Science and Technology
Faculty of Natural Sciences
Department of Physics

Annelen Dogger Schmidt

Modeling Susceptibility-induced Magnetic Field Distortion in the Human Head at 7 Tesla Using a Fourier-based Method

Master's thesis in Applied Physics and Mathematics
Supervisor: Johanna Vannesjö
July 2022

NTNU
Norwegian University of
Science and Technology

Annelen Dogger Schmidt

Modeling Susceptibility-induced Magnetic Field Distortion in the Human Head at 7 Tesla Using a Fourier-based Method

Master's thesis in Applied Physics and Mathematics
Supervisor: Johanna Vannesjö
July 2022

Norwegian University of Science and Technology
Faculty of Natural Sciences
Department of Physics

Preface

This master thesis was written in the spring semester of 2022 for the Department of Physics at the Norwegian University of Science and Technology (NTNU). A project report was written during the fall of 2021, which created the basis for the work performed in this master thesis. The method used in the master thesis was initially validated in the project report, where it was tested on geometrical shapes with commutable analytical solutions for the induced field distortions. The method was proven to work for simple geometries and was in the 2022 spring semester tested on humans to study the susceptibility effects.

The original goal of the thesis was to model susceptibility-induced field variations in the neck region. However, since the receiver coil needed for the in vivo measurement of the neck did not arrive in time, the goal was changed to analyze the head region. Throughout the year, I have learned to use new software, including SPM12, and much time has been put into understanding its function and how it can be best used to achieve the aim of the thesis.

I would like to thank my supervisor Johanna Vannesjo and my previous professor, Neil Peter Jerome, for assisting and counseling me throughout this semester. They have supplied me with valuable input in interpreting my results and have helped me in understanding different concepts regarding MR physics. I also want to thank Stefan Sommer from Siemens Healthineers, who gave me the opportunity to use a non-clinical UTE sequence which he has been working on. This made it possible to achieve more accurate air segmentation in this master thesis. Finally, I would like to thank the volunteers for taking their time to be part of my thesis.

Annelen Dogger Schmidt

Trondheim, 04.07.2022

Abstract

Magnetic susceptibility (χ) is an intrinsic property of all materials describing its tendency to become magnetized when placed under a magnetic field. The distribution of tissues with different magnetic susceptibility properties within the human body induces field distortions in MRI, which are typically strong and complex adjacent to abrupt susceptibility interfaces, e.g., air-tissue interfaces. The field distortions are hard to remedy with today's shimming technique, and will generate imaging artifacts, primarily signal loss and geometric distortions. The problem of field homogeneity is magnified in high field MR, as susceptibility-induced magnetic field distortions scale linearly with the magnetic field strength, and are a limiting factor for the theoretical gain of various high field MR applications. The ability to achieve accurate subject-specific B_0 field inhomogeneity using a numerical model can provide valuable insight for the work to minimize susceptibility artifacts through shimming and sequence optimization.

A Fourier-based method was used to rapidly calculate the induced field distortion based on a subject-specific susceptibility distribution of a human head. The subject-specific susceptibility map was attained by automatic segmentation of high-resolution anatomical images and by utilizing the high bone-air contrast of UTE images for further air segmentation. The presence of through-slice field gradients ($G_{z,s}$) was also quantified by a non-linear least-squares fit of the experimental data from a multi-echo gradient-recalled echo scan onto a signal decay function corrected for the presence of $G_{z,s}$. In addition, $G_{z,s}$ was quantified by linear fitting of the experimentally measured field maps and the numerically calculated field offset.

A striking degree of resemblance in shape, extent, and order of magnitude between the simulated and the experimentally measured frequency offset values, was observed in the prefrontal cortex, located above the nasal cavity, and the ethmoid and sphenoid sinuses. The same was observed for the quantified $G_{z,s}$-maps. However, the lack of air segmentation in the temporal bone, tympanic cavity, and parts of the nasal cavity and ethmoid sinuses caused deviations from the experimental measurements in the brain region adjacent to the mentioned air cavities. In addition, significant discrepancies between the numerical model and the experimental measurements were observed at the inferior and superior ends of the brain region, most likely due to the limited jaw, neck, and shoulder segmentation achieved in the subject-specific susceptibility model.

The Fourier-based method was proven to give valuable information in regions with locally strong susceptibility-induced field gradients, but some issues remained. The accuracy of the segmentation step is currently the main limiting factor, but several steps can be taken to improve the achieved segmentation in future work.

Sammendrag

Magnetisk susceptibilitet (χ) er en egenskap som alle materialer innehar og beskriver materiales tendens til å bli magnetisert når det befinner seg i et magnetisk felt. Den varierende fordelingen av magnetisk susceptibilitet i menneskekroppen frembringer feltforstyrrelser under MR avbildning. Magnetiske feltforstyrrelser er vanligvis sterke og komplekse nærme overflater der en brå endring i magnetisk susceptibilitet forekommer, f.eks. ved luft-vev overflater. Et fullsteding homogent felt er vanskelig å oppnå for in vivo målinger med dagens shimming-teknikk, og de gjenværende feltforstyrrelsene kan frembringe bildeartifakter, primært signaltap og geometriske forvregninger i det rekonstruerte bildet. Feltforstyrrelser grunnet forskjeller i magnetisk susceptibilitet er forsterket i høyfelts MR, da effekten stiger lineært med feltstyrken. Å beregne disse feltforstyrrelsene grunnet en magnetisk susceptibilitetsfordeling kan gi verdifull informasjon som kan brukes i videreutvikling av shimming-teknikken og bruk av sekvensparametere for å minimalisere tilstedeværelsen av bildeartifakter som oppstår grunnet induserte feltforstyrrelser.

En Fourier-basert metode ble brukt til å raskt kalkulere de induserte feltforstyrrelsene basert på en spesifikk susceptibilitetsfordeling til et menneskehode. Susceptibilitetsfordelingen for personen som blir avbildet, ble anskaffet gjennom automatisk segmentering av anatomiske bilder, og ved å bruke UTE bilder med høy bein-luft kontrast for videre luftsegmentering. Feltgradienter gjennom bilde-planet ($G_{z,s}$) ble kvantisert ved bruk av ikke-lineær minste kvadraters metode. En korrigert funksjon som beskriver signalforløpet hvor tilstedeværelsen av $G_{z,s}$ er tatt hensyn til, ble brukt som modell i tilpasningen av den eksperimentelle dataen oppnådd fra en multi-ekko gradient-ekko sekvens. $G_{z,s}$ ble også estimert ved lineær approksimasjon av feltkartet oppnådd ved eksperimentelle målinger og ved bruk av den numeriske modellen.

En overbevisende grad av likhet i form, utstrekning og størrelsesorden mellom de simulerte og de eksperimentelt målte frekvensforstyrrelsene ble observert i prefrontal cortex, lokalisert over nesegangene, og bihulene etmoid og sphenoid. Det samme ble observert for kartene over kvantiserte $G_{z,s}$ verdier. Mangel på luftsegmentering i temporalbeinet, øregangene og deler av nesegangene og etmoid bihulene, forårsaket avvik fra de eksperimentelle målingene i områder av hjernen nærliggende de gitte lufthullene. I tillegg ble det observert betydelige avvik i den nedre og øvre delen av hjernen mellom resultatene av den numeriske modellen, mest sannsynlig på grunn av begrenset kjeve-, nakke- og skuldersegmentering.

Den Fourier-baserte metoden ble vist til å kunne gi verdifull informasjon om lokale feltforstyrrelser som finner sted i deler av menneskehjernen under MR avbildning, men noen begrensninger i de oppnådde resultatene gjenstår. Nøyaktigheten av segmenteringstrinnet er for øyeblikket den viktigste begrensende faktoren, men flere tiltak kan bli tatt for å forbedre den oppnådde segmenteringen i fremtiden.

Table of Contents

Chapter 1

Introduction

Magnetic resonance imaging (MRI) is a non-invasive imaging technique that exploits a nucleus's magnetic property, mainly the hydrogen nucleus (proton), to generate images. MRI has superior soft-tissue contrast compared to other imaging modalities, e.g., CT, and it has the possibility to image changes in the metabolic processes giving functional information about the tissues. The interaction between the nuclear magnetic moment and an applied magnetic field, B_0, gives rise to a nuclear resonance phenomenon that can be utilized to generate radio-frequency signals. The emitted MR signal from the object is spatially encoded and localized by employing time-varying spatially linear gradients in each orthogonal direction, giving a linear relationship between the local field strength and the position of the precessing nucleus along the direction of the gradient. The MR signal acquisition mechanism assumes that the applied background field is spatially homogeneous and that the spatial encoding gradients are linear.

The homogeneity of the applied background magnetic field in an MR machine becomes distorted when a subject is placed within the scanner due to the magnetization of the tissues. A material's tendency to become magnetized when exposed to a magnetic field is described by magnetic susceptibility (χ), which is a fundamental property of a material (A.D. Elster and J.H. Burdette 2001). χ can be either positive (paramagnetic) or negative (diamagnetic), depending on if the induced magnetization of the tissue aligns or opposes the direction of the applied magnetizing field. The human body consists of a distribution of tissues with different magnetic susceptibilities, where most of the human tissues are diamagnetic with χ-values similar to that of water (Marques and Bowtell 2005). However, the human body is surrounded by air, which has a weak paramagnetic susceptibility value and embodies internal air cavities, causing interfaces between soft tissues and air. The difference in magnetization between the tissues gives rise to locally susceptibility-induced perturbing fields and, thus, causes static field inhomogeneity that is patient-to-patient specific. The field inhomogeneity will be most pronounced at tissue interfaces with an abrupt change in susceptibility value, e.g., air-soft tissue and air-bone interfaces. In addition, iron is a strongly paramagnetic material in the human body that also contributes to strong susceptibility interfaces.

The difference in magnetic susceptibility for biological components can be utilized on a microscopic scale as a source of contrast. Specifically, blood oxygenation level dependent (BOLD) imaging, used to generate functional MR images (fMRI), utilizes the change in magnetic susceptibility between oxygenated and deoxygenated hemoglobin to measure the brain activity of specific parts of the brain by correlating the temporal evolution of the signal change with an applied stimulus (Ogawa et al. 1990). However, as well as being a source of contrast, it is also a dominant source of artifacts in MRI, both on a microscopic and macroscopic scale. The main artifacts caused by the local susceptibility-induced field inhomogeneity are geometric distortion and signal loss. Geometric distortions occur in the reconstructed image when the presence of field distortions induces significant macroscopic field shifts. The induced field shifts disrupt the linearity between position and local field strength defined by the spatial encoding gradients, and the affected nuclei will precess at a different frequency than what is assumed by the MR acquisition mechanism, causing faulty spatial mapping of the MR signal. Signal void is prominent in areas where the local field variations induce intravoxel dephasing of the individual magnetic moments. The artifacts are

prominent at tissue interfaces with an abrupt change in susceptibility value. The magnitude of the field distortions scales linearly with the applied magnetic field (Juchem et al. 2011; Schäfer et al. 2009). The susceptibility-induced field distortions cause limitations in the theoretical gains of MRI, especially in fMRI and high field MR measurements (Juchem et al. 2011). The particularly strong and localized susceptibility artifacts generated at locations near air-tissue interfaces can significantly compromise the detection of neural activation in nearby brain regions, making it difficult to obtain reliable information (Wilson et al. 2002). Problematic brain areas affected by the susceptibility-induced field gradients include the prefrontal cortex and the medial and inferior temporal lobes (Deichmann, Gottfried et al. 2003; Juchem et al. 2011). In addition, for high-field imaging where more minor susceptibility differences are exacerbated, the bone-soft tissue interfaces will also contribute to generating highly variable local field gradients, e.g., around each vertebra in the spine, causing complications in spinal cord imaging.

Techniques to minimize local magnetic field distortion in MRI include shimming and optimizing sequence parameters. Shimming is a process that tries to homogenize the B_0 field. Improving the homogeneity of B_0 will improve both forms of susceptibility artifacts. Active shimming involves generating correcting magnetic fields described by spherical harmonic functions on a patient-to-patient basis. It is applied before imaging by directing current through specific coils localized in the MR machine system. However, today's active shimming design is not able to eliminate the strong and complex variable field distortions, and a residual field inhomogeneity will be present (Juchem et al. 2011). Today, research is largely done on the use of a multi-coil shimming technique (Juchem et al. 2011; Stockmann et al. 2016). The localized shimming technique utilizes a number of individual electrical coils that can emit a set of spherical harmonic basis functions and generates localized gradient field patterns close to the coils (Juchem et al. 2011). Even though the technique has been shown to improve the magnetic field homogeneity significantly, it cannot fully homogenize the entire brain region, and some residual field inhomogeneities will be expected (Juchem et al. 2011). Optimization of sequence parameters can be performed to minimize the signal loss caused by local field variations (Huang et al. 2015). Sequence optimization involves using spin-echo (SE) sequences instead of gradient-recalled echo (GRE) sequences, shortening the echo time (TE) and decreasing the voxel size (Bernstein et al. 2006; Huang et al. 2015). In addition, increasing the receiver bandwidth can be done to minimize the effect of the local magnetic field gradient across the imaging voxels, helping both against signal loss and geometric distortion (Huang et al. 2015). However, sequence parameter optimizations do not come without a cost. Decreasing the voxel dimension or increasing the receiver bandwidth for the equal resolution will reduce the signal-to-noise ratio in the image, and T_2^*-contrast will effectively be lost by shortening TE (Liang and Lauterbur 2000; McRobbie et al. 2017). In addition, there are situations where SE sequences cannot be used instead of GRE sequences to obtain necessary information, e.g., fMRI, which relies on the rapid signal acquisition and the BOLD effect as imaging contrast.

Currently, the presence of field inhomogeneities cannot be entirely eliminated and will cause limitations in the image quality and, thus, the informative value and the theoretical gain in MR, especially for scanners using higher field strengths where the problem is magnified (Juchem et al. 2011). Obtaining a fuller understanding of the characteristics of the induced complex field distortions can help optimize the application of shimming, the shim design, and the sequence parameters to improve the field homogeneity. Especially, it can be proven valuable in the ongoing research about the use of multi-coil shimming techniques. Therefore, a numerical model that simulates the magnitude of the inter-subject induced field distortions is desirable. It has recently been introduced a Fourier-based approach that rapidly simulates the local magnetic field perturbations (Koch et al. 2006; Marques and Bowtell 2005; Schäfer et al. 2009). The model has initially been tested and validated on simple geometrical structures with known analytical solutions for the induced magnetic field variation and has been proven to be computational fast with sufficient accuracy depending on the parameters selected (Schmidt 2021). The aim of this study is to establish a pipeline to yield a detailed and accurate estimate of the local field inhomogeneity in an individual subject, based on the segmentation of anatomical images. The simulation will further be validated by comparing the results to experimentally acquired field maps. In addition, through-plane susceptibility gradients ($G_{z,s}$) will be estimated, both from the results of the model and the acquired field maps, and by fitting experimental data from a multi-echo GRE (ME-GRE) scan onto a $G_{z,s}$-corrected signal decay function.

Chapter 2

Theory

Inspiration from the previously written thesis, Schmidt 2021, are used in most parts of Section 2.1, 2.5 and 2.6. In addition, most of the information used in the basic MR theory section are taken from the books written by Liang and Lauterbur 2000, Brown et al. 1999, Dance et al. 2014, A.D. Elster and J.H. Burdette 2001, McRobbie et al. 2017, and Weishaupt et al. 2008.

2.1 Basic MRI

MRI is a non-invasive diagnostic imaging technique that is preferred over other imaging techniques, e.g., CT, due to the superior soft tissue contrast in MR images. In addition, MRI can obtain functional information about the brain. Instead of using harmful radiation, such as in CT, to produce anatomical images, MRI utilizes a magnetic field. MRI is based on the nuclear magnetic resonance (NMR) phenomenon, arising from the interaction between an applied magnetic field and the magnetic moment of a spinning nucleus. The principle of NMR is understood by looking at a subatomic level where the particle's behavior follows quantum mechanics. Fortunately, MRI looks at the collective behavior of an ensemble containing many nuclei of the same type that possess a net magnetic moment. Hence, the macroscopic effect of the NMR principle is well described by classical physics. Still, it is beneficial to understand the NMR phenomenon on a quantum level.

Spin is an intrinsic property of a nucleus and is a type of angular momentum. Protons and neutrons are subatomic particles that constitute the nuclei of atoms and have spin = 1/2 property. If the total number of subatomic particles in the nucleus is odd, the nucleus will obtain a nonzero spin. A nucleus, such as ^1H, with an electrical charge and a nonzero spin angular momentum, will generate a nuclear magnetic dipole moment ($\vec{\mu}$) as the spin angular momentum will cause the charged particle to spin around its axis. Like any spinning charged object, the spinning charged particle will induce a magnetic dipole field around the nucleus due to the laws of electromagnetism. The net bulk magnetization for the ensemble of spinning nuclei will be the sum of their individual magnetic moments, and it will be zero when no external magnetic field (B_0) is applied due to random thermal motion giving random orientations of the individual magnetic moments. However, when a magnetic field is applied to the system, the magnetic moments will interact with the field and try to align with the direction of the field. The interaction between the magnetic moment of the spinning nucleus and the applied field causes a precessional motion of $\vec{\mu}$ about B_0, which is illustrated in Fig. 2.1. The precessional motion of the nucleus is described by Larmor's equation, and is given as

$$\omega_0 = \gamma B_0, \tag{2.1}$$

where ω_0 is the induced angular frequency of the nucleus, and is commonly referred to as the Larmor frequency. γ is a physical constant known as the gyromagnetic ratio and is nucleus-dependent. The magnetic properties of a hydrogen nucleus are most commonly exploited to generate an image in MRI. It is largely found in the human body as a compound in water molecules, but also in fat and other organic molecules. The gyromagnetic ratio for a hydrogen nucleus in water is $\gamma =$

2.675×10^8 rad/s/Tesla ($\gamma/2\pi = 42.58 \times 10^6$ Hz/Tesla) (Liang and Lauterbur 2000).

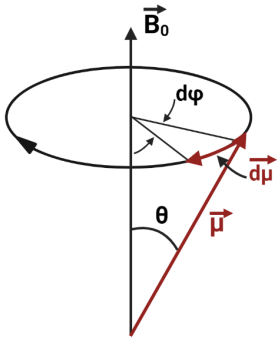

Figure 2.1: The interaction between a nuclear spin and the applied magnetic field B_0 causes a precessional motion of the nuclear magnetic moment ($\vec{\mu}$) about the direction of $\vec{B_0}$. ϕ describes the phase of the rotating magnetic moment vector.

The spinning ^1H-nucleus can either be in a spin-up ($+1/2$) or spin-down ($-1/2$) state, giving the proton only two possible energy states when placed under a magnetic field: either aligned with the $\vec{B_0}$ (in a lower energy state) or anti-parallel (in a higher energy state). The spins will naturally try to reside in the preferred lower energy state as it is more stable. However, thermal energy will prevent the magnetic moments from being fully aligned with $\vec{B_0}$. The distribution of spins in each energy level at thermal equilibrium is given by the Boltzmann distribution:

$$\frac{N^+}{N^-} = exp\left(\hbar\omega_0/k_BT\right),$$

where N^+ is the number of spins in the spin-up state, N^- is the number of spins in the spin-down state, $\hbar$ is Planck's constant, k_B the Boltzmann constant, and T the absolute temperature. There will be a slightly higher probability for the proton's magnetic moment to be aligned with the applied field. The net magnetization vector for an ensemble of proton spins will therefore be aligned with the direction of the applied field when in an equilibrium state. In addition, the net magnetization vector in equilibrium will not have a transverse component due to random initial phases for each $\vec{\mu}$ causing the transverse components of $\vec{M}$ to average out.

2.1.1 Excitation

The net longitudinal macroscopic magnetization vector ($\vec{M_z}$) is not detectable at equilibrium. Therefore, $\vec{M_z}$ must be pushed out of its equilibrium orientation. The system is excited out of equilibrium by applying a second magnetic field (B_1) which oscillates at the Larmor frequency, resulting in optimal energy transfer, and the system will be derived into a state of resonance. For clinical MR systems, the Larmor frequency will lie in the radio-frequency range. Therefore, the transmitted magnetic field applied for excitation of the precessing spins is commonly referred to as an RF pulse. The energy exchange between the spinning nucleus and the oscillating magnetic field causes the bulk magnetization vector to lose alignment with the B_0 and to get tipped into the transfer plane, giving the system a transverse magnetization component ($\vec{M_{xy}}$). The angle at which the magnetization vector is being tipped away from the z-axis (the axis of B_0) is determined by the magnitude of the applied B_1 field and the time interval for which it is applied (t_{RF}). The angle is known as the flip angle and is given by

$$\alpha = \gamma \cdot B_1 \cdot t_{RF}. \tag{2.2}$$

After applying the excitation pulse, the generated $\vec{M_{xy}}$-component oscillates around the z-axis. The oscillating nature of the transverse magnetization component makes the magnetization vector possible to measure as it will induce a current in a nearby receiver coil that is placed within the

generated oscillating field. The observed signal is known as the MR signal or the free induction decay (FID) signal and is the transient response of the spin system after the excitation pulse.

2.1.2 Relaxation Mechanisms

The generated signal will decay rapidly to zero due to spin relaxation mechanisms where the excited spins seek to fall back to the equilibrium state. The $\vec{M}_{xy}$ component will consequently disappear while $\vec{M}_z$ will gradually be restored after an excitation pulse. The energy loss due to proton interactions occurring when relaxing back to equilibrium is described by two main relaxation processes: T_1 relaxation (longitudinal relaxation time) and T_2 relaxation (transverse relaxation time).

T_1 relaxation time describes the restoration of the longitudinal magnetization vector,$\vec{M}_z$, as a result of energy exchange between the excited spins and the surrounding medium. After the excitation pulse, the excited spins seek to fall back to their preferred lower energy state orientation (equilibrium). The excess energy will be transferred to the surrounding environment through stimulated emission. The energy emission is stimulated by the fluctuating magnetic fields generated by the surrounding protons in the molecular environment. Optimal energy transfer will occur if the surrounding spins generate a magnetic field that fluctuates at the same frequency as the relaxing spins (the Larmor frequency). The fluctuating magnetic fields in tissues are caused by many processes, including dipole-dipole interactions and molecular motions of a neighboring spin. The T_1 relaxation times are generally relatively long as the fluctuating magnetic fields are usually local and random in magnitude. The longitudinal relaxation time (the T_1 value) will be tissue-specific and is defined as the time where approximately 63% of its initial $\vec{M}_z$-value (M_0) is restored. The difference in T_1 value between tissues can be utilized as image contrast when applying pulse sequences sensitive to variations in T_1 relaxation times. The obtained images are commonly referred to as T_1-weighted images.

T_2 relaxation time describes the rate at which the net $\vec{M}_{xy}$ component decays following the excitation pulse. The transverse relaxation results from the loss of phase coherence among the spins within a voxel due to the spin interaction with the ever-changing environments of molecules. Any process causing T_1 relaxation will also induce T_2 relaxation due to the stimulated energy transmission to the tissue, yielding a locally increased thermal energy. The released energy may affect the angular momentum components of a nearby spin that contributes to the net $\vec{M}_{xy}$, causing the affected spin to lose phase coherence with the other nearby spins and therefore dephase. However, T_2 relaxation may also occur without T_1 relaxation due to interactions between magnetic fields of the spins creating small field inhomogeneities in the field that the spins experiences. The spins can observe a local time-varying magnetic field either by diffusion along a spatially varying magnetic field or due to interaction with nearby moving spins associated with a small additional magnetic field. The spin interactions with the changing magnetic field will alter the affected spins' precession rate, causing a dynamic dephasing. The dephasing and, hence, the cumulative loss of phase coherence between the spins causes parts of the individual magnetization vectors to cancel out, and the net transverse magnetization vector will start to decay. The evolution of the signal loss due to the decay of the transverse magnetization vector is characterized by an exponential decay described on a timescale T_2. The tissue-specific time constant T_2 is defined as the time for which the transverse magnetization vector has decayed to approximately 37% of its initial value.

Time-independent field inhomogeneities of the external magnetic field introduce an additional dephasing of the spins, resulting in an overall signal decay that is faster than what is described by T_2. These stationary field inhomogeneities may result from defects in the magnet itself or susceptibility differences between tissues. The local field variations induce a static dephasing where the affected spins precess differently depending on their spatial location. Taking into account the additional spin dephasing due to local magnetic field inhomogeneities gives the total relaxation time, denoted T_2^*, to be given as

$$\frac{1}{T_2^*} = \frac{1}{T_2} + \frac{1}{T_2'},$$

where the value of T_2' accounts for the presence of field inhomogeneities. In vivo values for the

transverse relaxation times vary significantly depending on the tissue composition. As for T_1-weighted images, MRI sequences sensitive to differences in transverse relaxation time can be applied to highlight tissues with different T_2 or T_2^* values in the obtained image. Such images are commonly referred to as T_2- or T_2^*-weighted image, depending on if the measured signal follow the T_2 or the T_2^* decay.

All biological tissues are heterogeneous, containing various components with their particular relaxation time. However, the complex composition is simplified in MRI by looking at the mean relaxation time of the components within a voxel (Chang et al. 2015). The evolution of the recovery of the longitudinal magnetization component (T_1 relaxation) and the diminishing of the transverse component (T_2 and T_2^* relaxation) after an excitation pulse is illustrated in Fig. 2.2. Both relaxation mechanisms are independent processes, but occur simultaneously after the excitation of the spins.

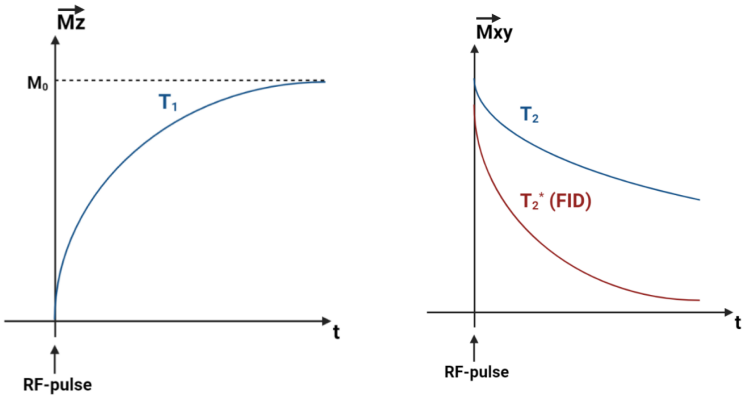

(a) (b)

Figure 2.2: (a) The exponential regrowth of the initial longitudinal magnetization vector, described by the T_1 relaxation time. (b) The exponential decay of the transverse magnetization vector, described by the T_2 relaxation time (blue graph), and the T_2^* relaxation time (red graph) which includes the effect of field inhomogeneities.

2.1.3 Spatial Encoding

Based on the information in Section 2.1.1 we know how to generate a detectable signal from a biological sample. The receiver coil will measure the sum of the induced MR signals from all parts of the object with excited spins. However, for an anatomical image to be generated, a differentiation of the spatial origins of the individual local signals constituting the total measured MR signal must be achieved. To do so, two spatial localization methods, slice excitation, and spatial encoding, are employed. The spatial localization mechanisms utilize independent linearly varying magnetic fields (a magnetic field gradient) that are defined in each orthogonal direction of the MR scanner (x-, y-, and z-direction). For a standard MR scanner, the static magnetic field is applied along the machine's bore's direction, which is conventionally defined as the z-direction. When a patient is placed in the MR scanner with the head first, the z-direction will correspond to the inferior-superior direction. The horizontal axis of the MR system is typically referred to as the x-direction and corresponds to the direction from right to left, and the vertical axis will accordingly be the y-axis which is set to increase along the anterior-posterior direction of the patient.

Selective Excitation

The MR signal measured by a receiver coil contains information about the total measured magnetization vector's phase, frequency, and amplitude. However, generating an image of a human is a four-dimensional problem where information about the location of the spins generating a signal

along the x-,y-, and z-direction is needed in addition to the signal's amplitude. Therefore, slice excitation is performed to reduce the problem by one dimension before spatially localizing the generated signals. Applying slice excitation will selectively excite only spins within a 2D-image plane at a defined position within the patient, restricting the registered MR signal to originate only from the excited slice.

Slice selection is achieved by applying a gradient field during the transmission of the excitation pulse. A linear magnetic field is applied along the slice-select direction (a slice-select gradient) in addition to the background field to make the Larmor frequency dependent on the position along the applied gradient. Thus, the Larmor frequencies will now be given as

$$\omega(z) = \omega_0 + \gamma \cdot G_S \cdot z,$$

where G_S is the strength of the slice-selective gradient and z a spatial localization along the direction of the gradient. As the transmitted RF pulse is frequency-selective, applying a slice-select gradient during the excitation period causes only the spins within a narrow frequency range, centered at the frequency at which the RF pulse oscillates, to be excited. Thus, the excitation pulse will now be spatially selective. The width of the excited slice (Δz) is given by

$$\Delta z = \frac{\Delta f}{G_S \cdot \frac{\gamma}{2\pi}},$$

where Δf is the frequency bandwidth of the excitation pulse.

The slice excitation assumes that the magnetization vector is flipped at the center of the applied RF pulse/slice-select gradient. Consequently, the second half of the slice-select gradient will induce a through-slice phase dispersion of the spins due to slight deviations in the resonant frequencies for the spins located along the gradient. The induced phase dispersion occurring in the second half of the slice-select gradient is corrected by applying a rephasing lobe after the primary slice-select gradient lobe. Hence, undesired signal loss due to spin dephasing induced by the slice-select gradient is avoided.

In-plane Localization and k-space

The signal from excited spins within a slice can be manipulated to make a full clinical MR image. Spatial localization of the MR signal can be obtained by encoding spatial information into the signal during the free precession period of the transverse magnetization component. As the generated MR signal is in the form of a complex exponential, spatial information can be encoded into the signal by altering its phase and frequency information. Hence, frequency-encoding and phase-encoding are performed for the in-plane localization of the MR signal.

Frequency encoding of the activated MR signal is achieved by applying a linear magnetic field, commonly referred to as the frequency-encoding gradient (G_{FE}), while the MR signal is sampled at different time points. Predictably altering the main magnetic field by applying the frequency-encoding gradient causes the oscillation frequency of the activated MR signal to be dependent on their spatial origin along the direction of the gradient. When the object experience the homogeneous B_0 field in addition to the linearly varying field strength,G_{FE}, the Larmor frequency along the frequency-encoding direction will be given by

$$\omega(\vec{r}) = \omega_0 + \gamma G_{FE} \cdot \vec{r}.$$

Thus, the received signal sampled at time t after excitation will be the sum of all local frequency-encoded signals originating from the excited spins and is given by

$$S(t) = \int_{object} \rho(\vec{r}) e^{-i\gamma G_{FE} \cdot \vec{r} t} d\vec{r} \tag{2.3}$$

when the carrier signal, $e^{-i\omega_0 t}$, is removed (demodulated). $\rho(\vec{r})$ is the spin-density at a position $\vec{r}$ in the imaging volume. Sampling the evolving MR signal in real-time will cause each measured

point to be affected by the gradient moment to a different amount and, hence, correspond to a different resonance frequency. The individual frequencies constituting the total MR signal originating from the whole body can be uniquely sorted out by using the Fourier transformation. Following the Fourier transform relation, the signal at each spatial frequency along the frequency-encoding direction ($\vec{k}_{FE}$) is given by

$$S(\vec{k}) = \int_{object} \rho(\vec{r}) e^{-i2\pi\vec{k}\cdot\vec{r}} d\vec{r}, \tag{2.4}$$

and the mapping relationship between the spatial frequency and the time at which the signal is sampled after RF excitation (t) is

$$\vec{k}_{FE}(t) = \frac{\gamma}{2\pi} \int_0^t G_{FE}(\tau) d\tau. \tag{2.5}$$

Thus, the information about the signal intensity for the spatial frequencies is derived directly from the measured MR signal by utilizing the Fourier transform relation, and the measured raw data is stored in a matrix known as k-space.

Phase-encoding is also applied to the MR signal to attain spatial information in both in-plane directions. The phase-encoding is applied in a preparatory period before the sampling of the MR signal, and it is performed by applying a gradient along the phase-encoding direction (G_{PE}) for a short time interval (T_{PE}), causing slight variations in the Larmor frequency of the spins along the gradient direction. Thus, the spins will accumulate a different amount of phase, depending on their spatial location, and the signal is phase-encoded. The initial phase term attained in the measured signals is given as

$$\phi(\vec{r}) = -\gamma G_{PE} \cdot \vec{r} T_{PE},$$

where $\vec{r}$ the position along the gradient. Similarly to the frequency-encoding, the effect of the phase encoding can be described by the Fourier transform, where the phase-encoded signal is described similarly as in Eq. 2.4, but with the relation between the spatial frequency along the phase-encoding direction and time t is given as

$$\vec{k}_{PE} = \frac{\gamma}{2\pi} \int_0^{T_{PE}} G_{PE}(\tau) d\tau.$$

Thus, information about the phase accumulation over the time interval T_{PE} will be stored in k-space, and both axes of k-space will represent spatial frequencies as frequency is defined as phase change over time.

Overall, k-space stores the digitized MR signals in the Fourier space during data acquisition and contains information about the frequency spectrum of the image-space for the two in-plane directions. The value of $\mathbf{k}_{PE}$ will be fixed for each sampling period, while the value of $\mathbf{k}$ along the frequency-encoding direction is a function of time as its value evolves during the sampling period. Thus, each sampling period will fill a line in k-space along the frequency-encoding direction, and the applied gradient, G_{FE}, determines the speed of the movement in k-space. A new preparatory period with a changed phase-encoding gradient strength or T_{PE} is needed to adjust the induced initial phase angle and, hence, to move along the phase-encoding direction in k-space. In summary, the in-plane spatial encoding gradients determine the value of $\mathbf{k}$, thus, the movement in k-space, and ensure that the signals stored in k-space at given frequencies are related to spatial positions in the image domain. Hence, the spatial encoding mechanism of the sampled MR signals relies on a homogeneous background field and stable linear gradients to correctly store the raw data in k-space. When a k-space is fully sampled, the acquired data can be used to reconstruct an image through the Fourier relationship.

When sampling echoed MR signal, the k-space will be symmetrical with the edges containing high spatial frequency information, determining the details in the image, and the center of k-space will include the low-frequency information and determine the contrast in the reconstructed image.

2.2 MR Acquisition Sequences

The appearance and the information gained from an acquired MR image are largely determined by the sequence parameters of the applied pulse sequence. This Section will introduce the MRI sequences employed in this thesis.

2.2.1 Basic Spin Echo and Gradient Echo Sequence

Spin-echo and gradient-recalled echo are the two major pulse sequence families in MRI. The diagrams of a basic SE and GRE sequence illustrated in the following paragraphs show the sampling of the MR signal using a line-by-line k-space trajectory, where the data is sampled along one line of k-space for each repetition time (TR). The diagrams indicate the generation of an echo signal together with the applied spatial encoding mechanisms. The time between the center of the excitation RF pulse and the echoed signal is defined as the echo time (TE). The phase-encoding gradient will be changed for each TR, indicated as the striped lines in the diagrams, to sample the whole k-space. Each echo signal is sampled at the same moment of time (at TE) such that the spins are in the same relaxation process state during each signal read-out.

The Spin Echo sequence

The conventional SE sequences generate an echoed signal at TE by utilizing a two-pulse excitation scheme consisting of a 90° excitation pulse followed by a time delay (TE/2) before the 180° refocusing pulse is applied. Both RF pulses are applied with slice selection gradients. It is assumed that the refocusing pulse is time symmetrical and that it inverts the magnetization vectors instantaneously at the center of the gradient. Hence, no refocusing lobe is required for the 180° RF pulse as the dephasing occurring in the first half of the applied gradient will be inverted and corrected for in the second half of the gradient.

The diagram of a basic spin-echo sequence is illustrated in Fig. 2.3a and the evolution of the magnetization vector in Fig. 2.3b. Before an excitation pulse is applied, the spins contributing to the net magnetization vector will be in equilibrium and generate a net longitudinal magnetization vector aligned with the applied field (step 1). Typically, spin-echo sequences use a slice-selective 90° RF excitation pulse to excite the spins into the transverse plane (step 2). The spins will begin to dephase relative to each other due to local field variations, causing some spins to precess faster than others (step 3). The rate of dephasing is described by the transverse relaxation time, T_2^*, and the FID signal will become exponentially dampened by the T_2^* relaxation mechanism. The dephasing caused by the static magnetic field variations will be a reversible process, assuming that the affected spins are stationary, and the accumulated phase shifts can be corrected. The static dephasing is reversed by applying a 180° RF pulse after half the echo time (step 4). The 180° refocusing pulse inverts the phase shifts that the spins have accumulated in the time interval between the excitation and the refocusing pulse. Thus, the spins that were ahead of the net magnetization vector due to the faster precession rate (the red arrows in Fig. 2.3b) will be flipped to be behind and vice versa. The precession rate of the affected spins will be unchanged, as their physical location and molecular environment are the same before and after the refocusing pulse. Thus, the spins that got flipped to be behind will still precess faster and catch up with the slower precessing spins that got flipped to be ahead. The accumulated phase shifts will gradually be reduced and fully refocus as an echoed signal at TE (step 5) if equal time is given to the system after the refocusing pulse, as it was given before its application. However, the 180° refocusing pulse will not eliminate the dynamic dephasing process induced by variable field inhomogeneities generated by spin-spin interactions (T_2). The amplitude of the refocused signal at TE will therefore be brought up to follow the signal decay function described by the T_2 curve (Fig. 2.4).

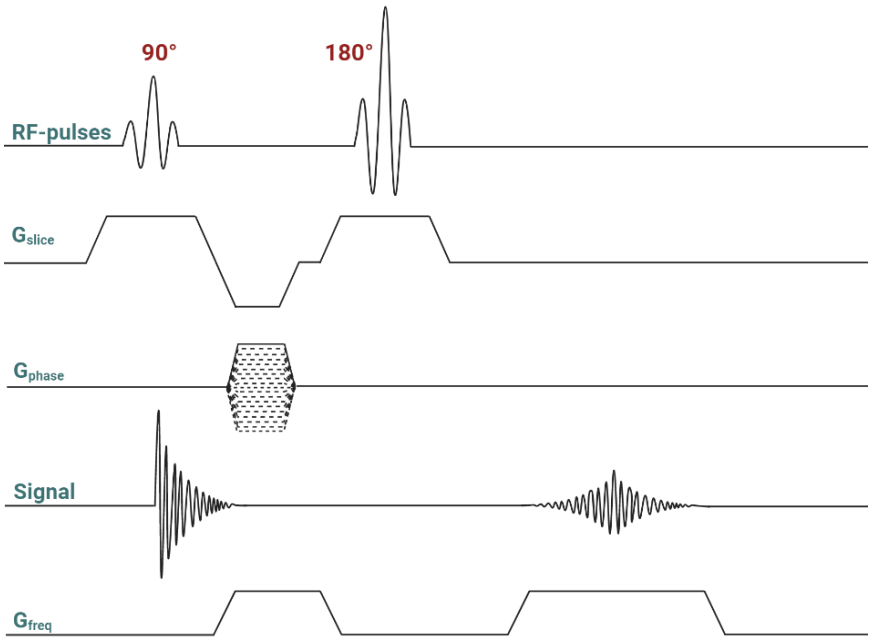

(a)

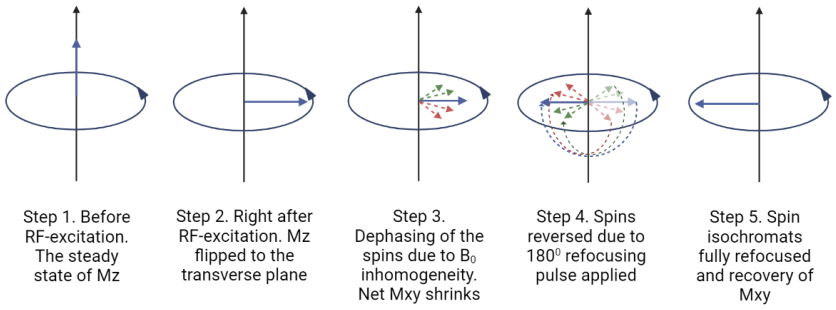

(b)

Figure 2.3: (a) Schematic illustration of a conventional SE sequence, showing timeline for the RF pulses, the slice-selective and the in-plane localization gradients in addition to the generated signal. (b) Step-wise illustration of how the spins that have dephased due to B_0 inhomogeneities get refocused into a spin-echo by applying a 180° RF pulse.

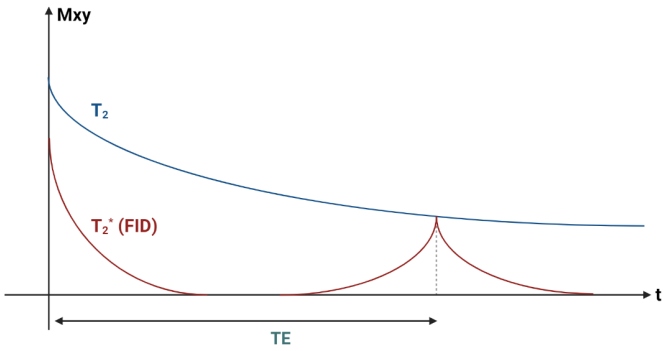

Figure 2.4: The spin-echo sequence generates an echoed signal at TE modulated by T_2 relaxation. The blue graph indicates the exponential function that damps the signal due to T_2 relaxation. The red graph shows the apparent signal, which before applying a 180° refocusing pulse, is an FID signal that is damped by the process described by the T_2^* relaxation time.

Basic Gradient Echo Sequences

Another form of echoed signal frequently applied in MRI is induced by employing gradient coils that generate time-varying gradient magnetic fields and are known as gradient-recalled echo. A general scheme of a conventional GRE sequence is indicated in Fig. 2.5a, and the step-wise evolution of the magnetization vector in Fig. 2.5b. The slice-excitation step in GRE sequences (step 2 in Fig. 2.5a) typically utilizes smaller flip angles than 90°, and the flip angle is indicated as α in Fig. 2.5a.

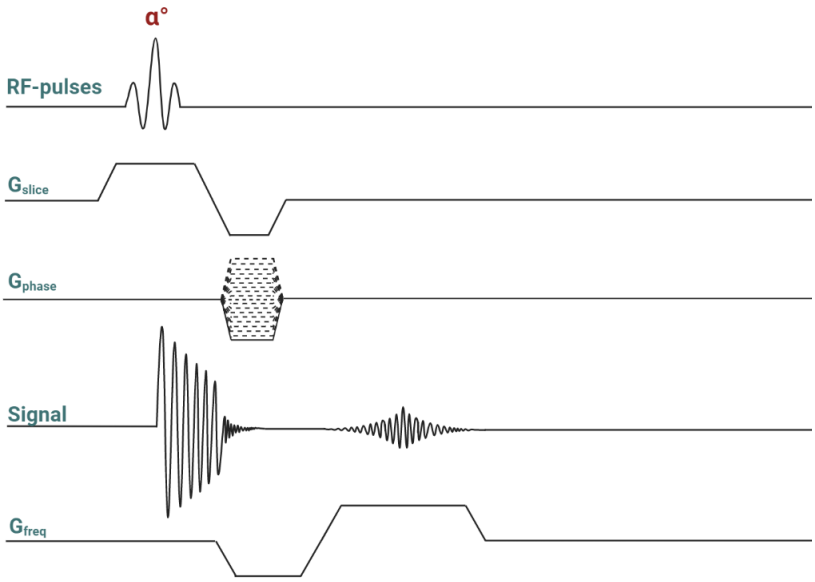

(a)

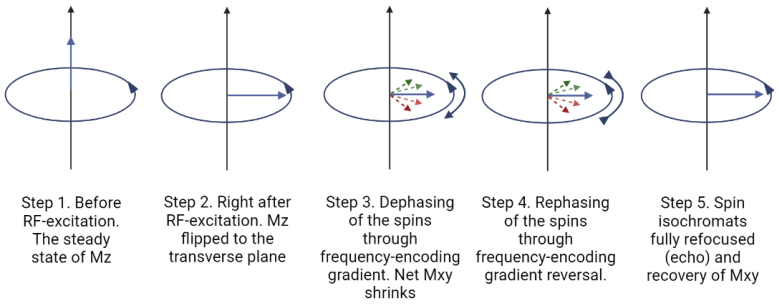

(b)

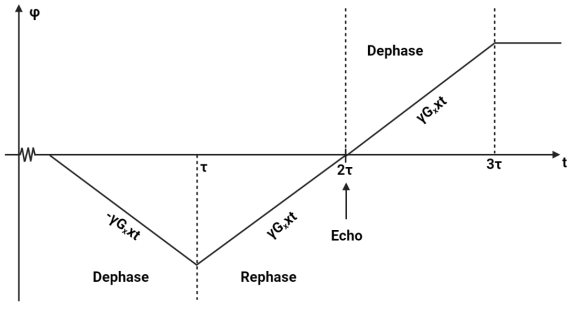

(c)

Figure 2.5: (a) A schematic illustration of a conventional GRE sequence. (b) Step-wise illustration of the excited spins evolution during a GRE sequence. (c) A illustration of the phase evolution for the spins, caused by a magnetic field gradient applied along the frequency-encoding direction (defined along the x-direction in the figure).

GRE sequences are based on the dephasing and rephasing of spins through the application of magnetic field gradients, such that a symmetrical k-space can be filled and used to reconstruct an image. A symmetrical sampling of k-space is achieved by applying an initial prephase gradient before the read-out gradient. The purpose of the prephase gradient is to move the initial k-space location to one of the ends in the k-space by inducing an initial dephasing of the spins, before acquisition of the MR signal during the read-out gradient. The movement in k-space is determined by the properties of the applied gradient, as previously mentioned in Section 2.1.3 under In-plane Localization and k-space. By applying a prephase gradient of half the gradient moment to the read-out gradient, the initial location in k-space is moved to one of its edges. Following the integral describing the spatial location in k-space, a negative prephase gradient will move to -k_{max}, and a positive gradient will move to +k_{max}. Thus, the prephase gradient influences the starting point prior to the sampling of the MR signal. Subsequently, applying the read-out gradient, of opposite polarity to the prephase gradient, while the MR signal is simultaneously sampled will map the k-space following the relationship given in Eq. 2.5, where it traverses the k-space in the opposite direction to the initial movement of the prephase gradient. The initial dephasing of the spins induced by the prephase gradient will be fully refocused at the center of k-space ($k_{FE} = 0$), and an echoed signal is generated at TE. The generation of a gradient-recalled echoed signal is principally also being done for the SE sequence. However, the initial lobe is of equal polarity to the read-out gradient due to the presence of the 180° refocusing pulse.

Multi-echo GRE Sequence

The same read-out gradient used to create a single gradient echo signal can be repeated to form several echoed signals after a single RF excitation. By applying read-out gradients of alternating polarity, the second gradient lobe of the prior read-out gradient will act as a prephase gradient for the subsequent read-out gradient. Consequently, multiple GRE echoes can be induced after a single excitation pulse by applying a train of read-out gradient lobes of alternating polarity, as long as the transverse magnetization vector hasn't completely diminished due to T_2^* relaxation (Fig. 2.6). By sampling multiple echoed signals at different times after the excitation pulse, without changing the phase-encoding for each TR, the same line of k-space will be filled for each TR. Thus, multiple images of the same slice taken at different echo times are obtained.

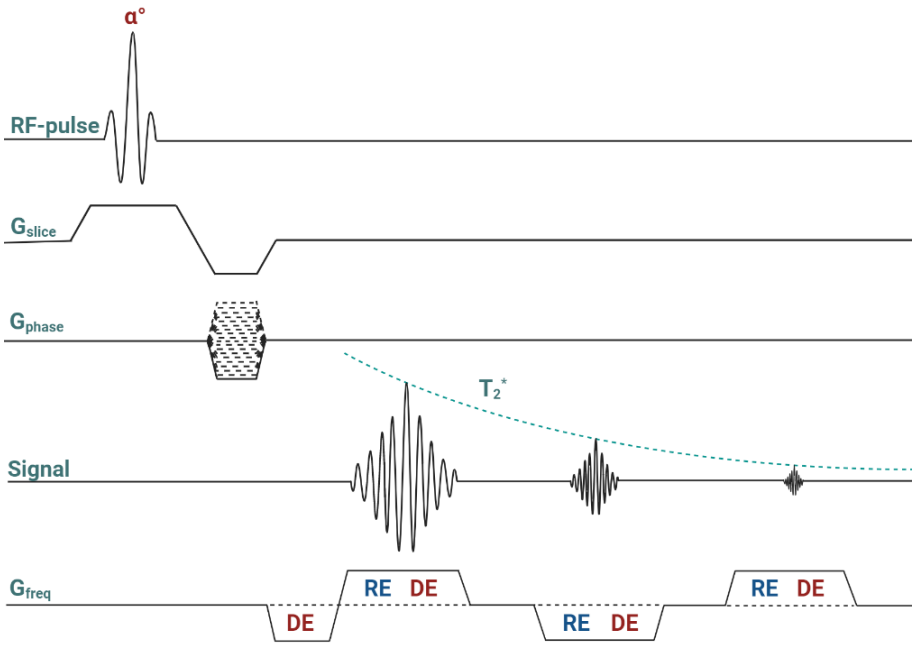

Figure 2.6: A multi-echo gradient echo sequence where the first half of the read-out gradient lobes rephase (RE) the spins, giving an echo signal, and the last half dephases (DE) them.

The information obtained from a ME-GRE scheme can be utilized to quantify the value of T_2^* for different tissue compartments. The relaxation of the transverse magnetization vector, and therefore the height of each gradient echo signal sampled at different echo times, follow an evolution described by the T_2^* relaxation time. T_2^* maps can be derived by simply fitting the ME-GRE signal to a mono-exponential decay curve:

$$S(TE) = S_0 \cdot exp\left(-\frac{TE}{T_2^*}\right), \tag{2.6}$$

where S_0 is the signal strength at TE = 0 (Hagberg et al. 2002). Quantifying T_2^* maps can give valuable information about the surrounding environment and the local field inhomogeneities present which the spins observe.

Field mapping

Information about the field inhomogeneity present within the imaging volume can be achieved by applying a field mapping imaging sequence. B_0 inhomogeneity will induce an additional phase accumulation term in the signal that accumulates with time after the RF-excitation. The field mapping sequence acquires two images taken at different echo times. By keeping the image information in their complex form, the information about the additional phase accumulation that occurs between the two echo times can be achieved. The phase difference in the signal between the two echo times can be calculated from

$$\Delta\phi = \angle[S_1 \cdot S_2^*]$$

where S_1 and S_2 are the images obtained at TE_1 and TE_2, respectively. The subscript * denotes the complex conjugate of the signal, and $\angle$ indicates computing the angle of the complex data. The calculated phase difference will be between $\pm\pi$. As the accumulated phase of the signal between the two echo times can exceed the interval between $[-\pi, \pi]$ if the susceptibility-induced field gradient (SFG) is strong enough, the time difference between the two echo times (ΔTE) should be kept short to minimize phase wrapping. The local frequency shift due to B_0 inhomogeneity is proportional to the phase accumulation occurring in the time interval between the two echo times, ΔTE, as follows:

$$\Delta\omega = \frac{\Delta\phi}{\Delta TE}, \tag{2.7}$$

where $\Delta\omega$ is the difference in frequency from the nominal Larmor frequency. The calculated $\Delta\omega$ from the above expression is given in radians per second (rad/s).

Inversion Recovery

Inversion recovery (IR) pulse sequences include a 180° magnetization preparation pulse before applying a conventional SE or GRE sequence. The time between the application of the 180° pre-pulse and the RF-excitation pulse is known as the inversion time (TI). Applying a 180° RF-preparation pulse inverts the net longitudinal magnetization vector for the different tissues. The tissues will still only possess a net longitudinal magnetization vector, but now pointing in the opposite direction from its direction in equilibrium. The different tissues will regrow their initial longitudinal magnetization vector differently due to their tissue-specific T_1 value (Fig. 2.7). The tissues with short T_1 values (yellow graph) will relax back to their equilibrium state faster than tissues with longer T_1 values (blue graph). Depending on when the excitation pulse is applied, the tissues with shorter T_1 values will generally generate a stronger signal in the obtained image as a larger part of their initial magnetization vector has been restored before the excitation pulse is applied. Hence, the tissues with shorter T_1 values will have a greater transverse magnetization component than tissues with longer T_1 values for the following read-out of the MR signal. Inversion recovery can be applied to influence the degree of signal coming from the different tissues. It can be applied to null out a signal from a certain tissue selectively or to retain T_1 contrast in the image. The suppression of different tissues is achieved by choosing TI when their M_z-component is at zero.

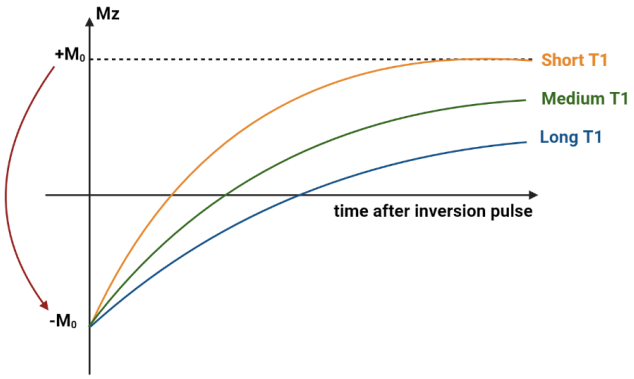

Figure 2.7: The regrowth of the initial magnetization vector for tissues with different T_1 values after applying a 180° inversion pulse.

2.2.2 MP-RAGE and MP-2RAGE

MP-RAGE (Magnetization Prepared - RApid Gradient Echo) is a fast pulse sequence that has become the dominant sequence for obtaining $3D$ T_1-weighted images. The sequence produces high-resolution images with very good anatomical detail, especially in the brain. MP-RAGE consists of a magnetization preparation (usually a non-selective 180° inversion pulse for T_1-weighting), followed by rapid spoiled gradient-echo sequences. The magnetization preparation period follows the same mechanisms as described in Section 2.2.1 under Inversion Recovery. In addition, low flip angles and short TE are used in MP-RAGE imaging sequences to have rapid read-outs of the signal. The MP-RAGE sequence consists of a train of excitation pulses with low flip-angles, and short TEs applied after TI to fill the lines of k-space, and a relatively long repetition time is typical for MP-RAGE sequences. To ensure that each in-plane line of k-space for an image slice has the same degree of relaxation, the $3D$ MP-RAGE acquire all slice encoding 'lines' of k-space from each preparation pulse, followed by a time delay between the acquisitions before moving onto the next in-plane line of k-space. Hence, it is the phase-encoding gradient that is being changed for each TR.

The MP-2RAGE sequence is based on the same principles as in MP-RAGE, but in contrast, it applies two bulks of a spoiled-gradient echo sequence read-outs for each inversion pulse, effectively giving two images with different inversion recovery times. The different inversion recovery times used for the two acquired images in the MP-2RAGE sequence are optimized such that the combined image will have a superior grey to white matter contrast.

2.2.3 Ultrashort Echo Time Sequences

For many conventional clinical MR pulse sequences, tissues with short T_2 relaxation time will have minor to no detectable signal (Robson et al. 2004). Bone can, in principle, be a source of MR signal as its composition includes protons. However, bone contains a high fraction of components with a very short T_2 relaxation time, causing its mean transverse magnetization vector to vanish before the read-out gradient is applied. Hence, conventional MR sequences will not be able to detect the decaying signal of bone (Chang et al. 2015). The lack of signal from bone cause problems in the visualization and differentiation between bone and air as both tissue types are seen as dark areas in the obtained image. A differentiation between bone and air can be achieved if sequences with short enough echo times for the signal from bone to be measured can be applied.

Ultrashort Echo Time (UTE) sequence was first introduced by Pauly et al. 1989 and is the general term for sequences that are able to have ultrashort echo times (TE less than 1 ms). Having such small echo times makes it possible to detect signals from tissues with short (less than $1 - 10$ms) and ultrashort (less than $0.1 - 1$ms) transverse relaxation times (Chang et al. 2015). The UTE

sequence is a gradient-echo-based radial imaging technique. The ultrashort TEs are accomplished by using a short RF-excitation pulse followed by the acquisition of the data right after the excitation pulse step. Due to physical limitations of the gradients and using ultrashort echo times, the data acquisition will occur while the gradient is ramping up, giving a ramped sampling of the data. In addition, the k-space trajectory for sampling the information of the detected signal in the k-space is radial from the center out. Hence, no phase-encoding gradient step is used, having the benefit of making the TE even shorter. The application of very short TE together with relatively small flip angles causes the UTE sequences to produce heavily proton-density-weighted images.

The tissues with long transverse relaxation time will still be illustrated as bright structures in the obtained UTE image. It is common to acquire a second image at a later echo time (in the order of ms) and subtract the acquired image information from the UTE image, such that the tissues with short T_2 values are featured in the obtained image. The tissues with long transverse relaxation times, and therefore high signal intensity, will in the subtracted image be suppressed as darker structures while the signal from the tissues with short T_2 values will be highlighted. Doing so can give a better visualization of tissues with short T_2 values and, hence, give better air-bone contrast in the obtained image (Chang et al. 2015).

2.3 Magnetic Susceptibility

The volume magnetic susceptibility is a property inherent in all materials that describes the materials tendency to become magnetized when placed under a magnetic field. χ is an dimensionless quantity in the SI unit system and is given by the equation:

$$\vec{\chi} = \frac{\vec{M}}{\vec{H}} \,, \tag{2.8}$$

where $\vec{M}$ is the degree of the materials macroscopic magnetization and $\vec{H}$ is the applied magnetic field intensity (Duyn and J. Schenck 2016). Therefore, when taking the contribution made by the magnetization of the tissue into account, the total local magnetic field ($\vec{B}$) that the spins within a bulk of tissue observe is given as

$$\vec{B} = \mu_0(\vec{H} + \vec{M}) = \mu_0(1 + \chi)\vec{H} \,. \tag{2.9}$$

The material's molecular composition determines both the sign and the value of χ. χ can be negative or positive, reflecting if the material's magnetization opposes (diamagnetism) or aligns (paramagnetism) the applied field, respectively. The diamagnetic effect is a property excising in all substances. For simplicity, the electrons surrounding a nucleus can be seen to move in a circular orbital motion. The circular orbital motion of an electron surrounding a nucleus generates a magnetic moment in the opposing direction to the angular moment (the spin direction) of the electron (Mulay 1963). When an external magnetic field is applied to the system, the circular motion of the electrons will be alternated according to Farraday and Lenz's law, where an electromagnetic force that tries to oppose the change applied to the system will be induced. The field-induced alteration of electron orbits causing a net magnetic moment oriented in an opposing direction to the external field is known as the diamagnetic effect (Duyn and J. Schenck 2016). Electrons tend to pair up with opposite spin states at each energy state of the atom/molecule. Generally, diamagnetism is associated with materials that consist of atoms/molecules with paired electrons. When no external field is applied, these materials will have no net magnetic moment as electrons of opposite spin states, but at equal energy levels generate equal magnetic moments in opposite directions that counteract each other. However, when the system is placed under a magnetic field, the diamagnetic effect induces a total magnetic moment in the opposite direction relative to the applied field.

Paramagnetism, on the other hand, is generally associated with materials that have unpaired electrons giving them a net intrinsic magnetic moment. When placed under a magnetic field, the net magnetic moment of the atom/molecules in the material will experience a torque force given by

$$\vec{\tau} = \vec{\mu} \times \vec{B_0}$$

that tries to align the net magnetic moments with the direction of the applied field, where the potential energy is at a minimum (Young and Freedman 2012). However, thermal motion within the material will prevent the magnetic moments from completely aligning with the direction of the field. The diamagnetic effect will also be present in paramagnetic materials, further weakening the extent of the paramagnetic effect.

As a bulk substance, the total induced magnetization of the material will be the sum of all individual magnetic moments, including the field-induced magnetic moments. The bulk magnetization will point in the opposite direction of the applied field for materials with diamagnetic properties and locally reduce the total magnetic field. In contrast, it will align with the direction of the field for materials with paramagnetic properties and, hence, locally strengthen the total magnetic field.

2.3.1 Magnetic Susceptibility in the Human Body

The human body consists of a distribution of magnetic susceptibility due to different properties between the tissues. Most biological molecules have even numbers of electrons, making most human tissues diamagnetic. Typical χ-values for most human tissues are similar to that of water which is approximately equal to $-9 \cdot 10^{-6}$ with slight variations due to different tissue compositions (Marques and Bowtell 2005). However, cortical bone is notably less diamagnetic than, for instance, soft tissue (Czervionke et al. 1988).

In addition to diamagnetic tissues, there also exist substances and structures with paramagnetic properties in the human body. The oxygen atom has an unpaired electron in an anti-bonding orbit, making the molecule O_2 paramagnetic (Boveris 1998). Air has a very low susceptibility value owning to its low density and is equal to $0.36 \cdot 10^{-6}$ under normal temperature and pressure (NTP) conditions. The anatomy of the human head includes air-filled regions, such as the nasal cavities, the auditory cavity (including the middle ear), and the sinuses (frontal, maxillary, sphenoid, and ethmoid). There also exist numerous small air cavities at different locations within the temporal bone of the brain. Another important substance in the human body with paramagnetic properties is the chemical element iron. Iron is found in the human body as a free element with high concentrations in the brain structures red nuclei and substantia nigra, and inside the structure of hemoglobin, where it plays an essential part in binding oxygen atoms. Deoxyhemoglobin molecules will, therefore, also show paramagnetic properties due to their unbound iron content.

2.4 Magnetic Susceptibility Artifacts in MRI

When a subject is placed into the MR scanner, the magnetization of the tissues will induce an additional perturbing field that distorts the B_0 field homogeneity. The susceptibility-induced field distortions will falsify the assumption made by the acquisition mechanism, namely, the homogeneous background field and the linearity of the spatial encoding gradients will be distorted, consequently causing errors in the acquisition of the MR signal. Hence, the susceptibility-induced B_0 inhomogeneity will produce profound artifacts in the MR image. The main artifacts related to magnetic susceptibility are two-fold: they can be seen as local signal-void and/or geometric distortions, depending on the properties of the field inhomogeneity and the sequence parameters used. In addition, the appearance of the susceptibility artifacts largely depends on the direction of the SFGs, which can be present in all three spatial dimensions. The susceptibility artifacts observed in MR images are generally a mix of both effects, and the susceptibility effects will cause more pronounced imaging artifacts at higher field strengths due to the linear dependency between the susceptibility-induced field and field strength.

2.4.1 Signal Loss

Following the Larmor Equation, given in Eq. 2.1, the hydrogen nuclei precess at a frequency depending on the local magnetic field. Thus, local field variations will induce a position-dependent

dispersion of the spins' resonance frequencies, leading to phase shifts. The induced position-dependent phase term for the individual spins gives rise to a phase dispersion across the affected voxel (Fig. 2.8c). The unwanted phase term causes mutual cancellation of the dephased magnetization vectors, leading to a reduced magnitude of the reconstructed signal originating from the affected voxel (Brown et al. 1999). Signal loss is prominent in voxels close to a strong susceptibility interface where an abrupt change in the local magnetic field is present (Fig. 2.8a).In addition, Fig. 2.8a also indicates the field inhomogeneities on a macroscopic level where the perturbing field occurs at a scale that's larger than at least a voxel size. Due to their relatively large extent compared to the voxel dimension, the macroscopic field inhomogeneities can be modeled by linear gradients. Fig. 2.8b indicates the microscopic field variations occurring over a distance much smaller than the voxel size. The microscopic field variations are induced by the molecular environment of the spins and other microscopic sources, but can also be due to highly variable field patterns induced by tissue compartments with complex geometrical shapes (Brown et al. 1999). The intra-voxel dephasing leads to a shortening of the apparent transverse relaxation time.

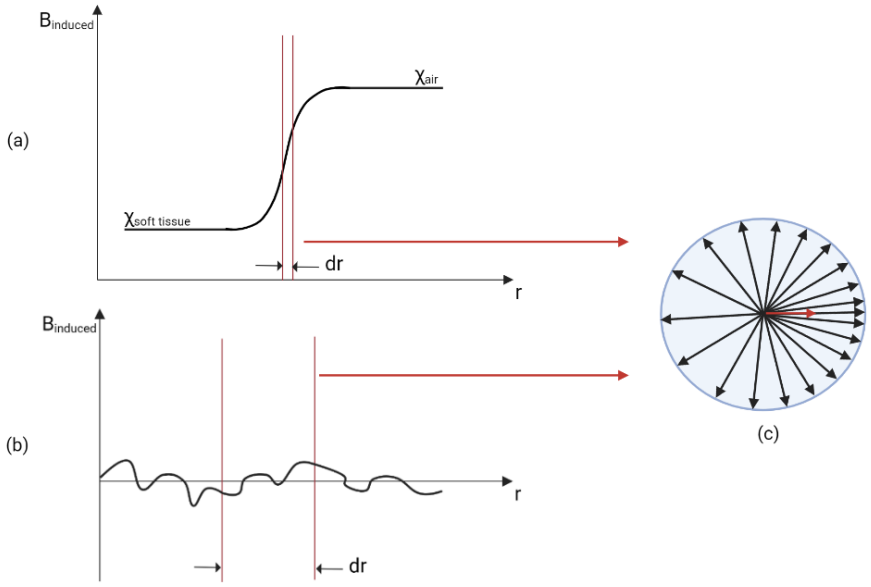

Figure 2.8: (a) Induced local field gradient across a voxel located close to a tissue interface with an abrupt change in magnetic susceptibility value. (b) Highly variable field distortions over small distances relative to the voxel dimension, causing intravoxel dephasing. (c) Intravoxel spin dephasing due to local field variations.

Effect of Local Through-plane Susceptibility Gradients

A phase dispersion across the slice thickness will be induced by the presence of local through-plane susceptibility gradients, $G_{z,s}$, and a signal intensity variation may occur across the slice, giving a local signal reduction in the slice integrated signal (Brown et al. 1999). The voxel dimensions in the slice-select direction are most commonly larger than the in-plane voxel dimensions in MR imaging. A larger voxel dimension will include a larger spatial extent to which the perturbing field variation can occur, effectively increasing its effect on the phase dispersion along the voxel's dimension. Hence, the imaging voxels are typically sensitive to the presence of through-slice field inhomogeneities, and will modulate the signal intensity more significantly than the in-plane SFGs (Deichmann, Josephs et al. 2002). The phase dispersion due to local SFGs across the slice is not taken into account in the theoretical model for the signal decay, which only considers the decay of the magnetization vector due to the relaxation processes. Consequently, the susceptibility-induced signal loss will lead to underestimation of the relaxation time T_2^* at the areas strongly affected by the SFGs. The underestimation of the T_2^* value can give rise to problems when interpreting T_2^* maps. It causes difficulties in knowing if the changes in T_2^* are due to changes in the tissue itself or caused by local magnetic field changes (ΔB_0). Dahnke and Schaeffter 2005 introduced a

corrected expression for the MR signal decay in a gradient echo scheme where the background field inhomogeneity in the slice-selection direction is taken into account. The corrected MR signal in a gradient echo scheme was written as

$$S_{\Delta B_0}(TE) = S_0 \cdot exp\left(-\frac{TE}{T_2^*}\right) \cdot |sinc(\gamma \cdot G_{z,s} \cdot \Delta z \cdot TE/2)|\,, \tag{2.10}$$

where Δz is the slice thickness, and S_0 is the signal strength at TE= 0 (Dahnke and Schaeffter 2005; Peters et al. 2007). The equation assumes that the dominant effect of the field inhomogeneity that causes signal loss is in the slice-select direction, and it makes the first-order approximation where the through-plane susceptibility-induced field gradients are assumed to be linear across the z-direction (Dahnke and Schaeffter 2005). In addition, the expression assumes an ideal slice profile for the slice-excitation, where the frequencies included in the voxel in the z-direction are described by a perfect rectangular function in the frequency domain and a sinc-function of infinite length in the time-domain. Consequently, the exponential signal decay will be modulated by a sinc-function. If the assumptions are fulfilled, Eq. 2.10 will give a better representation of the signal decay in regions strongly affected by field inhomogeneities in the slice-select direction (Dahnke and Schaeffter 2005; Peters et al. 2007).

In-plane susceptibility gradients lead to a different modulation of the signal behavior than the through-slice susceptibility gradients. The effect of in-plane susceptibility gradients is further discussed in Reichenbach et al. 1997.

2.4.2 Geometric Distortions

As mentioned in Section 2.1.3, a correct sampling of the MR signal to k-space relies on the linear relationship between the spin's position and frequency, established by the applied spatially linear encoding gradients during the read-out of the MR signal. However, the presence of macroscopic field variations will distort the linearity and give rise to a local field shift (Fig. 2.9), thus causing the spins to be wrongly spatially encoded during the read-out of the MR signal. The incorrect spatial localization of the spins is referred to as image distortion and will be identical for gradient-echo and spin-echo images. The direction in which the image distortion is dominant in the reconstructed image depends largely on the trajectory used to sample the cartesian k-space (a line-by-line or a zig-zag trajectory).

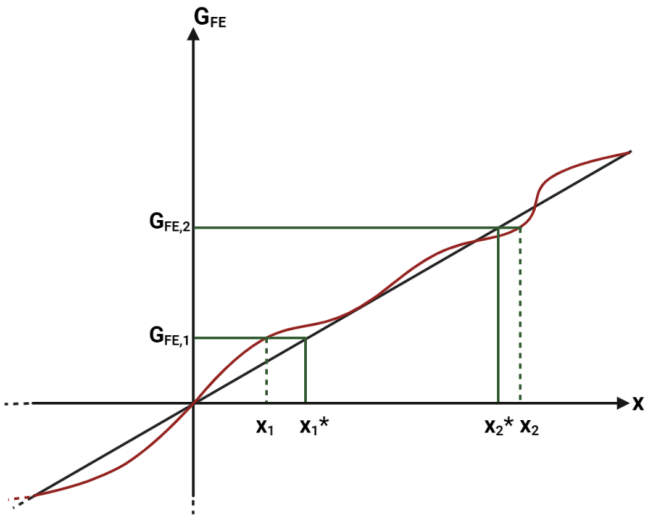

Figure 2.9: The black graph indicates the assumed linear read-out gradient, and the red graph the actual shape of the field distribution, where the presence of susceptibility-induced magnetic fields perturbs the linearity of the spatial encoding gradient. x indicates the true position of the spatial origin of the signal, and x^* indicates the position from where the MR acquisition mechanisms assume it originates.

As the spatial position is frequency-encoded during the read-out of the MR signal in an imaging process, a frequency shift induced by the field inhomogeneity will cause the origin of the measured signal to be assigned a different spatial localization along the frequency-encoding direction. The accumulated phase shift due to the local frequency shift is given by the relation

$$\Delta\phi(t) = \gamma\Delta B_0 t.$$

where t represents the time after the excitation pulse. For a conventional MR sequence with a line-by-line trajectory, a single line of k-space is sampled after an applied excitation pulse. Thus, each point along the phase-encoding direction in k-space will be sampled at equal time points after the excitation pulse. Consequently, the phase offset due to field inhomogeneity will be equal between subsequent digitized sampling points along the phase-encoding direction and will therefore not affect the phase evolution along the direction. Hence, the geometric distortion will primarily be seen along the frequency-encoding direction for line-by-line k-space trajectories, and there will technically be no image distortion in the phase-encoding direction. The spatial shift will correspond to the frequency offset that the wrongly positioned spins possess and will be evident in the reconstructed image if the induced frequency shift is larger than the defined frequency bandwidth for the imaging voxels.

MR sequences using a zig-zag k-space trajectory fills multiple lines of k-space after a single excitation pulse. The data points along the phase-encoding direction for equal k_{FE} will now be sampled at different time points after the RF excitation pulse. The susceptibility-induced phase errors will accumulate with time along the long echo train, causing the phase evolution along the phase-encoding direction to be altered. Thus, the field inhomogeneity can cause image distortion in both the frequency- and phase -encoding direction for MR sequences using zig-zag k-space trajectories, e.g., conventional echo-planar imaging (EPI) sequences. However, strong read-out gradients, corresponding to a high frequency bandwidth, are typically used in EPI sequences to achieve fast sampling of the MR signal. Thus, the image distortion along the frequency-encoding direction will largely be reduced. In contrast, due to the relatively slow movement along the phase-encoding direction, the effective pseudo-gradient along the phase-encoding direction will be significantly lower, causing the image distortion to almost entirely be along the phase-encoding direction (Deichmann, Josephs et al. 2002).

2.5 Reduction of Magnetic Susceptibility Artifacts

Approaches utilized to minimize susceptibility artifacts include sequence parameters optimization and the application of shimming techniques. Optimization of sequence parameters can reduce the signal loss and somewhat the image distortion in the reconstructed image, depending on the modification made in the imaging sequence. The signal loss due to local field inhomogeneities can be largely reduced with a spin-echo pulse sequence, where the acquired signal at TE will evolve with the intrinsic T_2 time. However, distortions during read-out can still occur for SE sequences (Brown et al. 1999). Depending on the information wanted to be obtained, there are situations where GRE sequences are required, e.g., BOLD fMRI. Regular GRE sequences do not include a refocusing pulse and will therefore be more sensitive to susceptibility-induced field variations in either imaging direction. Signal loss can be reduced in the reconstructed image for GRE sequences by shortening the echo time and by decreasing the voxel dimensions. Shortening the echo time will reduce the time at which the spin dephasing occurs, and reducing the voxel dimensions will limit the influence of field inhomogeneity across the voxel's dimension. Both parameter changes will effectively reduce the phase dispersion across the voxel and minimize the induced signal modulation (Brown et al. 1999). However, sequence parameter optimizations will also have their limitations. Reducing the echo time will greatly compromise the T_2^*-contrast in the image and the information gained about changes in the T_2^* value for different tissues. In addition, reducing the voxel size will affect the image quality as it effectively decreases the signal-to-noise ratio (SNR).

Sequence optimization can also make SE and GRE sequences more robust against geometric distortions. Increasing the frequency bandwidth per pixel will effectively decrease the effect that the susceptibility-induced frequency offset has on the image and thus reduce geometric distortions

along the frequency-encoding direction. The frequency bandwidth per pixel can be increased by directly increasing the gradient strength of the read-out gradient or by increasing the voxel dimension. However, increasing the strength of the read-out gradient for the same FOV and resolution will reduce the SNR in the image. In addition, increasing the voxel size will allow for more intravoxel dephasing, leading to signal loss. Generally, a compromise between geometric distortion and signal loss must be made when choosing imaging parameters to minimize the susceptibility effects in the image. Geometric distortions occurring along the phase-encoding direction for MR sequences using zig-zag k-space trajectories, can also be minimized by utilizing parallel imaging. Parallel imaging simultaneously collects the MR signals using multiple receiver coils, giving the possibility to reduce the length of the echo train used in EPI sequences by reducing the number of phase-encoding steps used, effectively increasing the frequency bandwidth along the phase-encoding direction (A.D. Elster and J.H. Burdette 2001; Weiskopf et al. 2004). Using parallel imaging can reduce the accumulated phase error in the measured MR signal and thus the presence of geometric distortions along the phase-encoding direction.

Both primary forms of susceptibility artifacts (signal loss and geometric distortion) can be reduced by directly increasing the B_0 homogeneity. Shimming is a commonly used technique that tries to improve the homogeneity of the applied background field by correcting for the present magnetic field inhomogeneities (A.D. Elster and J.H. Burdette 2001). Active shimming is applied to correct for the patient-specific field distortions generated due to the magnetization of the different tissues. Active shimming decomposes the apparent magnetic field into spherical harmonic basic functions and produces corresponding corrective magnetic fields by directing current through specialized coils placed in the MR system (Juchem et al. 2011; McRobbie et al. 2017). Field mapping can be performed to identify the weight needed for each harmonic term of the correcting fields and thus the current for each shim coil to best homogenize the magnetic field on a per-subject basis (A.D. Elster and J.H. Burdette 2001). However, the complex perturbing field patterns generated within the human body are hard to remedy with today's shimming technology due to their limited shaping capability (usually only spherical harmonics up to the second-order are available, but sometimes third-order terms as well) (Juchem et al. 2011). This is especially a problem in the prefrontal cortex, which is close to the frontal and ethmoid sinuses, and in the areas of the temporal lobes that are close to the sphenoid sinus, auditory air cavities, and air cavities within the temporal bone (Juchem et al. 2011). Much higher orders of the spherical harmonics would be needed to fully compensate for the induced locally highly variable field patterns. The degree of shim order is largely limited by the space within the MR core, where higher-order shimming needs a larger number of resistive shim coils (Wachowicz 2014). Thus, there will still be a presence of residual field inhomogeneity in the B_0 field even after the application of active shimming.

Today, research is done on multi-coil shimming techniques where multiple individually driven electrical shim coils are localized close to the shim volume (Juchem et al. 2011; Stockmann et al. 2016). The shimming of the volume is achieved through the superposition of each individual basic field shape created by the individual shim coils. Using a multi-coil system for shimming has proven to produce more flexible and complex magnetic field shapes, allowing for a repertoire of field shapes, including localized gradient patterns close to the individual coils (Juchem et al. 2011). This allows more complex field patterns in the human brain to be corrected. The multi-coil shimming technique has been shown to significantly reduce the field distortions present in the human brain at 7T, but some field variations will remain (Juchem et al. 2011; Stockmann et al. 2016).

Obtaining a better understanding of the characteristics of the induced perturbing field can be beneficial for optimizing the use of sequence parameters and gaining more insight into how the application and design of shimming techniques can be optimized to minimize the presence of B_0 inhomogeneity. This is especially important at higher field strength, where the generated perturbing field due to complex susceptibility distributions will be more severe.

2.6 Simulation of Susceptibility-induced Field Distortions

For optimization of sequence parameters and the shimming technique, it would be valuable to have a numerical method to rapidly quantify and simulate the susceptibility-induced field distortions caused by a spatial distribution of magnetic susceptibility. Thus, a numerical model can give valuable information for minimizing the susceptibility effects in the obtained images. This study utilizes a Fourier-based method to simulate the effects of the susceptibility-induced fields in MRI. When quantifying the induced magnetization, it is convenient to use the volume magnetic susceptibility given by Eq. 2.8. Consequently, Eq. 2.9 gives the total local magnetic field induction.

When a sample described by a magnetic susceptibility distribution, $\chi(\vec{r})$, is placed under a strong magnetic field, B_0, the induced field due to the magnetization distribution ($M(\vec{r})$) of the sample at position $\vec{r}$ is given by

$$\vec{B}(\vec{r}) \approx \vec{B}_d(\vec{r}) = \frac{\mu_0}{4\pi} \int_V \frac{1}{|\vec{r}-\vec{r}'|^3} \cdot \left(3\frac{\vec{M}(\vec{r}')\cdot(\vec{r}-\vec{r}')}{|\vec{r}-\vec{r}'|^2}(\vec{r}-\vec{r}') - \vec{M}(\vec{r}') \right) d^3r'. \tag{2.11}$$

Eq. 2.11 is obtained by solving Maxwell's equations, and it makes a dipole approximation where each element of the magnetization distribution is seen as an independent dipole. Therefore, the equation performs a first-order approximation of the dipole-dipole interaction where the contribution to the magnetic field at a point in the substance from quadratic or higher terms of $\vec{M}$ is neglected. The approximation is generally valid as most susceptibility values found within the human body are $|\chi| \ll 1$. In addition, the divergence of the integral evaluation at $\vec{r} = \vec{r}'$ is solved through the use of the Cauchy limiting process. Using the Cauchy limiting process effectively places the hydrogen nucleus in a Lorentzian sphere (Koch et al. 2006). A Lorentz sphere is an imaginary spherical shell surrounding the point of measurement that separates the field effects due to its microscopic configuration from the contribution of the surrounding molecules in the system (Wang and Liu 2015). Discrete atoms, molecules, and nuclei encountered at a microscopic scale generate susceptibility shifts that disrupt the concept of continuity in Maxwell's equations. By placing the point of measurement inside a Lorentz sphere, the field effects due to the discrete magnetic dipoles in the proton's immediate environment will be captured inside its interior, where random fluctuations of these fields are allowed, effectively canceling them out inside the shell. Hence, the point of measurement is placed inside an imaginary sphere of zero magnetic susceptibility, and the nearby magnetic environment is approximated by a continuum (Duyn and J. Schenck 2016; Marques and Bowtell 2005). Consequently, the magnetic susceptibility will be continuous at a microscopic scale, making the condition of continuity in Maxwell's equations valid both at a macroscopic and microscopic scale (Koch et al. 2006; Wang, Zhou et al. 2015).

The main magnetic field, B_0, is most commonly applied in the z-direction, making the z-component of the induced magnetization of the material the dominant component that deviates significantly from zero compared to its transverse magnetization components. Hence, only the z-magnetization and the z-component of the dipole magnetic field is important (Marques and Bowtell 2005). The expression for the induced magnetization when the dominance of the static field ($\vec{B}_0 = B_0\hat{z}$) is taken into account is given by

$$\vec{M} \approx M_z = \chi \frac{B_0}{\mu_0(1+\chi)} \approx \frac{\chi}{\mu_0} B_0. \tag{2.12}$$

The assumption $|\chi| \ll 1$, which is generally true for human tissues, is employed in the above equation. The expression for the z-component of the normalized ($B_{(z,d)}/B_0$) magnetic field perturbation due to induced magnetization of different tissues can then be obtained by inserting Eq. 2.12 into Eq. 2.11, which yields

$$\frac{\vec{B}_{z,d}(\vec{r})}{B_0} = \frac{\vec{B}_d(\vec{r})\cdot\hat{z}}{B_0} = \frac{1}{4\pi}\int_V \left(3\frac{\vec{\chi}(\vec{r}')\cdot(z-z')^2}{|\vec{r}-\vec{r}'|^5} - \frac{\chi(\vec{r}')}{|\vec{r}-\vec{r}'|^3} \right) d^3r' \equiv \int_V \chi(\vec{r}') D_z(\vec{r}-\vec{r}'). \tag{2.13}$$

$D_z(\vec{r})$ is the z-component of the unit dipole field and is given by

$$D_z(\vec{r}) = \frac{1}{4\pi}\left(\frac{3\cdot z^2 - |\vec{r}|^2}{|\vec{r}|^5} \right) = \frac{1}{4\pi}\left(\frac{3\cdot cos^2(\theta) - 1}{|\vec{r}|^3} \right), \tag{2.14}$$

where θ is the angle between the direction of B_0 and $\vec{r}$. The expression for the z-component of the normalized induced perturbing field given in Eq. 2.13, can easily be recognized as the convolution between the spatial susceptibility distribution ($\chi(\vec{r})$) and the function describing a dipole response ($D_z(\vec{r})$). By using the convolution theorem, the integral can easily be calculated in the Fourier domain through multiplication, and the problem is reduced to solving the expression:

$$\frac{B_z(\vec{k})}{B_0} = \chi(\vec{k}) \times D_z(\vec{k}), \tag{2.15}$$

where $\vec{k}$ is the coordinate position in k-space. In addition, $\chi(\vec{k})$ in the above equation is the $3D$ Fourier transform of the susceptibility distribution map while $D_z(\vec{k})$ is the Fourier pair of the dipole unit field that is defined in Eq. 2.14. $D_z(\vec{k})$ is defined in k-space as

$$D_z(\vec{k}) = \left(\frac{1}{3} - \frac{k_z^2}{k_z^2 + k_\rho^2}\right), \tag{2.16}$$

where $k_\rho^2 = k_x^2 + k_y^2$ (Schäfer et al. 2009). The characteristics of a theoretical point-dipole field distribution in image space and the k-space definition of the dipole kernel in the $k_z - k_\rho$ plane is illustrated in Fig. 2.10. Fig. 2.10b indicates the characteristics of the convolution kernel used.

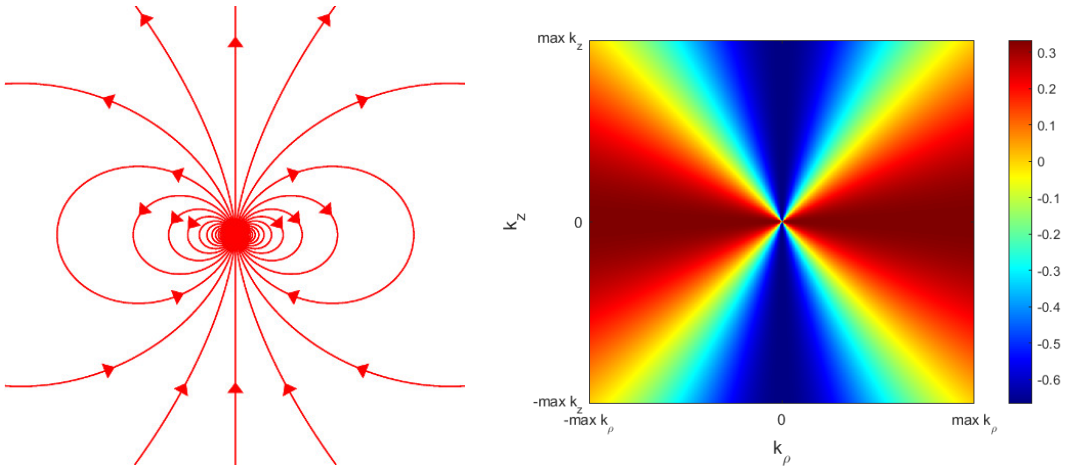

(a) (b)

Figure 2.10: (a) Field lines of a theoretic magnetic point-dipole (Griffiths 1999). (b) Simulated dipole kernel in k-space, $D(\vec{k})$. Eq. 2.16 was employed and the dipole kernel was described on a $570 \times 570 \times 570$ matrix with an isotropic resolution of 0.75 mm. The kernel illustrates variation of the dipole field with k_z and k_ρ.

Eq. 2.16 is not defined for k equal to zero (the center of k-space) or infinity, and are therefore not valid in the center of k-space. The value of the dipole kernel at $k = 0$ effectively specifies the average value of the dipole field over the whole calculation volume. Hence, $B_z(\vec{k} = 0)$ defines the averaged field offset due to the susceptibility-induced field for the whole calculation volume, which extends towards infinity for a continuous infinite Fourier transformation (Koch et al. 2006). In addition, it has been shown that evaluating the integral for the dipole function at $k = 0$ is equivalent to the calculation of the Lorenz sphere term (Cheng et al. 2009). As the Lorentz sphere term is already taken into account in the equation for the susceptibility-induced magnetic field (Eq. 2.11), it will be consistent with assigning the value of the dipole kernel at the center of k-space equal to zero. Furthermore, assigning the value of $B_z(\vec{k} = 0)$ to zero makes the reasonable assumption that the perturbing magnetic field infinitely far away is zero, which, conveniently, will have the consequence of satisfying the boundary conditions at the edges of the calculation volume.

The Fourier-based method can easily simulate the induced field that alters the homogeneity of B_0 by multiplying the $3D$ representation of the dipole kernel with the $3D$ spatial susceptibility distribution in the Fourier domain and subsequently taking the $3D$ inverse Fourier transform back

to the spatial domain. The $3D$ map of the susceptibility distribution includes the geometry of structures included in the sample. In addition, the dipole interaction described in Eq. 2.14 changes as $(3 \cdot cos(\theta) - 1)$, where θ includes the information about the orientation of the structure relative to B_0. The induced field distortions will therefore depend both on the shape of the structure, and its angle to B_0, which was further noticed in the previous study made (Schmidt 2021).

2.6.1 Digitization and Discretization Effects

The expressions for the dipole kernel and the susceptibility-induced magnetic field distribution described in Section 2.6 were attained based on infinite field-of-view (FOV), corresponding to the integration over an infinitely large space. However, in practice, the description of the input susceptibility distribution used in the Fourier-based method is discretized onto a matrix of finite size and resolution. The expression for the dipole kernel must also be defined on a discretized matrix to obtain consistency with the discrete input susceptibility distribution. Thus, to rapidly calculate the susceptibility-induced magnetic field over a finite range, the Fourier-based method utilizes discrete fast Fourier-transformation (DFFT), having the consequence of violating the continuum analysis within the solution space (Koch et al. 2006). The finite arbitrary susceptibility distribution and Fourier transformation will introduce errors in the FFT calculation seen as (a) aliasing and (b) truncation artifacts in the obtained images:

(a) Aliasing corresponds to the overlapping of signals outside the FOV onto the image near its edges. Applying FFT over a limited calculation volume introduces a periodicity in the reconstructed image function. The introduced periodicity of the solution space can give rise to aliasing artifacts where periodic neighboring images influence the obtained image. The artifact is most evident at the edges of the calculation volume. As the dipole field, which is utilized in the Fourier-based method, is relatively long-range, the method will be prone to aliasing artifacts. Generally, the aliasing effect will become more noticeable and affect the obtained values of the calculated field offset more significantly when the object size becomes comparable to the size of the FOV.

(b) Truncation artifacts, also known as Gibbs-ringing artifacts, arise in the Fourier-based method due to the input susceptibility-map being a finite matrix representing, resulting in a truncation of the Fourier series used to reconstruct the image function (Liang and Lauterbur 2000). There will be insufficient data to perfectly reconstruct the image function, and the FFT calculation error due to truncated Fourier series will manifest itself as amplitude oscillation of alternating higher and lower intensities throughout the computation volume (Liang and Lauterbur 2000). Gibbs-ringing artifacts are most pronounced adjacent to the sharp interfaces. The discrete nature of the susceptibility boundaries of the input susceptibility-map will significantly increase the Gibbs-ringing artifact as the discretization of boundaries effectively increases the surface areas (Koch et al. 2006). The discretized surface boundaries will also obtain angles to the applied field, B_0, causing interference between the generated intensity oscillation artifacts (Koch et al. 2006).

Aliasing and Gibbs ringing artifacts can be minimized in the Fourier-based method by increasing FOV and the spatial resolution, respectively. However, increasing both FOV and the spatial resolution will dramatically increase the computation time as it effectively increases the matrix size of the computation volume. Compromises must therefore be made. The effects of FOV and resolution on the accuracy of the Fourier-based method were analyzed in the thesis by Schmidt 2021.

Chapter 3

Methods

Experimental data for this thesis was acquired on a 7T Siemens MAGNETOM Terra scanner located at St. Olav's hospital in Trondheim, Norway. A 32-channel head coil was used for signal reception for all measurements performed. The acquired DICOM images was converted to NiFTi files using MRIcrone. All simulations were implemented and performed in MATLAB R2020a (The Mathworks Inc., Natick, MA), on a Windows 10 Home PC with 2.10 GHz AMD Ryzen 5 mobile processor and with 6.94 GB usable RAM. The main functions used for the simulations are found in Appendix A. Imaging of, in total, three healthy volunteers were carried out with informed consent. The first two measurements were used to optimize the acquisitions and sequence parameters, and thus only results from the last measurement is shown in the thesis (Appendix B).

3.1 Segmentation of Anatomical Image

The Fourier-based model is based on a subject-specific input susceptibility map for calculating the frequency offset. Thus, information about the location and shape of the different tissues is needed in the model and was obtained by applying a segmentation tool to a high-resolution anatomical dataset of the subject.

For a healthy volunteer, a MP-2RAGE sequence was acquired to obtain detailed anatomical images. Isotropic resolution of 0.75 mm and a FOV of 168 mm $\times$ 255 mm $\times$ 252 mm was used. The TE and TR values were set to be 1.99 ms and 4300 ms, respectively, and the applied sequence used TI1/TI2 of 840/2370 ms. The image slices were acquired with no initial rotation, and the acquired images with distortion correction of the spatial gradients turned off was used. Subsequently, the high-resolution anatomical images was used for differentiation and localization of the main different tissue types present within a human head. For this thesis, the Statistical Parametric Mapping 12 (SPM12) software was used to segment the $T1$ weighted anatomical MP-RAGE image acquired with the second inversion time. The segmentation toolbox in SPM12 uses an in-build algorithm that classifies the subject's data into several different tissue types according to the tissue probability map (TPM). TPM defines the probability of finding a tissue at a given location.

Before applying the segmentation algorithm, some preprocessing was performed on the image to improve the accuracy of the anatomical image segmentation. In SPM12, the origin of the template space, the location $[0, 0, 0]$, is set at the anterior commissure. The anterior commissure is a white matter tract connecting both brain hemispheres. To better align the input anatomical image (subject space) with the TPM (template space), the origin of the anatomical image was reset to be located at the same relative position within the human brain as for the template space. Thus, the origin of the subject space was reset to be located at the anterior commissure. The position of the anterior commissure was identified using the combined image achieved from the MP-2RAGE sequence due to its superior grey to white matter contrast. However, it is the MP-RAGE image with the second inversion time that was being used in the segmentation step.

After the pre-processing step of the anatomical images, the segmentation of the images into different tissue types was achieved by applying the segmentation algorithm in SPM12. Several input parameters to the segmentation algorithm can be specified. Finding the best input parameters is a matter of empirical exploration and will be dependent on the desired outcome one wishes to achieve from the segmentation. As emphasized in Appendix C, the results of the segmentation step are relatively largely affected by choice of the initial parameters. A relatively smooth intensity modulation artifact was observed across the acquired MP-RAGE image. Thus, a lighter bias regularisation was chosen to account for this artifact in the segmentation algorithm. Doing so will prevent the algorithm from modeling the intensity variations as being due to different tissue classes. However, choosing very light regularisation will give poor results for the air segmentation (Appendix C). The parameters that were used in the segmentation step for the final results are indicated in Table 3.1. The tissue probability map used in the segmentation step was the *TPM.nii*, which is included in the SPM12 software package. *TPM.nii* classifies the tissues of the anatomical image into grey matter, white matter, cerebrospinal fluid (CSF), bone, soft tissue, and air/background (Ashburner et al. 2021). Accurate segmentation between bone, air, and soft tissue is mainly focused on in this thesis. Grey matter, white matter, and CSF are assumed to have susceptibility values of soft tissue, and precise segmentation between these tissue compartments is therefore not heavily weighted.

Table 3.1: Input parameters for the segmentation algorithm in SPM12.

Parameter	**Value**
Bias regulation	Very light regularisation (0.0001)
Bias FWHM	60 mm cutoff
Tissue Probability map	TPM.nii
Number of Gaussians	Grey Matter: 2
	White Matter: 2
	CSF: 2
	Bone: 3
	Soft tissue: 4
	Air: 2
Native tissue	Native space
Clean Up	Light Clean
Affine Regularisation	ICBM space template - European brains
Sampling distance	3
Deformation Fields	Forward

The SPM12 segmentation toolbox gives the probability maps for the location of each tissue type segmented as output. Due to partial volume effects, a voxel can be given a relatively high probability for multiple tissue types. Thus, the obtained probability maps from the SPM12 segmentation step were later compared with each other, voxel by voxel, where the voxel was given the tissue type with the highest probability.

3.1.1 Segmentation Using UTE Dataset

Segmentation between air and bone is difficult to achieve with data from conventional MR sequences, e.g., MP-RAGE, as air produces no signal while bone produces little to no detectable signal. The differentiation between the two compartments is especially challenging in brain regions

with anatomical air cavities surrounded by bone tissue (e.g., sinuses, auditory cavities, and air cavities within the temporal bone). Consequently, correct segmentation between air and bone will be hard to achieve with conventional MP-RAGE images and the SPM12 segmentation program. Using an UTE sequence with TE values that are remarkably less than those of conventional sequences allows tissues with very short T_2 values to be detected, and differentiation between air and bone can be achieved. Thus, a single echoed UTE sequence was applied in addition to the MP-2RAGE sequence to obtain further information for the segmentation of tissues.

A non-clinical UTE sequence under development (Stefan Sommer, Siemens Healthineers), was acquired with a 0.75 mm isotropic resolution and an isotropic FOV of 252 mm in each spatial dimension. The repetition time and echo time were 3.25 ms and 0.05 ms, respectively, and a small flip angle of 4° was used. Coronal images with no initial rotation were acquired, and distortion correction of the gradients was turned off to prevent any image scaling caused by the correction. The imaging volume was set to have an equal initial position as set in the MP-RAGE sequence to ensure structural alignment of the brain structures between the two subject spaces. However, a scaling of the reconstructed UTE images was observed when compared to the acquired MP-RAGE images. As described in Appendix D, a modification of the resolution in the DICOM header file was executed to achieve structural alignment between the two acquired images. The resulting UTE image showed a significant overlay with the MP-RAGE image and could be used for further air segmentation.

The probability map for the air segmentation obtained from the SPM12 was overlaid onto the modified UTE images, where the superior air-bone contrast in the UTE images was utilized for further air segmentation. The 3D slicer software was used for the manual segmentation. The software was also used to remove extrusions, fill holes and smoothen the achieved bone and air segmentations. A median smoothing filter of 1.5 mm was applied. As a final product, a relatively representable subject-specific tissue map defining the location of the segmented tissues was achieved.

The established pipeline for deriving a subject-specific tissue distribution map is indicated in Fig. 3.1. The top row indicates the automatic tissue segmentation performed on the MP-RAGE image using SPM12, and the bottom row the use of the UTE data to refine the air segmentation manually. The spatial resolution of the anatomical images on which the segmentation was performed was unchanged, and the structure of the tissues was therefore defined using cubic voxels of 0.75 mm.

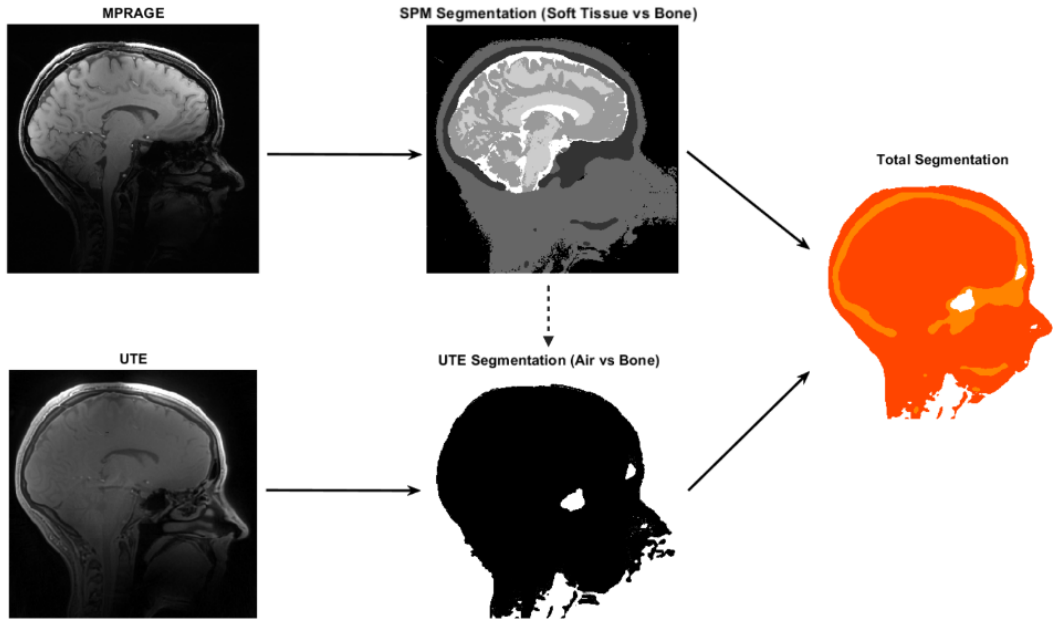

Figure 3.1: The pipeline for the segmentation of the main brain tissues. The output is a susceptibility map where air, bone and soft tissue (including grey matter, white matter and CSF) is spatially segmented and given their corresponding susceptibility value.

3.2 Frequency Offset

The achieved subject-specific tissue map, defining the voxel-wise positions for each tissue class segmented, was used to construct a three-dimensional matrix representing the spatial distribution of the magnetic susceptibilities within the subject (Output in Fig. 3.1). The susceptibility values for grey matter, white matter, CSF, and soft tissue deviates only slightly from each other, and their susceptibility effects are most often not apparent in the obtained MR images (Collins et al. 2002; Schäfer et al. 2009). Thus, the locations for grey matter, white matter, CSF, and soft tissue obtained from the segmentation step were all given the susceptibility value of soft tissue. The susceptibility values that were used in this thesis are in accordance with those found in J.F. Schenck 1996 and are presented in Table 3.2.

Table 3.2: Susceptibility values of bone, soft tissue and air, presented in parts-per-million (ppm) (J.F. Schenck 1996)

Structure	χ **[ppm]**
Bone	-8.86
Soft tissue	-9.05
Air	0.36

Before applying the numerical model to the susceptibility distribution characterizing the subject, $\chi(\vec{r})$, the effective FOV for the subject-space was increased. The FOV was changed to be 427.5 mm $\times$ 427.5 mm $\times$ 427.5 mm by adding a buffer region between the object of interest and the edge of the simulation matrix, effectively increasing the matrix size, without changing the spatial resolution. The matrix size was increased to $570 \times 570 \times 570$. The padding of the original three-dimensional matrix containing the information about $\chi(\vec{r})$ is performed to minimize the aliasing effect, caused by the infinite repetition of the susceptibility distribution generated by using the discrete fast Fourier transformation (Section 2.6.1). Thus, applying a buffer region will move the repeated images further away from the central region of interest. Due to computational limitations, large matrix sizes could only be achieved by using single precision instead of double-precision matrices as it requires less computational memory. The difference in using single versus double precision and smaller versus larger matrix sizes with an equal resolution of 0.75 mm, was analyzed in Appendix E. The difference in the quantified frequency offset values when using single compared to double precision was insignificant compared to the gain achieved by using a larger matrix size. Thus, single-precision matrices are used for the model in this thesis, such that aliasing effects can be minimized.

The susceptibility-induced field distribution given in Eq. 2.13 was calculated at each point using the Fourier transformation. The description of the susceptibility map in the Fourier domain ($\chi(\vec{k})$) was achieved by applying a three-dimensional DFFT. The spatial resolution, Δr, of the matrix, was 0.75 mm (unchanged from the MP-RAGE dataset) in each spatial direction. Truncation effects, which are enhanced by the discretization effects of the model, were reduced through apodization of $\chi(\vec{k})$. The apodization of $\chi(\vec{k})$ was achieved by element-wise multiplication of $\chi(\vec{k})$ with a raised cosine filter. The raised cosine filter was set to have a roll-off value (β) equal to 0.9, giving an almost Gaussian low-pass filter that effectively smoothens the susceptibility distribution in k-space. In addition, the filter is described using polar coordinates, making it rotationally uniform. Subsequently, following Eq. 2.15, $B_z(\vec{k})$ was calculated by element wise multiplication of the kernel describing the field distribution for a theoretical dipole in Fourier domain (Eq. 2.16) with $\chi(\vec{k})$. The value of the dipole field at the center of k-space, $D(\vec{k} = 0)$, is undefined and was set equal to zero, such that the total map of generated field distortions averages to zero in real-space (Schäfer et al. 2009). Finally, the inverse Fourier transformation was applied, and the susceptibility-induced field distortions in real space were obtained. The results were scaled to Hertz by using the Larmor relationship given in Eq. 2.1. Thus, the simulated frequency offset is obtained. The main magnetic field was orientated in the inferior-superior direction for the performed simulations using the Fourier-based method.

Two field maps, one with standard shim mode and the other with a tune-up shim mode, were acquired to validate the results from the numerical model. Field maps measure the in vivo field inhomogeneity present and will therefore be the ground truth for the frequency offset map. The tune-up shim mode does not involve any additional subject-specific shimming, whereas the standard shim mode includes the application of the subject-specific static shimming. Field maps with tune-up shim modes were acquired as the numerical model does not include any effects from shimming. However, the acquired field map with no subject-specific shimming will also include field inhomogeneities caused by other factors than the susceptibility differences. Thus, a field map with standard shimming was also acquired. Other than the difference in shim mode, the two field maps had equal acquisition parameters with 1.5 mm isotropic resolution and TR=901 ms. The two complex images were acquired at the echo times TE1 = 4.08 ms and TE2 = 5.1 ms, giving an echo spacing of 1.02 ms. The read-out bandwidth for both sequences was 402 Hz/Px. As for the MP-RAGE image, the acquired slice images in the field maps sequences were taken in the sagittal plane with no initial rotation. Equal orientation and position between the field maps and the MP-2RAGE scans were ensured such that image slices at corresponding positions in the scanner-based coordinate system could more easily be attained and compared. The reconstructed field map image was scaled to have values in the interval [-π,π], before the frequency offset was attained by utilizing Eq. 2.7. The corresponding magnitude images were used to remove the noise outside the imaging volume in the field map images. In addition, due to strong phase-wrapping observed in the tune-up dataset, a phase-unwrapping algorithm found in the FSL software was applied for at the tune-up dataset. Thus, unwrapped images for the brain region were derived for the tune-up field map dataset. The mask of the brain region used in the phase-unwrapping step was saved and applied for later masking of the brain region.

To be able to calculate the difference between the reference frequency offset value (field map) from the simulated value (model), the 3D matrix storing the information from the field map imaging sequences was interpolated using the in-build Matlab function, *interp3*. The cubic interpolation method was used. The FOV was unchanged, but the resolution was increased to 0.75 mm by the interpolation step. The mask of the brain region obtained from the phase-unwrapping step was also interpolated to gain a mask of the brain region that can be applied to the numerical model. After the interpolation step, the 3D matrix containing the simulated frequency offset was re-scaled to the size of the 3D matrix storing the interpolated field map data, such that each matrix contained the information from corresponding positions in the scanner-based anatomical coordinate system (Brainder n.d.). Subsequently, the error of the model's estimation was calculated by taking the difference between the reference value, defined by the field map, and the model's estimated frequency offset value.

To better compare the numerical solution with the experimental values, the root-mean-square error (RMSE) was calculated for defined regions of interest (ROIs), for each transverse image slice, and for the whole brain region. Two ROIs were defined in a narrowed region within the transverse image slice, located above the nasal cavity, and the sphenoid and ethmoid sinuses, where strong frequency offset values are expected. ROI1 was taken at a level in the inferior-superior direction close to the air cavities. ROI2 was taken at an equal in-plane position but for a transverse slice located at a more superior position compared to ROI1. In addition, the RMSE was evaluated over the entire brain within the transverse slices for four ROIs divided in the inferior-superior direction: a region covering the lower brain region, the cerebellum, a region right above the nasal cavity, the sphenoid, and the ethmoid sinuses, a region covering the superior orbitofrontal cortex, and the upper brain region.

A flowchart showing the main steps performed for calculating the frequency offsets, both from the model and from the acquired field maps, is indicated in Fig. 3.2.

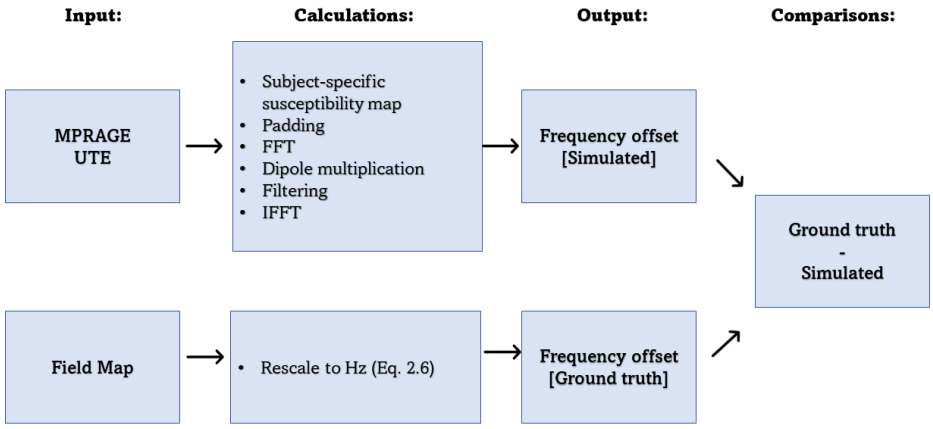

Figure 3.2: A flowchart indicating the step-wise procedure of calculating the in vivo frequency offset maps from the field map dataset (ground truth), and the model (simulation). A description of the different functions used during the calculation steps can be found in Appendix A.

3.3 Through-Slice Susceptibility Gradients

In addition to quantifying the frequency offset, estimation of the presence of in vivo through-slice susceptibility gradients, $G_{z,s}$, was performed. The value of $G_{z,s}$ was calculated using three different methods: (I) Non-linear least-squares fit of the acquired experimental data from a ME-GRE scan onto the corrected signal decay function given in Eq. 2.10, (II) linear fit of the acquired field map data, and (III) linear fit of the field offset predicted by the numerical model. A flowchart for the three different methods used to quantify the present $G_{z,s}$ is shown in Fig. 3.3.

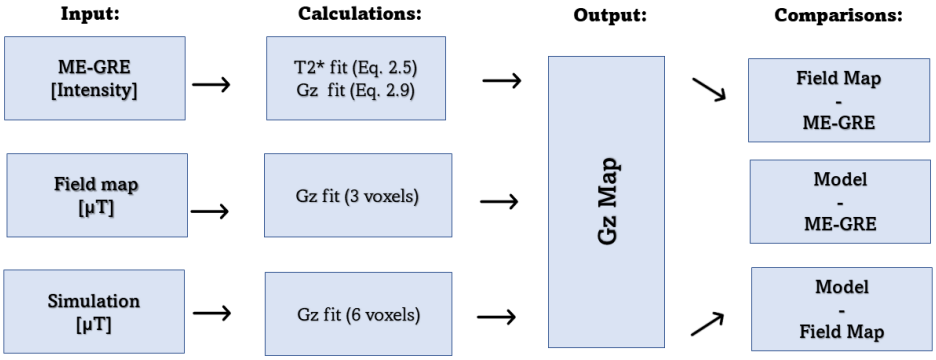

Figure 3.3: A flowchart indicating the step-wise procedure of obtaining $G_{z,s}$-maps from the ME-GRE dataset, the field map dataset, and the model (simulation). A description of the different functions used during the calculation steps can be found in Appendix A.

3.3.1 Quantifying $G_{z,s}$ From a Multi-Echo GRE Scan

As previously mentioned in Section 2.4.1, the theoretical model for the signal decay (Eq. 2.6) does not take into account the enhanced signal modulation induced by through-slice susceptibility gradients. Thus, an underestimation of the T_2^* will occur in regions where relatively strong $G_{z,s}$ is present when applying exponential fit to the theoretical model. This is especially a problem for imaging sequences with larger slice thickness, as larger slice thickness will make the sequence more sensitive to field inhomogeneities along the slice-select direction, causing the signal to decay more rapidly than described by the theoretical model. A modified signal decay function, corrected for

the presence of through-slice susceptibility-induced gradients, was introduced in Section 2.4.1 and is given in Eq. 2.10. The parameter $G_{z,s}$ in the given equation can be estimated by applying a non-linear least-squares fit of the experimental data acquired from a ME-GRE sequence onto the $G_{z,s}$-corrected signal decay function. The value of S_0 was not fixated to allow some flexibility in the model fit. However, to make the fit more focused towards the estimation of $G_{z,s}$, the value of T_2^* was fixated. Thus, the value of T_2^* was initially estimated by performing a fit to the simple monoexponential decay function within a defined region where little to no field inhomogeneity was expected. The initial estimate of S_0 and T_2^* in the model fit was calculated using the expression found in Hagberg et al. 2002 which is a geometric approximation of the area under the theoretical signal decay curve. By assuming that corresponding tissue types have equal T_2^* value, the value of T_2^* in the $G_{z,s}$-corrected model fit was conveniently fixated to the mean value of the T_2^* values calculated within the defined region with field homogeneity.

After fixating the value of T_2^*, maps of the estimated $G_{z,s}$ and S_0 values was derived for an image slice where an region with enhances signal loss was observed. The implemented non-linear least-squares fitting model for the ME-GRE datasets was initially validated and performed on a phantom before being applied to in vivo data (Appendix F). A ME-GRE scan with 0.75 mm isotropic resolution and an echo train ranging from 4 ms to 38.38 ms with an echo spacing of 3.82 ms was used in the phantom measurement. In addition to validation of the method, the difference in the obtained results when assuming a perfect, but not physically achievable, rectangular slice profile and when assuming a gaussian slice profile was also investigated in Appendix F. Only minor differences in the obtained results were observed. However, a small slice thickness was used in the phantom measurement, and the difference in the result is expected to be greater for larger slice thicknesses. In the continuing analysis, the sinc-corrected signal decay function, where a perfect rectangular slice profile is assumed, was used.

Two ME-GRE scans were performed on a healthy volunteer, one with standard and the other with a tune-up shim mode. Both ME-scans had a 0.75 mm isotropic in-plane resolution and a slice thickness of 4.5 mm, thus minimizing the effect of in-plane compared to the through-plane susceptibility gradients on the signal modulation. TR was set to 1200 ms, and a long echo train of ten echoes ranging from 3.10 ms to 40.95 ms with an echo spacing of 3.97 ms was used. The read-out bandwidth for each echo was 400 Hz/Px and the datasets with distortion correction turned off were used. The value of T_2^* was estimated within a defined $2D$-region of size 50×17 voxels located in the superior part of the brain where little to no field inhomogeneity was expected. The mean value of the estimated T_2^* values over the defined region was calculated and used for the model fit to the corrected signal decay function. Subsequently, the values of $G_{z,s}$ and S_0 were estimated for the entire imaging volume within a transverse image slice. The fitting process used an initial estimate of $G_{z,s}$ that was set equal to $1 \cdot 10^{-8}$T/m (close to zero). The inferior-superior position at which the maps of $G_{z,s}$ were derived was located at a level of the inferior frontal lobe, above the nasal cavity, and the ethmoid and sphenoidal sinuses. Thus, in an area where strong $G_{z,s}$ values are expected to be present.

The RMSE and the R^2 value for each performed fit were saved, and their mean value was calculated. For the estimation of $G_{z,s}$ the mean value of the goodness-of-fit statistics was calculated both for the entire masked brain region and for a defined ROI at size 172×47 located in the region above the nasal cavity, the ethmoid and sphenoidal sinuses, where the strong susceptibility gradients are expected.

3.3.2 Quantifying $G_{z,s}$ From the Numerical Model and a Field Map Scan

The in vivo values of $G_{z,s}$ were also quantified using the results from the numerical model and the datasets from the same two field map sequences used in Section 3.2. The method described in Section 3.3.1 assumed that the field gradients are linear across the voxel in the slice direction, which is a reasonable assumption for macroscopic field inhomogeneities. By assuming that the same assumption holds true over a distance equal to the slice thickness of the ME-GRE scan, a linear least-squares curve-fitting was performed on the datasets from the numerical model and the field map sequences to estimate the value of $G_{z,s}$. The applied linear model fit was a first-order

polynomial given as

$$y = p1 \cdot x + p2$$

where x is the position along the inferior-superior direction and y is the value of the field inhomogeneity at position x obtained from the numerical model and the field map datasets. Thus, *p1* will be the parameter $G_{z,s}$ that one wishes to quantify. The value of *p2* was not fixated to allow flexibility in the model fit. The field offset (field inhomogeneity) was given in μT for both the numerical model and the field map dataset, and the position of the slices, x, was given in the scanner-based anatomical coordinate system with units of m. Consequently, the estimated value of $G_{z,s}$ from the linear fits was given in units $\mu T/m$. Different slice thickness of 1.5 mm and 0.75 mm was used for the field maps and in the numerical model, respectively. Thus, a linear fit of six data points was made for the numerical model, and a fit with three data points for the field map datasets, having the consequence of estimating $G_{z,s}$ across a spatial distance of in total 4.5 mm (a distance equal to the slice thickness for the ME-GRE scans). The derived $G_{z,s}$-maps from the different datasets were calculated at the approximately equal inferior-superior position defined in the scanner-based coordinate system.

The mean RMSE and R^2 for the achieved linear model fits were calculated both for the entire brain region and within the same region of interest as defined in Section 3.3.1.

3.3.3 Comparison Between the Estimated $G_{z,s}$-maps

To evaluate the difference in the methods used to quantify the values of $G_{z,s}$, the difference between the acquired $G_{z,s}$-maps was attained. To do so, the $G_{z,s}$-maps obtained from the field map sequences were, to start with, interpolated to have the identical in-plane resolution as for the numerical model and the ME-GRE scan, which is of 0.75 mm. The difference in the numerical model's estimation of $G_{z,s}$ and the derived $G_{z,s}$-maps from the ME-GRE and field map datasets was attained, in addition to the difference between the ones obtained from the field maps against the ME-GRE datasets with similar shim mode. The non-linear least-squares model fit performed onto the ME-GRE dataset estimates the magnitude of the $G_{z,s}$ and does not give any information about its direction. Thus, the absolute value of the $G_{z,s}$-map derived from the numerical model and from the field maps were used when comparisons against the $G_{z,s}$-maps attained from the ME-GRE dataset was made. The difference between the estimated values for $G_{z,s}$ was calculated over the entire brain region at approximately equal locations in the scanner-based coordinate system. In addition, the RMSE between the estimated $G_{z,s}$-maps was evaluated over the whole brain region and for the previously defined ROI located above the nasal cavity, the ethmoid and the sphenoid sinus.

Histogram plots of the difference in estimated $G_{z,s}$ values, rounded to their nearest 50th value, were derived for each comparison made.

Chapter 4

Results

4.1 Segmentation

The air segmentation produced by the SPM12 software and the final air segmentation when additional information from the UTE images is used, is indicated in Fig. 4.1. A poor segmentation is observed for the one achieved using SPM12, where only minor parts of the frontal sinus are segmented as air. A significantly improved air segmentation is observed when adding manual air segmentation of the UTE images, with an especially clear benefit for the segmentation of the sphenoid sinus located below the temporal lobe, but also for the frontal sinus.

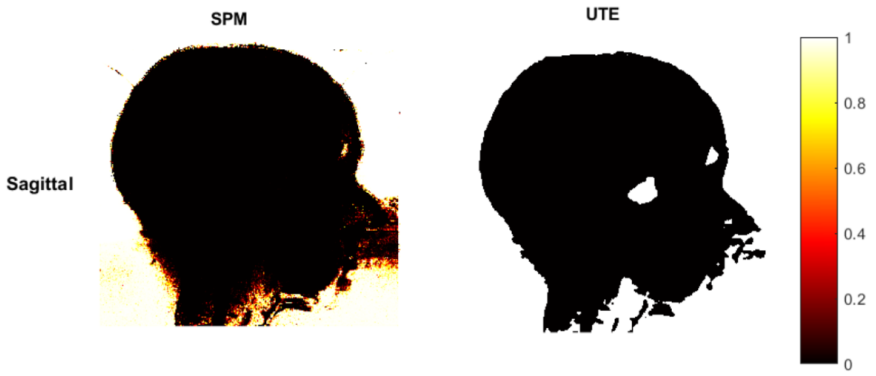

Figure 4.1: The probability map for the air segmentation obtained from SPM12, and the manual air segmentation obtained when utilizing the UTE data.

Fig. 4.2 indicates the air segmentation shown in the transverse plane in the location of the frontal sinuses and the corresponding generated frequency offset when the un-processed, heavily pixelated air segmentation is used compared to a smoothed air segmentation. The air segmentation obtained from SPM12 was heavily pixelated with multiple singular voxels segmented as air (see blue arrow Fig. 4.2). A heavily pixelated air segmentation in the numerical model is observed to induce multiple singular dipole fields generating highly variable and abrupt field variations in the affected area(blue arrow in bottom row Fig. 4.2). A noticeable improvement in the calculated field offset was observed when the extrusions were removed, and a uniform smoothing kernel of 1.5 mm was applied to the air segmentation. More smoothly varying field patterns are now observed around the air cavities. Thus, the additional processing of the air segmentation showed to be beneficial against discretization effects. However, care should be taken when applying such smoothing, as some extrusions can be due to anatomical structures and not caused by the pixelation of the air segmentation attained from SPM12.

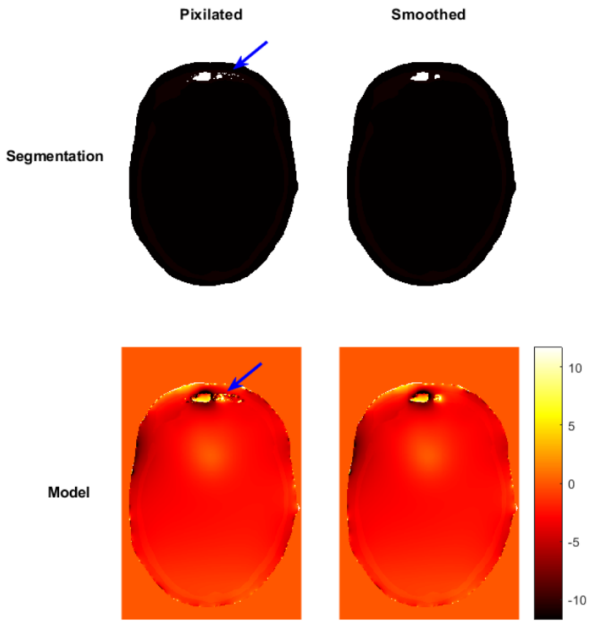

Figure 4.2: Segmentation of air and the corresponding simulated field offset shown in parts-per-million (ppm) for both a pixelated and a smoothed air segmentation. The arrows indicate the location of pixelation effects.

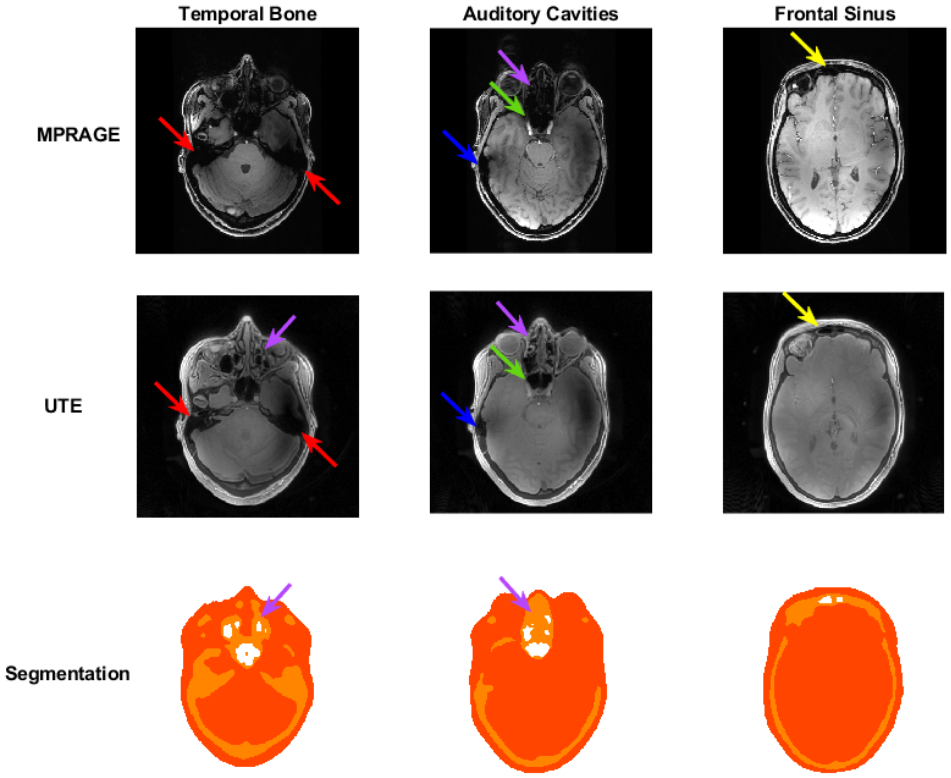

Figure 4.3: The high-resolution T_1 weighted MP-RAGE image, together with acquired UTE images and the susceptibility map for corresponding slices. The slices are taken at positions where the temporal bone region, the auditory cavities (the tympanic cavities), and the frontal sinus is indicated. The arrows indicate the position of air cavities surrounded by bone.

Fig. 4.3 illustrates the acquired MP-RAGE and UTE image in the transverse plane, together with the constructed tissue distribution map, at three different positions along the inferior-superior direction. The images in Fig. 4.3 are taken at positions indicating the temporal bone (the red arrows), the auditory cavities (blue arrows), also known as the tympanic cavities, together with the nasal cavity (purple arrows), ethmoid and the sphenoid (green arrows) sinuses, and at a position indicating the frontal sinuses (yellow arrows). Intensity modulation artifact is seen to be present in both the MP-RAGE and the UTE images. As expected, little to no differentiation between bone and air cavities is achieved by visual inspection for the conventional MP-RAGE images. A significantly improved air-bone contrast is observed in the UTE images, especially towards the anterior side of the human head. A differentiation between bone and air can now be visually achieved with the UTE images for most parts of the imaging volume (see purple, green and yellow arrows in Fig. 4.3). The benefit of the increased bone-air contrast in the UTE images is seen in the tissue segmentation map, where air cavities have been segmented for the corresponding regions. However, difficulties in differentiation between bone and air are still seen in the area of the tympanic cavity and within the temporal bone (see blue and red arrows in Fig. 4.3), which consequently affects the segmentation map where no air is segmented in these regions. In addition, some information about the localization of air is observed to be lost in the model for the nasal cavity and the ethmoid sinuses (see purple arrows in Fig. 4.3). The air cavities in these regions often have highly irregular surfaces and are relatively small, making it difficult to segment manually.

4.2 Frequency Offset

The acquired magnitude image, together with the original field map images with standard and tune-up shim mode, are shown in Fig. 4.4. The field map images are scaled to frequency and are shown in Hz. For both field maps, a strong positive frequency offset is evident in the regions adjacent to the sphenoid sinus (see blue arrows in Fig. 4.4). The observed frequency offset in the region is more extensive and prevalent for the field map sequence with standard shim mode. In addition, a long-range field gradient variation is observed along the inferior-superior direction for the tune-up field map, giving a pronounced negative frequency shift in the inferior parts of the brain and a noticeably large positive frequency shift at the superior end of the brain. The long-ranged gradient is significantly less present in the field map with standard shim mode, indicating that the application of subject-specific shimming corrected for the long-ranged field inhomogeneity.

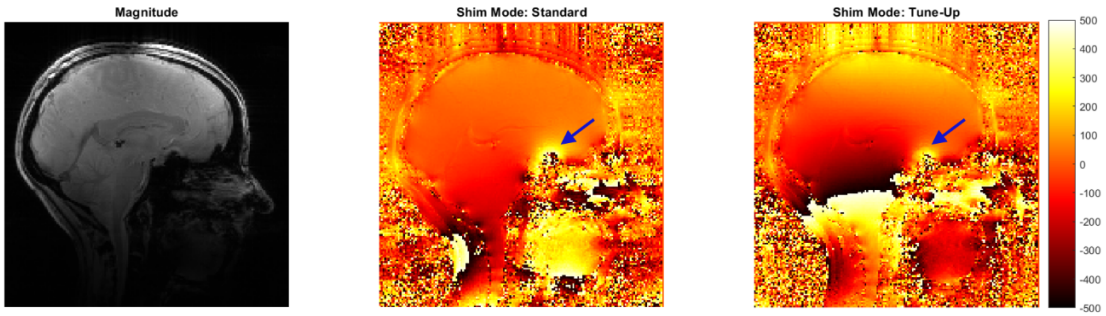

Figure 4.4: The magnitude and field map images, one with standard and the other tune-up shim mode, taken in the sagittal plane. The arrows indicate regions and features of interest in the images.

A clear phase wrapping is observed in the tune-up field maps in the lower parts of the brain, largely affecting the region where the cerebellum is located. The significant phase wrapping will give incorrect information about the frequency shift in the affected areas. Thus, the FSL's phase unwrapping algorithm was applied to the tune-up field map dataset. The original field map image and the resulting unwrapped image are indicated in Fig. 4.5. A clear improvement in the information about the frequency offset in the cerebellum region is observed.

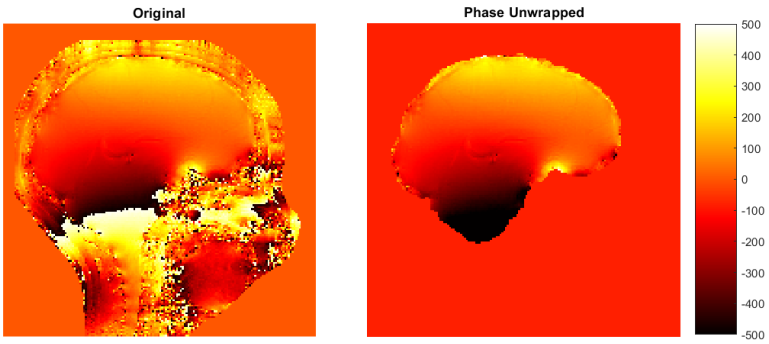

Figure 4.5: The original tune-up field map image and the obtained unwrapped image shown within the brain region.

Fig. 4.6 shows the frequency offsets calculated using the numerical model based on the subject-specific susceptibility map. A clear dipole field pattern is observed outside the imaging volume, with a more distorted quadrupole at the inferior end (see blue arrow in Fig. 4.6). The observed distorted quadrupole in the neck region is a consequence of the lack of segmentation of the anatomical structures in the region below the head and is not expected to be present in the actual situation where the upper body part is present. In addition, noticeable negative frequency offsets, giving a slight axial gradient, are observed at the posterior end of the neck region that has been segmented (green arrow in Fig. 4.6). The gradient seems to affect the inferior end of the brain region slightly. Furthermore, strong, positive frequency offsets are observed in the regions adjacent to the segmented air cavities, e.g., the nasal cavity, the sphenoid, and the ethmoid sinuses (see white arrows in Fig. 4.6). Frequency offsets due to curved facial structures (mainly at the anterior end) and the shape of the head (mostly seen at the posterior end) are also observed, indicating how the curvature of the head surface can induce frequency offsets. However, the frequency offset caused by anterior facial structures does not seem to extend into the brain region.

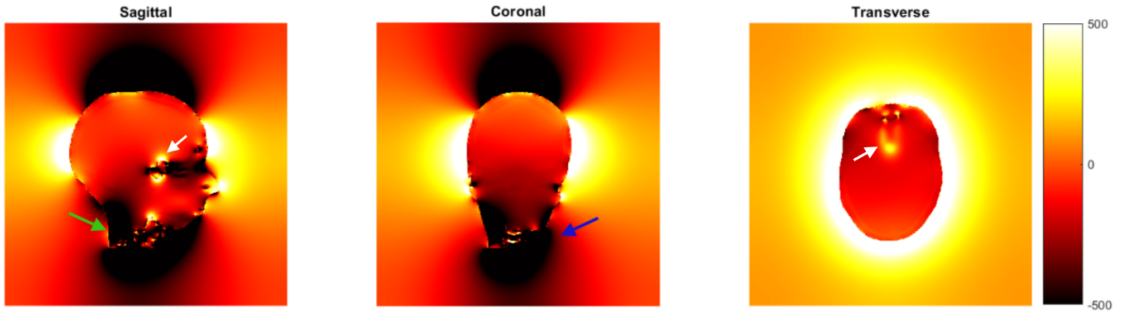

Figure 4.6: Simulated frequency offset obtained from the Fourier-based model where the input susceptibility map has been padded to a matrix of size $570 \times 570 \times 570$. The arrows indicate regions and features of interest in the images.

4.2.1 Comparison Between Field Maps and Numerical Model

The high-resolution anatomical MP-RAGE images are indicated in the top row in Fig. 4.7. The four transverse image slices are taken at different positions along the inferior-superior direction with an equal spatial distance between the image slices of 12 mm. The first two images are taken at levels indicating the temporal bone (light blue arrows in Fig. 4.7), and the tympanic cavities (light purple arrow in Fig. 4.7) together with the nasal cavity, ethmoid and sphenoid sinus (light green arrow in Fig. 4.7).

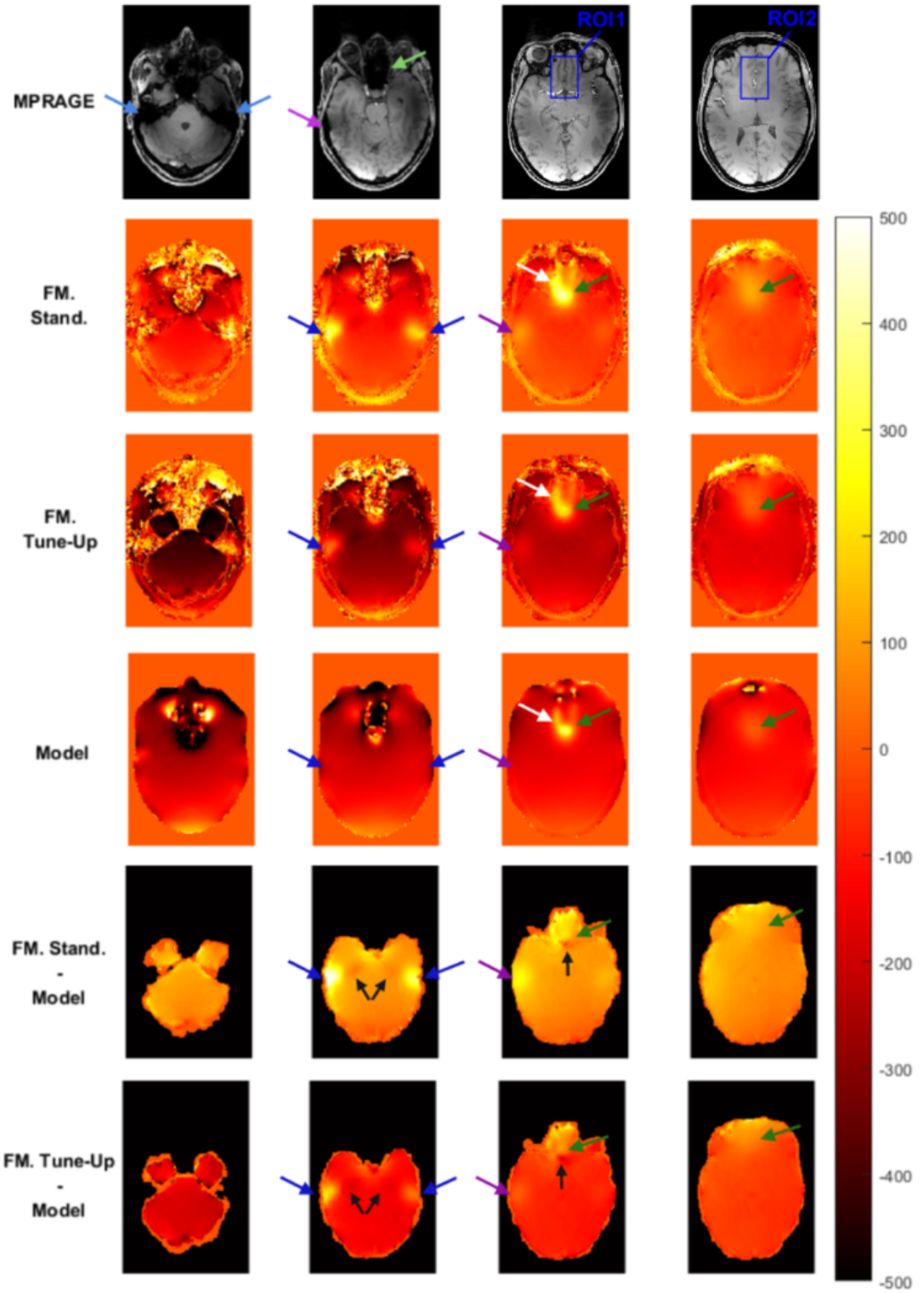

Figure 4.7: Transverse images at different positions indicating the location of the temporal bone and the auditory cavities (the tympanic cavity), in addition to the brain region right above and at a more distant level from the nasal cavity, the sphenoid and ethmoid sinuses. The top row indicates the high-resolution T_1 weighted anatomical images. The following rows indicate the measured frequency offset from field maps with standard and tune-up shim mode and the simulated frequency offset. The brain region of the FM with tune-up indicates the unwrapped data. The last two rows indicate the difference between the field map and the values obtained from the model evaluated within the brain region. The arrows indicate regions and features of interest in the images.

The last two image slices are taken at superior positions to the mentioned air cavities, more specifically at the level of the inferior frontal lobe and at a level of the upper part of the orbitofrontal cortex, where the frontal sinus is located in close proximity. The following rows indicate the measured frequency offset (both with standard and with tune-up shim mode) and the simulated frequency offset, together with the difference images taken between the field maps and the model's prediction within the brain region. The unwrapped data attained within the brain region is overlaid onto the original image for the field map with tune-up shim mode.

Noticeable positive frequency offsets are observed in the locations above the nasal cavity, the ethmoid, and the sphenoid sinuses (see dark green and white arrows in Fig. 4.7) for both measured field maps and for the model. General agreement in the shape, extent, and order of magnitude are observed for the induced frequency offsets between the datasets in the mentioned regions. However, looking at the difference images, the model seems to slightly underestimate the frequency offset for the locations above the nasal cavity and the ethmoid sinuses. In addition, the limitation of the air segmentation in the subject-specific susceptibility model for the temporal bone and tympanic cavity is clearly visible in Fig. 4.7, where the model strongly underestimates the presence of frequency offsets above these regions (see dark blue and dark purple arrows in Fig. 4.7). The underestimation is less prevalent when the model is compared to the experimental data with tune-up shim mode, and only a minor difference is seen above the tympanic cavity (see purple arrow in bottom row Fig. 4.7). Following the same observations made in Fig. 4.4, generally stronger local susceptibility-induced frequency offsets are observed for the field map with standard shim mode compared to both the field map with tune-up shim mode and the model's prediction, giving stronger underestimations of the model when looking at the difference images. When looking at the difference images between the model and the field map with standard shim mode, an underestimation of the frequency offset for the numerical model is seen throughout the brain region. In contrast, for the comparison against the field map with tune-up shim mode, an overestimation is observed for the numerical model. The observed overestimation is stronger for the more inferior slices indicated in Fig. 4.7. In addition, regions where the model slightly overestimated the frequency offset are seen in certain areas within the brain, indicated by the black arrows in Fig. 4.7.

Further analysis was made in the two ROIs indicated in Fig. 4.7, to evaluate the significance of the difference in estimated frequency offset between the numerical model and experimental values in more detail. The RMSE value evaluated over the two ROIs is shown in Table 4.1. A noticeably lower RMSE value is observed when the model is compared against the field map with tune-up shim mode.

Table 4.1: The RMSE values for the model's prediction of frequency offset compared against measured field maps (both with standard and tune-up shim mode), evaluated over two defined ROIs located above the nasal cavity, the sphenoid, and ethmoid sinuses.

Shimming	**ROI1 [Hz]**	**ROI2 [Hz]**
Standard	170	127
Tune-up	84	47

The RMSE values evaluated over the whole brain region for each transverse image slice were also calculated and are indicated as a bar plot in Fig. 4.8. The position of the image slices along the inferior-superior direction is given relative to the imaging volume's isocenter (position 0). A more uniform distribution of the RMSE values is seen for the situation when the model is compared to the field map with standard shim mode (the subplot to the left in Fig. 4.8). Much larger variations in RMSE values for each transverse image are evident for the comparison between the model and the field map with tune-up shim mode (the subplot to the right in Fig. 4.8). A more U-shaped distribution with significantly larger RMSE values towards the inferior and the superior ends of the brain is observed. The red dashed lines indicate the region where the model's prediction correlates better with the tune-up field map dataset compared to the one with standard shim mode, as indicated by their lower RMSE values within the region.

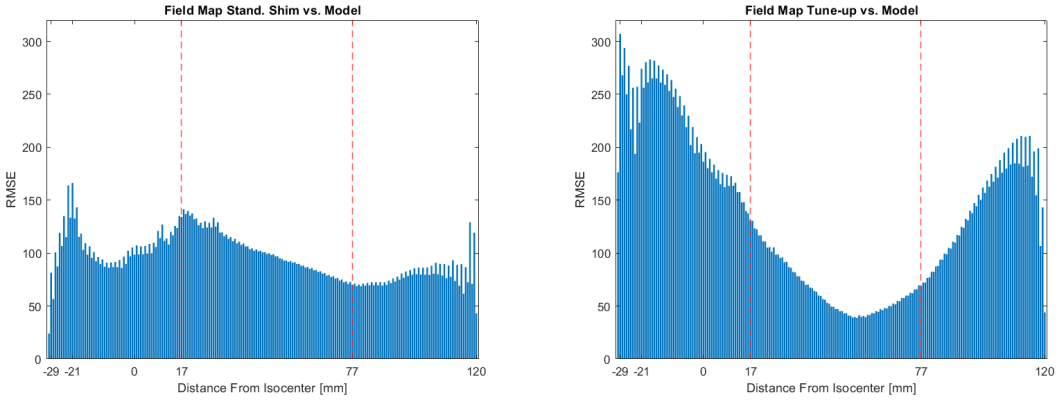

Figure 4.8: Bar plots of the RMSE values for the model's prediction of frequency offset compared to measured field maps (both with standard and tune-up shim mode) evaluated over the brain region for each transverse image slice. The area between the red dashed lines indicate the region where the model's prediction correlates better with the tune-up field map.

In addition, the total RMSE taken over the entire brain region was calculated for both comparisons made against the model's prediction and is indicated in Table 4.2. Slightly lower RMSE is observed for the comparison of the model against the field map with standard shim mode. The max value of RMSE, when calculated for each transverse image slice, and its corresponding spatial position along the inferior-superior direction relative to the isocenter of the imaging volume, is also presented in Table 4.2. The maximum RMSE is significantly larger for the comparison against the tune-up field map, and the position of the transverse image slices where the highest RMSE was evaluated are located in the inferior brain region (at the edge of the cerebellum) for both comparisons.

Table 4.2: The total RMSE value evaluated over the entire brain region, and the max RMSE value with its corresponding spatial position along the inferior-superior direction, for the comparisons of the model's prediction against the measured field maps (both standard and tune-up shim mode).

Shimming	**Total RMSE [Hz]**	**Max RMSE [Hz]**	**Pos. Max RMSE**
Standard	98	166	$\sim -21\,\mathrm{mm}$
Tune-Up	111	306	$\sim -29\,\mathrm{mm}$

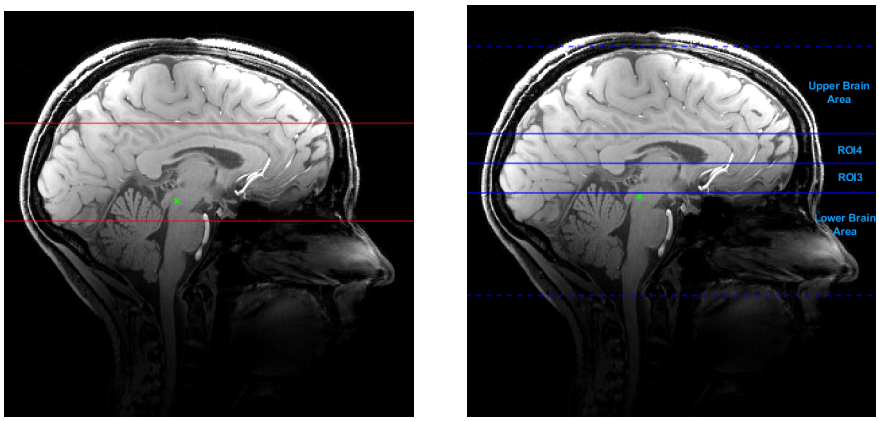

(a) (b)

Figure 4.9: High-resolution T_1 weighted image indicated in the sagittal image plane. The isocenter is indicated with a green cross. (a) the red dashed lines indicate the region where the model's prediction of frequency offset correlates better with the tune-up field map. (b) the four ROIs divided along the inferior-superior direction, for which RMSE values are evaluated.

The red dashed line in Fig. 4.9a indicates the anatomical region where the model corresponds better with the tune-up field map dataset than with the field map with applied shimming and are the same lines as the ones indicated in Fig. 4.8. The region is observed to cover important brain regions prone to strong and local magnetic field artifacts, e.g., the prefrontal cortex and the temporal lobes.

For further analysis, the RMSE value evaluated for the model against the field maps was evaluated over four regions of interest taken in the inferior-superior direction. The ROIs are indicated in Fig. 4.9b. An ROI covering the lower brain area where the cerebellum is located and an ROI covering the upper brain region relatively far away from air-tissue interfaces found within the head are defined, together with an ROI covering the brain region close to the air-tissue interfaces present in the lower brain region (ROI3) and an ROI more distant but still affected by the susceptibility-induced field gradients (ROI4). The attained RMSE values for the four different ROIs are presented in Table 4.3. Noticeably high RMSE values are observed for the comparison between the model and the field map with tune-up shim mode at the lower and upper brain regions. However, noticeably lower values of RMSE are seen for the same comparison in ROI3 and ROI4.

Table 4.3: The RMSE values for the model's prediction of frequency offset compared against the measured field maps, both with standard and with a tune-up shim mode, evaluated over four ROIs divided along the inferior-superior direction.

Shimming	**Lower Brain Area [Hz]**	**ROI3 [Hz]**	**ROI4 [Hz]**	**Upper Brain Area [Hz]**
Standard	120	107	90	76
Tune-Up	159	65	43	114

4.3 Simulation of Through-slice Susceptibility Gradients

4.3.1 Non-Linear Least-Squares Fitting to the Sinc-Corrected Signal Decay Function

The magnitude images acquired at every third echo time from the ME-GRE scans with standard and tune-up shim mode are indicated in Fig. 4.10. A noticeable enhanced signal loss is observed above the nasal cavity, the sphenoid, and ethmoid sinuses for both measurements (see green arrow in Fig. 4.10). Thus, the indicated transverse image slice was used to quantify $G_{z,s}$.

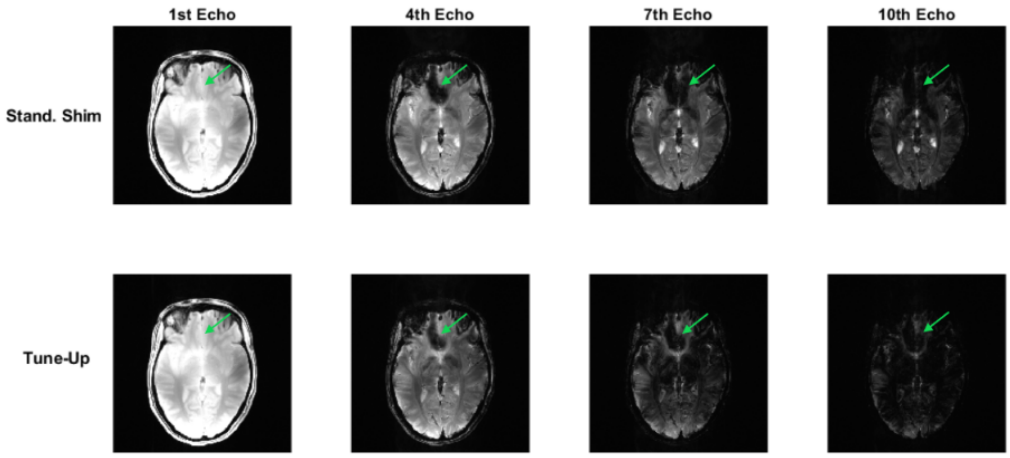

Figure 4.10: Transverse gradient-echo images acquired from the ME-GRE sequence (both with standard and tune-up shim mode) taken superior to the sphenoid sinus and the orbits. The green arrow indicates the region where a more rapid signal loss is observed.

Fig. 4.11 indicates the magnitude image acquired at the first echo taken in the superior region of the brain, together with the narrow area in which field homogeneity was assumed (the blue square in Fig. 4.11). Furthermore, the maps of the estimated S_0 and T_2^* values for the narrow region are also indicated. A pattern resemblance is observed between the magnitude image and the estimated S_0 map. Somewhat varying values of T_2^* are observed, where most of the values seem to lie in the range between approximately 25 ms and 35 ms. The mean value of the goodness-of-fit parameters for the performed fits is indicated in Table 4.4, together with the mean calculated T_2^* value. The observed outstanding goodness-of-fit values for the model fit indicate that the estimated values for S_0 and T_2^* are credible.

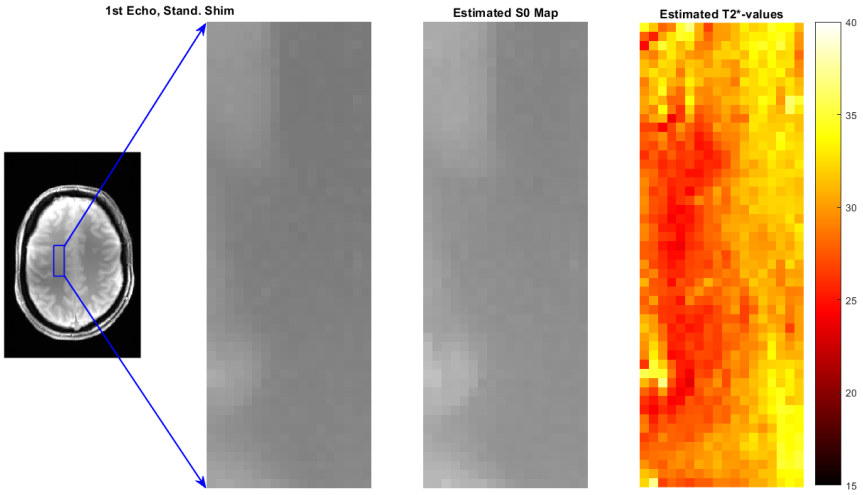

Figure 4.11: The transverse gradient-echo image acquired at the first echo time at TE = 3.1 ms taken in the superior brain region, in addition to a narrow region where non-linear least-squares fit to the monoexponential signal decay was performed. The maps of the estimated parameters, S_0 and T_2^*, are also indicated.

Table 4.4: The mean value of goodness-of-fit variables over the region where T_2^* was estimated, together with the mean calculated T_2^* value.

RMSE [intensity]	**R^2**	**Mean T_2^* [ms]**
9	0.997	29.7

Fig. 4.12 shows the result of the sinc-corrected model fit applied within the brain region for the image slice where an enhanced signal loss was observed. Maps of the RMSE, R^2, estimated S_0 and $G_{z,s}$ are indicated from left to right in the figure, respectively. The top row shows the result of the fits made to the ME-GRE dataset with standard shimming, and the bottom row for the model fit to the ME-GRE dataset with no static shimming applied (tune-up). In addition, the region of interest located above the nasal cavity, the ethmoid, and the sphenoid sinuses, is highlighted by a dashed blue box indicated in each image. The mean values of the goodness-of-fit statistics, evaluated over the entire region and within the defined ROI, for both model fits are shown in Table 4.5, together with the mean values of $G_{z,s}$ taken over the defined ROI.

In general, low RMSE and high R^2 values are seen for most parts of the brain region, with exceptions at locations where the ventricles and CSF tissue or blood vessels are expected to be located (see green arrows in Fig. 4.12). The regions of worse goodness-of-fit statistics are more prevalent for the model fit performed on the ME-GRE dataset with standard shim mode. Thus, worse goodness-of-fit statistics are obtained for both model fits when evaluated over the entire brain region than within the ROI. High correspondence between the two maps with estimated S_0 values is observed, and they show a pattern similar to what was seen for the magnitude image. In addition, high

values of $G_{z,s}$ are observed within the ROI, with a pattern similar to the one observed for the induced signal loss in the acquired magnitude images. As expected from previous results, the mean value of quantified $G_{z,s}$ within the ROI is seen to be higher for the dataset with standard shim mode (Table 4.5). Tissue contrast is observed in both $G_{z,s}$-maps, mainly outside the ROI, following a similar pattern to what is observed in the S_0 map. When comparing the two acquired $G_{z,s}$-maps, higher values of $G_{z,s}$ are seen to be estimated in most parts of the brain region for the model fit to the ME-GRE dataset with tune-up shim mode, as expected due to the presence of the large-scaled gradient. An area above the temporal bone with slightly lower values of $G_{z,s}$ is observed and is most likely due to the direction of the local susceptibility-induced field gradient being in the opposite direction of the long-ranged gradient, causing them to counteract each other.

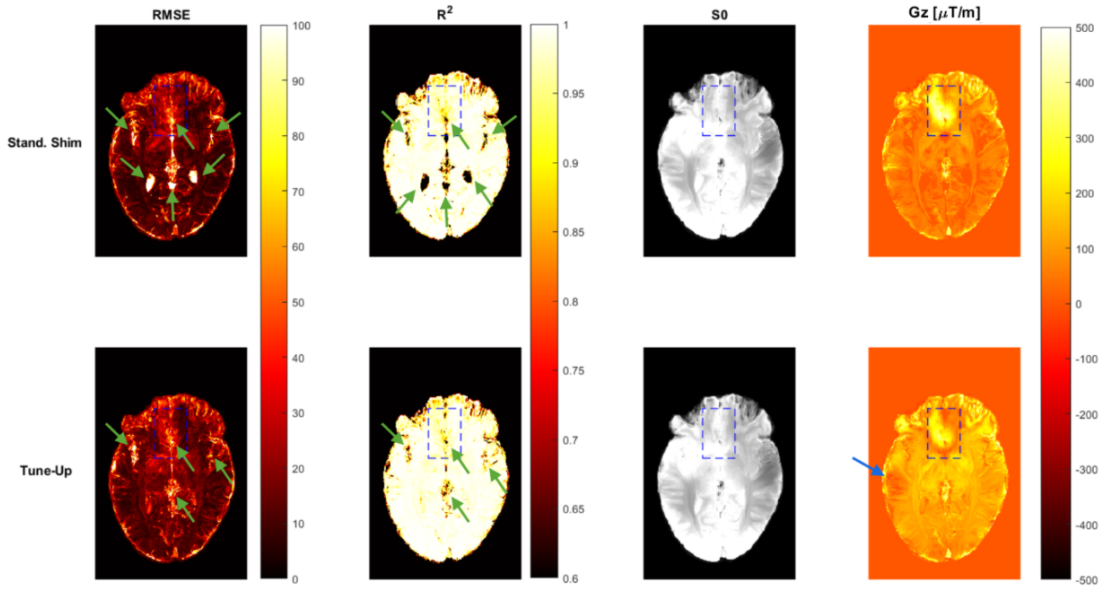

Figure 4.12: Maps of the RMSE, R^2 and estimated S_0 and $G_{z,s}$ values for the non-linear least-squares fits performed to the sinc-corrected signal decay function.

Table 4.5: The mean value of goodness-of-fit variables for the non-linear least-squares fit made to the ME-GRE datasets (both stand. shim and tune-up), evaluated over the brain region and for the ROI. In addition, the mean value of the estimated $G_{z,s}$ evaluated over the ROI is indicated.

Shim Mode	**RMSE [intensity]**		**R^2**		**Estimated $G_{z,s}$[μT/m]**
	Brain	ROI	Brain	ROI	ROI
Standard	21	27	0.67	0.94	194
Tune-Up	20	25	0.89	0.97	132

Fig. 4.13 indicates the non-linear least-squares model fits, both to the sinc-corrected (red curve) and the monoexponential (green curve) signal decay function, performed in a single voxel located in a region where a homogeneous field is assumed (4.13a), and for a voxel where a relatively strong value of $G_{z,s}$ was estimated (4.13b-c). A high degree of similarity is observed for the model fits in the voxel with a homogeneous field, where both seem to follow the evolution of the experimental data equally well. However, clear differences are observed between the two model fits for a voxel with a relatively strong $G_{z,s}$ present. The experimentally measured data shows a small re-growth in signal in the approximate time interval between 0.01 s and 0.025 s. The oscillations observed at later echo times seems to be most likely a noise floor as only small variations around relatively low intensities are seen. The monoexponential curve fit does not follow this feature and gives a rapid signal decay with unrealistically low values of T_2^* (3.9 ms and 5.3 ms for the fit to the shimmed and

tune-up dataset, respectively). A clear improvement is observed when applying the sinc-corrected model fit, which follows the shape of the re-growth in signal magnitude around the same time interval as where it was observed for the experimentally measured data.

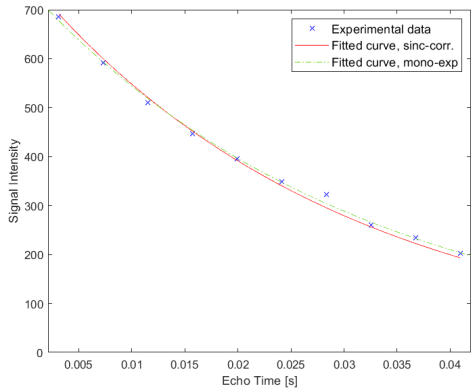

(a)

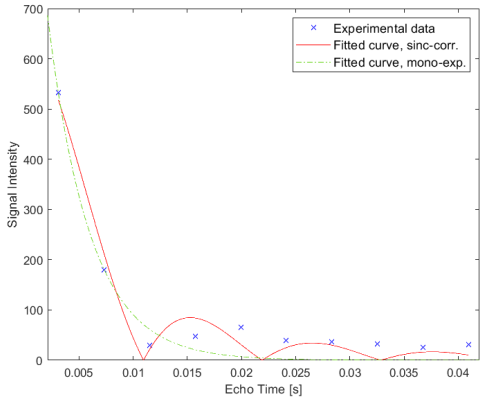

(b)

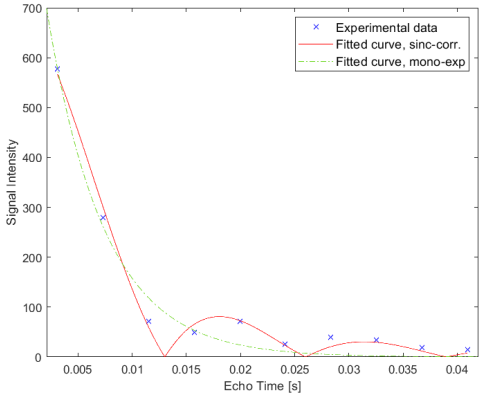

(c)

Figure 4.13: Results of the Non-Linear Least-Squares fitting performed in a single voxel to the experimental data obtained from a ME-GRE sequence. The green dashed curve is the fit made with a simple monoexponential decay model, the red curve is the result of the fitting made with a sinc-corrected signal decay function, and the blue crosses are the experimental data. (a) the results of the model fit in a voxel with a homogeneous field. (b) and (c) indicates the model fits in a voxel where a relatively strong value of $G_{z,s}$ is estimated to the dataset with standard shimming and tune-up, respectively.

4.3.2 Linear Fits

In addition to estimating the in vivo values of $G_{z,s}$ from ME-GRE scans, the presence of $G_{z,s}$ was quantified from linear fitting to the measured (field maps) and simulated (numerical model) field offset over an equal distance as the slice thickness used in the ME-GRE sequences. The goodness-of-fit statistics for the performed linear fits are shown in Table 4.6 together with the mean value of $G_{z,s}$ evaluated over the defined ROI. The linear fitting to the field offset attained from the numerical model shows far better goodness-of-fit statistics than for the fit made to the field map datasets. However, the RMSE value for the linear fit to both field map datasets is strikingly low compared to the order of the estimated $G_{z,s}$ values. Following the same trends as before, the mean value of $G_{z,s}$ is noticeably higher for the linear fit to the field map with standard shim mode compared to the other performed linear fits.

Table 4.6: The mean value of goodness-of-fit variables for the linear fit made for the measured field maps (both stand. shim and tune-up) and the model. The values are evaluated over the brain region and for the ROI. The mean value of the estimated $G_{z,s}$ evaluated over the defined ROI is also indicated.

Datasets	**RMSE** [μ**T**]		$\mathbf{R}^2$		**Estimated** $G_{z,s}$ [μ**T/m**]
	Brain	ROI	Brain	ROI	ROI
FM Stand.	0.2	0.1	0.63	0.80	146
FM Tune-Up	0.2	0.09	0.79	0.73	72
Model	0.02	0.01	0.91	0.95	94

4.3.3 Comparisons Between Derived $G_{z,s}$-Maps

The maps of quantified $G_{z,s}$ values from the different datasets are shown in Fig. 4.14. The absolute value of the $G_{z,s}$-map derived from the numerical model is also indicated. The bottom row in Fig. 4.14 indicates the difference between the $G_{z,s}$-map acquired from the numerical model (top row) taken against the $G_{z,s}$-maps acquired from experimentally measured data (middle row). The absolute value of the $G_{z,s}$-map from the numerical model is used for the comparison against the estimated $G_{z,s}$-maps from the ME-GRE dataset. The same ROI as defined in Section 4.3.1 is indicated in Fig. 4.14. The model's error in estimating $G_{z,s}$ compared to the other derived $G_{z,s}$-maps are only indicated within the brain region in the bottom row in Fig. 4.14. Significant offset values are seen close to the edges of the segmented brain region, especially for the comparisons made to the estimated $G_{z,s}$-maps derived from the field map datasets. The observation indicates that the masking of the brain region includes parts of the surrounding cortical bone, giving a noise-like pattern on the edges. Too little signal is measured from bone, giving a low SNR value, and a proper model fit in these regions can thus not be achieved.

The pattern of the quantified $G_{z,s}$ values within the ROI shows a striking similarity in the distribution pattern and order of magnitude between each $G_{z,s}$-map attained from the different datasets. However, some distinct differences are seen within the ROI for each comparison, including the noticeable overestimated value of $G_{z,s}$ for the numerical model at the location indicated by the green arrow in Fig. 4.14, and the underestimation seen towards the upper left part of the ROI (see white arrows in Fig. 4.14). The observed underestimated $G_{z,s}$ values within the ROI are most distinct when compared to the datasets with standard shim mode. In addition, the numerical model seems to overestimate the value of $G_{z,s}$ over a larger area in the ROI at the location above the sphenoid sinus when compared to the datasets with tune-up shim mode (see black arrows in Fig. 4.14).

When looking at the whole brain region, a greater heterogeneity of quantified $G_{z,s}$ values are seen in the maps obtained directly from experimental measurements (field map and ME-GRE), compared to the one obtained from the numerical model. This is further highlighted when looking at the difference images. Particular areas where the numerical model seems to more noticeably underestimate the $G_{z,s}$ values are indicated by the green, blue and purple arrows in Fig. 4.14, and are located at correspondingly approximately equal locations in each comparison. However, for the difference image between the numerical model and ME-GRE dataset with tune-up shim mode, a slight overestimation of the gradient strength is observed in the region indicated by the blue arrow. In addition, the model underestimates the strength of $G_{z,s}$ throughout most parts of the brain region compared to tune-up shim datasets (both for field map and ME-GRE).

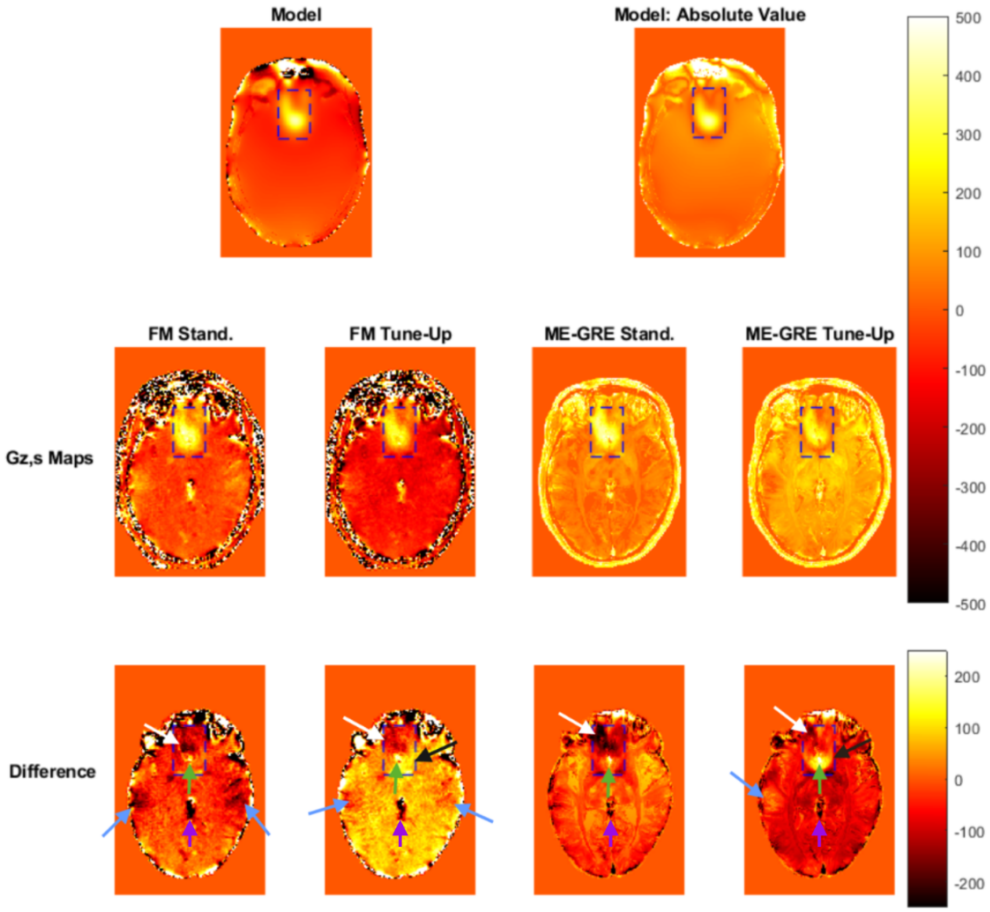

Figure 4.14: The $G_{z,s}$-maps attained from the model, the field map datasets, and the ME-GRE datasets. The absolute value of the quantified $G_{z,s}$ values from the numerical model is also indicated. The bottom row indicates the difference of the estimated $G_{z,s}$ value from the model against the other predicted $G_{z,s}$-maps for the brain region. The values are shown in μT/m, and the arrows indicate features of interest in the images.

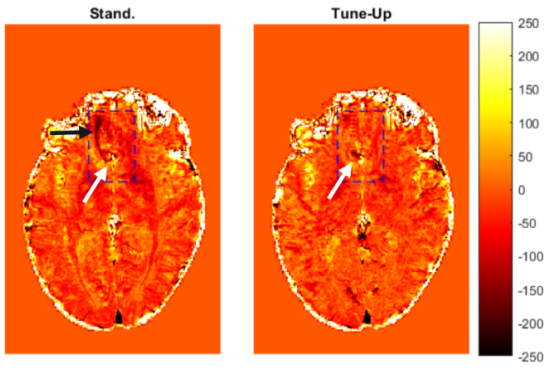

Figure 4.15: The difference in estimated $G_{z,s}$ values obtained from the linear fit of the field map datasets against the value obtained from the non-linear least-squares fitting to ME-GRE datasets, evaluated between the datasets with corresponding shim mode (Stand. or tune-up). The values of $G_{z,s}$ are shown in units $\mu T/m$.

A better correspondence is observed between the $G_{z,s}$-maps obtained from the experimental meas-

urements, where the difference images taken between the $G_{z,s}$-maps from the experimental measurements with equivalent shim mode are shown in Fig. 4.15. Only minor differences are observed within the ROI where the $G_{z,s}$-map from the ME-GRE dataset with tune-up shim mode seems to overestimate the $G_{z,s}$ in a small region above the nasal cavity and ethmoid sinuses (see black arrow Fig. 4.15). In addition, more noticeable variations are observed within the ROI indicated by the white arrows but occur only over a small region. Some variations following patterns similar to tissue structures are also observed for the brain region in the difference images indicated in Fig. 4.15.

The above observations are further highlighted in Table 4.7 indicating the RMSE value for the different comparisons made. Generally, higher RMSE values are observed when evaluated over the entire brain region, most likely due to the presence of the observed noise-like pattern at the edges of the masked brain region. However, the comparisons between the model and the ME-GRE datasets show noticeably lower RMSE values evaluated over the brain region compared to the other comparisons. The lowest RMSE values, assessed over the ROI, are observed for comparisons between the $G_{z,s}$-maps attained from the experimentally measured datasets. However, only slightly higher RMSE values are seen for the other comparisons except for the comparison between the model and the ME-GRE dataset with tune-up shim mode.

Table 4.7: The RMSE values for the models' prediction of $G_{z,s}$ against the $G_{z,s}$-maps obtained from the field map and ME-GRE datasets (both stand. and tune-up), in addition to the RMSE values for the comparison of the field map against ME-GRE datasets with corresponding shim mode. The RMSE value is evaluated over the entire brain region within the investigated image slice and a defined ROI.

Datasets	**RMSE Brain [μT/m]**	**RMSE ROI [μT/m]**
Model - FM stand.	267	94
Model - FM Tune-Up	286	91
Model - ME-GRE stand.	104	123
Model - ME-GRE Tune-Up	120	93
FM - ME-GRE (stand.)	223	70
FM - ME-GRE (Tune-Up)	235	51

Histogram plots indicating the fraction of voxels within the ROI with a given difference in estimated $G_{z,s}$ for each comparison made are indicated in Fig. 4.16. In general, the histogram plots for the comparisons made against the model indicates that the model underestimates the value of $G_{z,s}$ for most of the voxels within the ROI, except for the comparison against the field map with tune-up shim mode, where the model seems to overestimate for almost 50% of the voxels in the ROI. In addition, a more uniform distribution of the histogram plot is observed for the comparison of the model against the field map with tune-up shim mode. Nearly 56%, 55%, 41%, and 61% of the voxels show a difference in estimated $G_{z,s}$ of ± 50 μT/m when comparing the model against field map standard shim, field map tune-up, ME-GRE standard shim, and ME-GRE tune-up, respectively. In addition, for the same comparisons, 21%, 18%, 13% and 19% of the voxels have estimated equal values of $G_{z,s}$. Furthermore, it is also observed that the comparisons made against the model generally show bars extending to larger values than what is observed for the comparison made between the experimentally measured datasets.

The histogram plots attained for the comparisons of the field maps against the ME-GRE with equal shim mode show a far more peaked distribution than the other indicated plots, where 76% and 93% of the voxels have a difference of ± 50 μT/m for the comparisons made between the datasets with standard and tune-up shim mode, respectively. Most of the observed offset values for the presented comparisons are negative. 29% and 44% of the voxels in the ROI show a difference of estimated $G_{z,s}$ equal to zero for the comparisons made against the experimental datasets with standard and tune-up shim mode, respectively, and the distribution of the histogram plots for the

presented comparison show a peak value correspondingly at -50 μT/m and 0 μT/m.

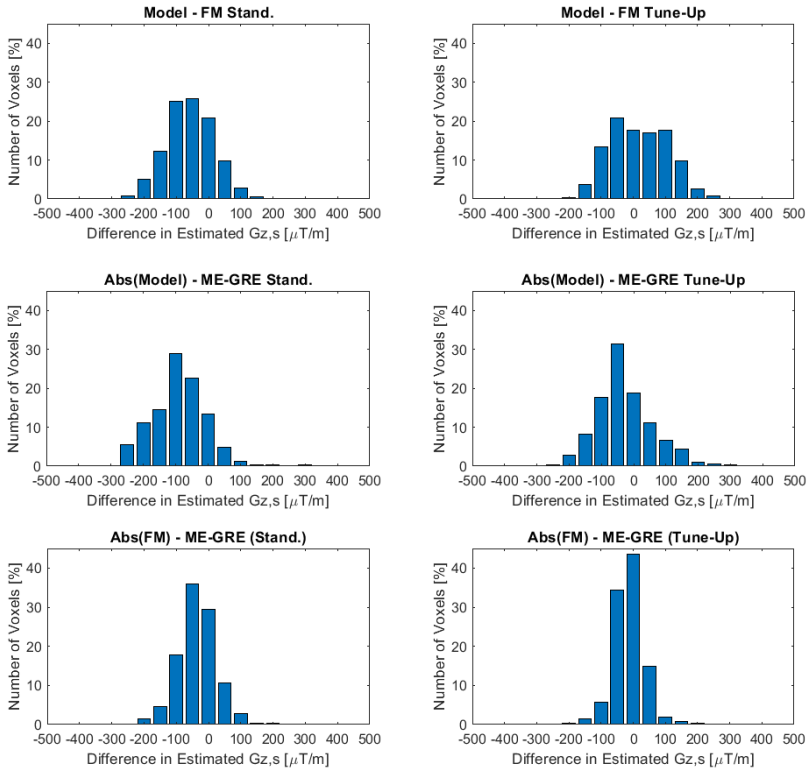

Figure 4.16: Histogram plots indicating the number of voxels within the ROI with a given difference in estimated $G_{z,s}$ for each comparison made. The number of voxels is given in percentage of the total number of voxels within the ROI.

Chapter 5

Discussion

5.1 Quantification of Frequency Offset

A Fourier-based method for calculating frequency offset from susceptibility maps has been described and tested on in vivo experimental datasets. A remarkable degree of resemblance was observed between the numerical calculations and experimentally measured field maps. Several features observed in the experimental field maps were reproduced by the numerical model, especially in the regions above the nasal cavity, and the sphenoid and ethmoid sinuses. The numerical model was able to replicate both the shape, extent and order of magnitude of the induced frequency offset in the affected area. In addition, the numerical model reproduced the same pattern of frequency offsets at the back of the head (the posterior side), as observed for the measured field map with tune-up shim mode. The induced frequency offset value in the mentioned area indicates how the shape of the head is close to, but not perfectly spherical, and will induce slight frequency offsets due to its interface to the surrounding air. However, apparent differences between the numerical model and measured field maps were also seen to occur, affecting the accuracy of the model. Most noticeable was the difference in frequency offset above the temporal bone and the tympanic cavity, where the experimental data indicated significant frequency offsets, whereas no similar pattern was seen in corresponding regions for the numerical simulations.

Higher quality air segmentation was achieved by using UTE images. However, limitations were still found for the segmentation of air cavities within the temporal bone and tympanic cavities. The poor bone-air contrast in the mentioned areas was mainly caused by the intensity modulation artifact observed in the acquired images, which was most pronounced towards the inferior parts of the imaging volume. Thus, the observed artifact caused significant limitations for the air segmentation in the affected areas. The observed intensity modulation is most likely due to B_1 inhomogeneity, a well-known disadvantage of acquiring images at higher field strength, where an uneven excitation of nuclei within the imaging volume occurs, giving rise to shading areas. In addition, slightly higher frequency offsets were measured from the field maps in the locations above the nasal cavity and ethmoid sinuses, compared to the predicted values from the numerical model, which is most likely also a consequence of the poor air segmentation in the area. The partly lost air segmentation in the nasal cavity and ethmoid sinuses, was mainly limited by the spatial resolution used to segment air cavities manually. The many small air cavities with highly uneven surfaces were challenging to mask out with the resolution of 0.75 mm. Thus, the difficulty in attaining anatomically correct and detailed air segmentation is a limitation of the model, and a source of error for the calculated frequency offset. This underlines how the validity of the numerical model is heavily dependent on having anatomically correct segmentation of the different tissues present, where the shape, orientation, and susceptibility difference between the bulk tissues, largely affect the simulated frequency offsets.

An improved air segmentation may be achieved by applying a dual-echo UTE imaging sequence. Applying a dual echoed UTE sequence could improve the accomplished differentiation between bone and air in the acquired image, as tissues with high T_2 values are suppressed, making the

tissues with shorter T_2^* values more visible. In addition, interpolation of the anatomical images to higher spatial resolution can be performed to increase the accuracy of the manual segmentation performed on the UTE images, where more complex interfaces and smaller air cavities can now be more easily masked as air. A higher spatial resolution of the susceptibility map will also improve the numerical model results at the interfaces between tissue compartments, as it effectively reduces the discretization effects in the numerical model. Another possible approach to attain more accurate segmentation of air and bone is to utilize a deep learning-based image-to-image translation network (Ladefoged et al. 2020).

Larger field offsets and stronger local field gradients were observed in the regions adjacent to the sinuses and nasal cavities in the standard field map compared to both the tune-up field map and the model. To understand this observation, one can note that the local susceptibility-induced field gradients above the sinuses and the nasal cavities oppose the long-range gradient in the inferior-superior direction in the tune-up field map. The subject-specific shimming compensates well for the long-range gradient but will consequently exacerbate the local field gradient above the sinuses and the nasal cavities in the standard field map due to the limitation of spherical harmonic shimming which cannot compensate for the local complex field distortions. Thus, a larger error is observed within the ROI located above the nasal cavities when the model is compared to the standard field map.

A higher degree of agreement between the numerical model and the tune-up field map is expected throughout the brain region as the numerical model does not include the effect of subject-specific shimming. However, when evaluating the RMSE value over the entire brain region within the imaging volume, a slightly higher RMSE value was attained for the comparison against the tune-up field map than when compared to the field map with standard shim mode (Table 4.2). From the analysis of the RMSE values calculated for each transverse image slice, a clear U-shape distribution with significant RMSE values towards the ends of the brain region in the inferior-superior direction was observed. By visual comparison between the tune-up field map (Fig. 4.5) and the results of the numerical model (Fig. 4.6) presented in the sagittal image plane, an apparent discrepancy is observed along the inferior-superior direction of the imaging volume, where the presence of the long-range field gradient is not as recognizable in the results of the numerical model as it is for the tune-up field map. Only slight tendencies of its presence are visible in the numerical model at the inferior and superior ends of the brain region. Thus, the noticeably high RMSE values observed at the inferior and superior ends of the brain region primarily result from the absence of the long-range field gradient in the calculated frequency offset.

A head coil was used for all measurements performed in this thesis. Anatomical structures down to the shoulder region could therefore not be imaged. In addition, a strong intensity modulation artifact was observed in the measured anatomical images and was most prevalent at the more inferior parts of the imaging volume. Thus, only parts of the neck and jaw were able to be segmented, and the numerical model greatly lacked accurate information about the susceptibility distribution in the shoulder, neck, and jaw regions. The presence of the substantial interface between the external surface of the body and the surrounding air has previously been reported to induce a global offset value of the field within the brain, and the inclusion of the jaw and neck to be of importance for the presence of a field gradient across the brain in the inferior-superior direction (Koch et al. 2006). Thus, the lack of segmentation of more inferior body parts, from the jaw and down to the shoulder region, was shown to be a considerable limitation in the accuracy of the numerical model, especially at the inferior and superior ends of the brain region. A drastic improvement is expected in the agreement between the measured tune-up field map and computed frequency offset if information about the inclusions and anatomical structures of the shoulder, neck, and jaw region is included in the subject-specific susceptibility model. An increased segmentation of the mentioned body parts can be achieved by utilizing a cross-modality registration between a reference image, not specific to the subject, and the acquired image for the subject (Koch et al. 2006).

The RMSE values for the comparison against the tune-up field map evaluated over four regions divided in the inferior-superior direction, clearly showed higher errors of the model in the lower and upper brain regions, corresponding to the areas where the long-range field gradient induced significant frequency offsets. However, relatively low RMSE values were observed for the two ROIs

located in the areas with local susceptibility-induced field gradients present. Thus, even though the results of the numerical model lacked the prediction of an increasing long-range field gradient in the inferior-superior direction, high accuracy was still observed for the model's estimation of frequency offset in the two ROIs located in proximity to the nasal cavity, sphenoid and ethmoid sinuses. Thus, the model showed high accuracy in areas where more complex field distortions are generated, which are the areas of primary interest in this thesis, as today's shimming technique has problems in correcting for these field distortions. The frequency offset values generated by the long-ranged gradient were less substantial and more equal to the one estimated by the numerical model in this area, most likely being the reason for the observed higher accuracy in the ROIs.

However, even with the improvements of the subject-specific susceptibility model, some deviations between the measured field maps and the numerical model are still expected to be observed, mainly due to other sources of B_0 inhomogeneity not taken into account in the numerical model. The measured field maps include external magnetic field perturbations (e.g., due to main magnet imperfections), susceptibility-induced field distortions generated from less substantial interfaces, and dynamic B_0 field inhomogeneity. The measured field maps include the slight field distortions caused by the susceptibility interfaces between, e.g., grey matter, white matter, and CSF. These tissues were, for simplification, all set to the susceptibility value of soft tissue in the numerical model, as they have nearly identical susceptibility properties. In addition, the dynamic B_0 inhomogeneity induced by displacement of structures with different magnetic susceptibilities, was not taken into account in the numerical model, but is present in the measured field maps. The respiration cycle has been proven to cause a time-varying field distortion that can extend into the brain region due to changes in the spatial position of several large structures surrounding the lungs, in addition to changes in air density within the lungs (change in its effective susceptibility value) (Marques and Bowtell 2005; Raj et al. 2000; Van de Moortele et al. 2002). Furthermore, the effect of rotations during imaging can also cause deviations between the calculated and measured field inhomogeneity (Marques and Bowtell 2005). For the numerical model, the main magnetic field is applied in the inferior-superior direction, and no rotational effects of the imaging volume between the acquisition of the anatomical MP-RAGE image and the acquisition of the reference field map are taken into account. However, the effect of rotation can easily be incorporated into the simulation in future work by rotating the direction of the main magnetic field in the numerical model. A rotation of the main magnetic field can be introduced when calculating the susceptibility-induced field distortion in k-space by using the expression

$$D_z(\vec{k}) = \frac{1}{3} - \frac{(k_z cos\theta - k_y sin\theta)^2}{k_x^2 + k_y^2 + k_z^2}$$

for the dipole field, where the angle θ corresponds to rotation of the coordinate system (a clockwise rotation about the x-axis) (Marques and Bowtell 2005).

Another essential feature of the numerical model that may affect its accuracy is its dependency on the value of susceptibility. As previously emphasized, results from the numerical model are largely influenced by the susceptibility values given to the various bulk tissues. Thus, a possible reason for the variation observed in the calculated frequency offset from the measured field maps can also be due to the values assigned to the tissues in the model. The magnetic susceptibility values depend not only on the intrinsic composition of the tissue, but also on the temperature and other physiological variables (Collins et al. 2002). These values are not often measured, and uncertainties exist in the choice of susceptibility values. The values used are taken from J.F. Schenck 1996. However, the values used in a later published article written by Koch et al. 2006 use a slightly different value of susceptibility of soft tissue but a more noticeably different value for bone. In addition, the application of the filter in k-space to avoid truncation artifacts and minimize the discretization effect in the results has been proven in a previous paper published by Schäfer et al. 2009 to affect the results of the frequency offset as it attenuates regions of the dipole field. However, the filter kernel was shown to have the most prominent effects on the contrast between grey and white matter, which is not considered in the susceptibility model used in this thesis.

5.2 Quantification of Through-slice Susceptibility-induced Gradients

Through-slice susceptibility gradients were quantified from non-linear least-squares fitting of experimental data to a sinc-corrected signal decay function and linear fitting of both the measured and computed field inhomogeneity across a distance of 4.5 mm (equal to the slice thickness used in the ME-GRE scan). From the results indicated in Table 4.4 and Fig. 4.11, highly accurate non-linear least-squares fitting of the monoexponential signal decay function was achieved in the narrow region, which supported the assumption that the field is homogeneous in that area. In addition, the mean T_2^* value was found to be between the value of grey and white matter when compared to the values found in Peters et al. 2007, with only a slight elevation from the one given for white matter. However, variations in estimated T_2^* values were observed within the narrow region. Possible reasons for the observed variation of estimated T_2^* values include partial volume effect, presence of weak susceptibility gradients due to tissue interfaces between grey and white matter, or due to the direction of the nerve fibers present in white matter. Relatively large slice thickness was used in the ME-GRE sequence to ensure that the through-slice field gradients are the dominant contributor to signal modulation compared to in-plane susceptibility gradients. However, having a larger slice thickness increases the partial volume effect where different tissues are averaged together in a slice, resulting in erroneous signal intensity. From inspection of the intensity image for the narrow region, the grey matter seems to be present in small parts of the region. Thus, a weak susceptibility interface between the two tissues is most likely present and alters the measured signal in the affected regions. Interfaces between grey and white matter in neighboring slices can also induce weak gradients affecting the illustrated image slice. In addition, the narrow region was chosen in an area mainly including white matter, which consists of numerous nerve fibers directed along a tract. The T_2^* value has shown to be dependent on the orientation of these white matter fibers and can therefore also be a reason for the observed variations in estimated T_2^* values.

The model fit to the sinc-corrected signal decay function was observed to describe the evolution of the experimentally measured data noticeably well, especially within the ROI. In addition, the acquired $G_{z,s}$-maps from the model fit followed the same trends as observed for the field maps, where larger and stronger local field gradients were quantified for the standard ME-GRE dataset. However, significantly worse goodness-of-fit statistics at specific regions of the brain and tissue contrast in the calculated $G_{z,s}$-maps were observed when evaluating the model fit over the entire brain region. The observations indicate an important limitation of the model fit, namely that the whole brain region was given the same value of T_2^*, despite the presence of heterogeneous tissue distribution. Thus, the tissues with different T_2^* than what was assumed by the model will not be appropriately described by the model fit and give an incorrect estimation of the $G_{z,s}$ values. This was especially observed for locations in CSF as it has an appreciably lower T_2^* value than what was assumed by the model fit. The minor difference in the T_2^* value for grey and white matter to the one assumed by the model fit gives relatively high goodness-of-fit statistics, but slight deviations in estimated $G_{z,s}$ values, and are most likely the reason for the observed tissue contrast in the $G_{z,s}$-maps.

Even though the anatomical pattern observed in the results from the sinc-corrected model fit is most likely an erroneous feature, it is important to keep in mind that some susceptibility-induced gradients are expected between grey and white matter. The presence of underlying/overlying anatomy can affect the superior/inferior image slices. Thus, some anatomical features may appear projected into the neighbor slice. However, these patterns would have followed more or less the pattern of the interfaces between the structures and not an elevated value throughout the tissue types. A mixture of both susceptibility-induced field gradients due to the tissue interfaces and the erroneous anatomical feature may be present in the results but is difficult to differentiate in the obtained $G_{z,s}$ map.

When comparing the quantified $G_{z,s}$ map calculated from the numerical model with the maps obtained from the field map and the ME-GRE datasets, a striking degree of similarity in pattern, extent, and order of magnitude is evident in the ROI located above the nasal cavity, ethmoid and sphenoid sinuses (see Fig. 4.14). In addition, the absolute value of the model is able to

resemble the slightly lower value of $G_{z,s}$ surrounding the area of strong gradients. This was also observed for the $G_{z,s}$-map obtained from the tune-up ME-GRE dataset. From further analysis of the maps indicating the difference between the model and the experimental measurements (bottom row Fig. 4.14), regions of noticeable difference were observed within the ROI, and a higher degree of heterogeneity was seen throughout most parts of the brain region. As previously discussed, the experimental data is a direct measurement of the subject and will be affected by other factors than only the susceptibility differences, e.g., external field inhomogeneity and dynamic field inhomogeneity. It will also include a higher degree of anatomical information about the local tissue variation with different intrinsic T_2^* values, explaining the larger degree of heterogeneous distribution of $G_{z,s}$ values seen for the maps calculated from the experimental datasets. Thus, many of the observed deviations result from the numerical model being a simplified version of reality, whereas the experimental data directly measures the total system.

In addition, as previously discussed, the limitations of the numerical model exist in the ROI above the ethmoid and nasal cavity due to poor air segmentation and are observed as a negative deviation when compared to the $G_{z,s}$ maps calculated from the experimental data in Fig. 4.14. The deviation is larger when the model is compared to the experimental data with standard shim mode, corresponding to the previous finding where the local susceptibility gradient is increased for the datasets where subject-specific shimming has been applied. Furthermore, the missing long-range gradient for the numerical model is also affecting the resemblance of its $G_{z,s}$ map with the ones attained from the experimental datasets with tune-up shim mode, where a relatively strong overestimation of the $G_{z,s}$ was observed for the numerical model throughout the brain region, except the part above the ethmoid and nasal cavities.

A noticeably higher degree of similarity between the $G_{z,s}$-maps calculated from the field map and the ME-GRE datasets were observed, where the primary amount of voxels within the ROIs show either relatively low or no deviations in the comparison against the experimental data. This shows how the model used to fit the signal decay to the ME-GRE data is a reasonable model, even though it has made assumptions simplifying the reality, e.g., field linearity across the slice thickness and ideal slice profiles.

Chapter 6

Future Work

The results suggest that the largest improvement in the model's accuracy could be obtained by improving the segmentation. Thus, improving the segmentation step in the established pipeline should be investigated in future work. Possibilities of improving the segmentation step include applying dual-echo UTE imaging and interpolating the anatomical MP-RAGE image to obtain a higher resolution for the manual segmentation. Furthermore, a deep learning algorithm for differentiation between the localization of bone and air can also be utilized. In addition, cross-modality registration between reference images, not specific to the subject, and the subject-specific anatomical images can be used to improve the segmentation of the inclusions in the jaw, neck, and shoulder area. It is also expected to be beneficial to gain further insight into the effect of rotation on the accuracy of the numerical model against the acquired field maps and the cost of applying the low-pass filter in k-space to see if the filter affects the quantity of calculated frequency offset.

Generally, high accuracy of the numerical model was achieved in the regions of interest, with the greatest resemblance to the tune-up field map, and it was proven to be a valid method for simulating frequency offset. Thus, the method can be further extended by including the effect of shimming and comparing the results to the field maps with standard shim mode. For this thesis, the calculated frequency offset was used to quantify the presence of through-slice field gradients, whose presence induced signal loss. However, the results of the numerical model can also, in principle, be used to predict geometric distortions for EPI sequences, which are sensitive to susceptibility effects.

B_0 field inhomogeneity is a major limitation of the theoretical gain in spinal cord imaging at higher field strength, due to the highly variable field gradients induced around each vertebra in the spine. Applying the numerical method and testing its validity in spinal cord imaging is also of interest, as gaining further insight into the susceptibility-induced field gradient can help improve the shimming technique for the mentioned area. However, discretization effects will most likely be increased due to the highly variable anatomical structures. Future work should also focus on improving the spatial resolution and thus the discretization effect of the numerical model when going into spinal cord imaging.

Chapter 7

Conclusion

This work established a pipeline for calculating the subject-specific B_0 field inhomogeneity based on anatomical images. The results of the numerical model were validated by comparing them to experimentally measured field maps. In addition, through-slice susceptibility-induced field gradients were quantified from the experimentally measured field maps and the simulated field offset. A non-linear least-squares model fit of the experimental dataset from a ME-GRE scan to a corrected signal decay function was also performed to quantify the presence of $G_{z,s}$.

The numerical model showed promising results when compared to experimental measurements, where the numerical model reproduced many of the same features observed in the experimental data. This was especially seen within the brain region with the highest susceptibility-induced field distortions, e.g., above the nasal cavities, ethmoid and sphenoid sinuses. The model showed the highest degree of similarity to the tune-up field map in the regions above the mentioned air cavities. Similar analyses were made for the obtained maps indicating the quantified $G_{z,s}$ values. However, some issues affecting the validity of the model remained. The largest discrepancies from the experimental data were observed at the inferior and superior ends of the brain region. The accuracy of the segmentation is currently the main limiting factor, but several steps can be taken to improve this in the future.

An accurate subject-specific B_0 field inhomogeneity achieved using the numerical model has the potential to provide helpful information in work to minimize susceptibility artifacts through shimming or sequence optimization. The work performed in this thesis lays a solid foundation for future studies where improvements and further model development can be made, such that further insight into how shimming and sequence optimization affects susceptibility-induced field distortion can be obtained.

Bibliography

Ashburner, J. et al. (2021). 'SPM12 Manual'. In.

Bernstein, M.A., J. Huston III and H.A. Ward (2006). 'Imaging Artifacts at 3.0T'. In: *Journal of magnetic resonance imaging* 24.4, pp. 735–746.

Boveris, A. (1998). 'Biochemistry of free radicals: from electron to tissue'. In: *Medicine (Buenos Aires)* 58, pp. 350–356.

Brainder, ed. (n.d.). *The NIFTI file format*. https://brainder.org/2012/09/23/the-nifti-file-format/. Accessed: 2022-04-26.

Brown, R.W. et al. (1999). *Magnetic Resonance Imaging: Physical Principles and Sequence Design*. John Wiley and Sons, Inc.

Chang, E.Y., D. Jiang and C.B. Chung (2015). 'UTE imaging in the musculoskeletal system'. In: *JOURNAL OF MAGNETIC RESONANCE IMAGING* 41.4, pp. 870–833.

Cheng, Y.N., J. Neelavalli and E.M Haacke (2009). 'Limitations of calculating field distributions and magnetic susceptibilities in MRI using a Fourier based method'. In: *Phys. Med. Biol* 54, pp. 1169–1189.

Collins, C.M. et al. (2002). 'Numerical calculations of the static magnetic field in three-dimensional multi-tissue models of the human head'. In: *Magnetic Resonance Imaging* 20, pp. 413–424.

Czervionke, L.F. et al. (1988). 'Magnetic susceptibility artifacts in gradient-recalled echo MR imaging'. In: *American Journal of Neuroradiology* 9, pp. 1149–1155.

Dahnke, H. and T. Schaeffter (2005). 'Limits of Detection of SPIO at 3.0 T Using T_2^* Relaxometry'. In: *Magnetic Resonance in Medicine* 53.

Dance, D. R. et al. (2014). *Diagnostic radiology physics: A handbook for teachers and students. Endorsed by: American Association of Physicists in Medicine, Asia-Oceania Federation of Organizations for Medical Physics, European Federation of Organisations for Medical Physics*.

Deichmann, R., J.A. Gottfried et al. (2003). 'Optimized EPI for fMRI studies of the orbitofrontal cortex'. In: *NeuroImage* 19.2, pp. 430–441.

Deichmann, R., O. Josephs et al. (2002). 'Compensation of Susceptibility-Induced BOLD Sensitivity Losses in Echo-Planar fMRI Imaging'. In: *NeuroImage* 15, pp. 120–135.

Deville, G., M. Bernier and J. M. Delrieux (1979). 'NMR multiple echoes observed in solid ^{3}He'. In: *Phys. Rev. B* 19 (11), pp. 5666–5688. DOI: 10.1103/PhysRevB.19.5666. URL: https://link.aps.org/doi/10.1103/PhysRevB.19.5666.

Duyn, J.H. (2018). 'Studying brain microstructure with magnetic susceptibility contrast at high-field'. In: *NeuroImage* 168, pp. 152–161.

Duyn, J.H. and J. Schenck (2016). 'Contributions to magnetic susceptibility of brain tissue'. In: *NMR in Biomedicine* 30.4, e3546.

Elster, A.D and J. Burdette (2001a). *Gyromagnetic ratio (γ)*. URL: https://mriquestions.com/gyromagnetic-ratio-gamma.html (visited on 5th Nov. 2021).

— (2001b). *Susceptibility Artifact*. URL: https://mriquestions.com/susceptibility-artifact.html (visited on 21st Oct. 2021).

Elster, A.D. and J.H. Burdette (2001). *Questions and answers in magnetic resonance imaging*. 2nd. Mosby.

Fernández-Seara, M.A. and F.W. Wehrli (2000). 'Postprocessing Technique to Correct for Background Gradients in Image-Based R_2^* Measurements'. In: *Magnetic Resonance in Medicine* 44.

Gentile, K. (2002). 'The care and feeding of digital, pulse-shaping filters'. In: *RF Design*.

Griffiths, D.J. (1999). *Introduction to electrodynamics*. Upper Saddle River.

Grøvik, E. (2017). 'Multimodal Dynamic MRI for Structural and Functional Assessment of Cancer'. PhD thesis. University of Oslo.
Hagberg, G.E. et al. (2002). 'Real-time quantification of T changes using multiecho planar imaging and numerical methods'. In: *Magnetic Resonance in Medicine* 48.5, pp. 877–882.
Huang, S.Y. et al. (2015). 'Body MR imaging: Artifacts, k-space, and solutions'. In: *Radiographs* 35, pp. 1439–1460.
Jackson, W.D. (1999). *Classical electrodynamics*. 3rd. John Wiley and Sons, Inc.
Juchem, C. et al. (2011). 'Dynamic multi-coil shimming of the human brain at 7T'. In: *Journal of Magnetic Resonance* 212, pp. 280–288.
Koch, K.M. et al. (2006). 'Rapid calculations of susceptibility-induced magnetostatic field perturbations for in vivo magnetic resonance'. In: *Phys. Med. Biol* 51, pp. 6381–6402.
Ladefoged, C.N. et al. (2020). 'AI-driven attenuation correction for brain PET/MRI: Clinical evaluation of a dementia cohort and importance of the training group size'. In: *NeuroImage* 222.
Liang, Z. and P.C. Lauterbur (2000). *Principles of Magnetic Resonance Imaging: A Signal Processing Perspective*. IEEE Press Series in Biomedical Engineering Metin Akay.
Marques, J.P. and R. Bowtell (2005). 'Application of a Fourier-Based Method for Rapid Calculation of Field Inhomogeneity Due to Spatial Variation of Magnetic Susceptibility'. In: *Concepts in Magnetic Resonance Part B (Magnetic Resonance Engineering)* 25B, pp. 65–78.
McRobbie, D.W. et al. (2017). *MRI from Picture to Proton*. 3rd. Presidio Press.
Mulay, L.N. (1963). *Magnetic Susceptibility*. Interscience.
Murashima, M., T. Ueno and N. Sugimoto (2013). 'Effective digitized spatial size of unit dipole field in Quantitative Susceptibility Mapping'. In: pp. 1049–1052. DOI: 10.1109/EMBC.2013.6609684.
Ogawa, S., T.M. Lee and D.W. Tank (1990). 'Brain magnetic resonance imaging with contrast dependent on blood oxygenation'. In: *National Acad Sciences* 87, pp. 9868–9872.
Ojemann, J.G. et al. (1997). 'Anatomic Localization and Quantitative Analysis of Gradient Refocused Echo-Planar fMRI Susceptibility Artifacts'. In: *NeuroImage* 6.3, pp. 156–167.
Pauly, J.M. et al. (1989). 'Slice-selective excitation for very short T2 species'. In: *Proc 8th Annual Meeting ISMRM, Amsterdam*.
Peters, A.M. et al. (2007). 'T_2^* measurements in human brain at 1.5, 3 and 7 T'. In: *Magnetic Resonance in Medicine* 25.
Port, J.D. and M.G. Pomper (2000). 'Quantification and Minimization of Magnetic Susceptibility Artifacts on GRE Images'. In: *Journal of Computer Assisted Tomography* 24, pp. 958–964.
Raj, D. et al. (2000). 'A model for susceptibility artefacts from respiration in functional echo-planar magnetic resonance imaging'. In: *Physics in Medicine and Biology* 45.
Reichenbach, J.R. et al. (1997). 'Theory and application of static field inhomogeneity effects in gradient-echo imaging'. In: *Journal of Magnetic Resonance Imaging* 7.
Robson, M.D. et al. (2004). 'Contrast enhancement of short T2 tissues using ultrashort TE (UTE) pulse sequences'. In: *Clinical Radiology* 59.8, pp. 720–726.
Salomir, R., B. Denis de Senneville and C.TW. Moonen (2003). 'A Fast Calculation Method for Magnetic Field Inhomogeneity due to an Arbitrary Distribution of Bulk Susceptibility'. In: *Concepts in Magnetic Resonance Part B: Magnetic Resonance Engineering* 19B, pp. 26–34.
Schäfer, A. et al. (2009). 'Using magnetic field simulation to study susceptibility-related phase contrast in gradient echo MRI'. In: *NeuroImage* 48, pp. 126–137.
Schenck, J.F. (1996). 'The role of magnetic susceptibility in magnetic resonance imaging: MRI magnetic compatibility of the first and second kinds'. In: *Medical Physics* 23, pp. 815–850.
Schmidt, A. (2021). 'Modeling of the Susceptibility-induced Magnetic Field Distortion by Using a Fourier-based Method at 7 Tesla'. PhD thesis. Norwegian University of Science and Technology.
Sommer, S. (2022). *Siemens Healthineers*. personal communication.
Stockmann, J.P. et al. (2016). 'A 32-Channel Combined RF and B0 Shim Array for 3T Brain Imaging'. In: *Journal of Magnetic Resonance* 75, pp. 441–451.
Trungo, T. et al. (2002). 'Three-dimensional numerical simulations of susceptibility-induced magnetic field inhomogeneities in the human head'. In: *Magnetic Resonance Imaging* 20.
Van de Moortele, P.F. et al. (2002). 'Respiration-induced B0 fluctuations and their spatial distribution in the human brain at 7 Tesla'. In: *Magnetic Resonance in Medicine* 47, pp. 888–895.
Wachowicz, K. (2014). 'Evaluation of active and passive shimming in magnetic resonance imaging'. In: *Research and Reports in Nuclear Medicine* 4, pp. 1–12.

Wang, Y. and T. Liu (2015). 'Quantitative Susceptibility Mapping (QSM): DecodingMRI Data for a Tissue Magnetic Biomarker'. In: *Magnetic Resonance in Medicine* 73.

Wang, Y., D. Zhou and P. Spincemaille (2015). 'What is the Lorentz sphere correction for the MRI measured field generated by tissue magnetic susceptibility: the spatial exclusivity of source and observer and the Cauchy principal value'. In: *Proceedings of the International Society for Magnetic Resonance in Medicine* 23.

Weishaupt, D., V.D. Kochli and B. Marincek (2008). *How does MRI work?: An Introduction to the Physics and Function of Magnetic Resonance Imaging*. 2nd. Springer.

Weiskopf, N. et al. (2004). 'Single-shot compensation of image distortions and BOLD contrast optimization using multi-echo EPI for real-time fMRI'. In: *NeuroImage* 24, pp. 1068–1079.

Wilson, J.L., M. Jenkinson and P. Jezzard (2002). 'Optimization of Static Field Homogeneity in Human Brain Using Diamagnetic Passive Shims'. In: *Magnetic Resonance in Medicine* 48, pp. 906–914.

Young, H.D and R.A Freedman (2012). *University physics with modern physics*. 13th. Pearson Education.

Appendix

A Main Functions

```
%%Fourier-based method

function [B_kspace] = SusMap_Kspace(Obj,dr)
%Input units:
%[obj] = unitless / susceptibility map
%[dr] = mm
%Output:
% B_z(k)/B_0, dimensionless quantity
[M, N, L] = size(Obj);

Obj_tilde = fftshift(fftn(Obj));
clear Obj

[Dipole_map] = dipole(M,N,L,dr);
clear M N L dr

B_kspace = Obj_tilde.*Dipole_map;
end


function [SusImageSpace] = ImageSpace_SusMap(B_kspace)
%Output: Image domain representation of B_kspace
SusImageSpace = ifftn(ifftshift(B_kspace));
end

function [Dipole]= dipole(M,N,L,dr)
%Input units:
%[dr] = mm
%Output: Dipole field defined in k-space
dx = dr(1)*10^(-3); %units: m
dy = dr(2)*10^(-3);
dz = dr(3)*10^(-3);

dkx = cast((2*pi/(M*dx)),'single'); %units: rad/m
dky = cast((2*pi/(N*dy)),'single');
dkz = cast((2*pi/(L*dz)),'single');
clear dy dx dz dr

kx = ((-M/2)*dkx:dkx:(M/2-1)*dkx);
ky = ((-N/2)*dky:dky:(N/2-1)*dky);
kz = ((-L/2)*dkz:dkz:(L/2-1)*dkz);
clear dky dkx dkz M N L

[kx,ky,kz] = meshgrid(kx,ky,kz);

Dipole = 1/3-(kz.^(2))./(kx.^2 + ky.^2 + kz.^2); %units: unitless
clear kx ky kz krho
Dipole(isnan(Dipole)) = 0;
end

%Filters:

function [Filter,fwhm] = RaisedCosineFilterPolar(beta,Size,dr)
```

```
%Input units:
%[dr] = mm
%Output: Raised Cosine Filter and the FWHM of the filter
M = Size(1);
N = Size(2);
L = Size(3);

dx = dr(1)*10^(-3); %units: m
dy = dr(2)*10^(-3);
dz = dr(3)*10^(-3);

dkx = (2*pi/(M*dx)); %units: rad/m
dky = (2*pi/(N*dy));
dkz = (2*pi/(L*dz));
clear dy dx dz dr Size

kx = ((-M/2)*dkx:dkx:(M/2-1)*dkx);
ky = ((-N/2)*dky:dky:(N/2-1)*dky);
kz = ((-L/2)*dkz:dkz:(L/2-1)*dkz);
clear dkx dky xkz

Ty = 1/(max(ky(M)));
Tx = 1/(max(kx(N)));
Tz = 1/(max(kz(L)));
T = [Ty,Tx,Tz];
T = max(T);
clear Ty Tx Tz

[kx,ky,kz] = meshgrid(kx,ky,kz);
kx = tall(kx);
ky = tall(ky);
kz = tall(kz);
kr = sqrt(ky.^2+kx.^2+kz.^2);
clear kx ky kz

Filter1 = abs(kr)<=(1-beta)/(2*T);
ROI2 = kr>(1-beta)/(2*T) & kr <=(1+beta)/(2*T) ;
ROI2 = Filter1+ROI2;
Filter3 = 0.5*(1+cos(pi*T/beta*(abs(kr)-(1-beta)/(2*T))));
Filter3 = Filter3.*ROI2;
clear ROI2

Filter = Filter1 + Filter3;
Filter(Filter > 1) = 1;
Filter = gather(Filter);

y = squeeze(Filter(:,N/2+1,L/2+1));
halfMax = max(y) / 2;
index1 = find(y >= halfMax, 1, 'first')-1;
index2 = find(y >= halfMax, 1, 'last')+1;
fwhm = index2-index1 + 1;
end


%Zeropadding
function [matrix] = Zeropadding(X,Nnew)
%Input:
%X = original matrix
```

```
%New = New matrix size
%Output: Zeropadded matrix with new size equal to New
[m,n,l] =size(X);

pad_val_y = Nnew(1)-m;
pad_val_x = Nnew(2)-n;
pad_val_z = Nnew(3)-l;

matrix =zeros([Nnew(1) Nnew(2) Nnew(3)],'single');

matrix(pad_val_y/2+1:m+pad_val_y/2,pad_val_x/2+1:n+pad_val_x/2,
pad_val_z/2+1:l+pad_val_z/2) = X(:,:,:);
end

function [matrix] = Padding(X,Nnew,Sus)
%Input:
%X = original matrix
%New = New matrix size
%Sus = susceptibility value given to the padded voxels
%Output: Padded matrix with new size equal to New
[m,n,l] =size(X);
matrix =zeros([Nnew(1) Nnew(2) Nnew(3)],'single')+Sus;
f_pad_y = floor((Nnew(1)-m)/2);
c_pad_y = ceil((Nnew(1)-m)/2);
f_pad_x = floor((Nnew(2)-n)/2);
c_pad_x = ceil((Nnew(2)-n)/2);
f_pad_z = floor((Nnew(3)-l)/2);
c_pad_z = ceil((Nnew(3)-l)/2);

matrix(f_pad_y+1:m+c_pad_y,f_pad_x +1:n+c_pad_x,f_pad_z+1:l+c_pad_z)
= X(:,:,:);
end


%%Simulating GzMaps:

function [t2s, s0,rmse, rsq] = T2sUncorrLM(te, S)
%% Description: Estimating T2*. Monoexponential fit.
%Input
%te = echo train
%S = Acquired data (signal intensity)
te = cast(te*10^(-3),'double'); %units: s

%Range of R2* and T2*
minT2s = min(te)/20;
maxT2s = max(te)*20;
ranget2s = [minT2s, maxT2s];
clear minT2s MaxT2s

%Estimate initial guesses with a fast method:
[s00,r2s0] = InitialEstimate(te, S);


%fit function:
g = fittype('exp1');

%Matrix saving R2s and T2s
r2s = zeros([size(S,1) size(S,2)]);
```

```
t2s = zeros([size(S,1) size(S,2)]);
s0 = zeros([size(S,1) size(S,2)]);
rmse = zeros([size(S,1) size(S,2)]);
rsq = zeros([size(S,1) size(S,2)]);


%fit:
sz = [size(S,1) size(S,2)];
ind = 1:size(S,1)*size(S,2);
[r, c] = ind2sub(sz,ind);

mr = max([size(r,1),size(r,2)]);
for i=1:mr
      x0 = double([s00(r(i),c(i)), r2s0(r(i),c(i))]);
      y = cast(squeeze(S(r(i),c(i),:)),'double');
      %fit:
      [f, gof, op] = fit(te(:), y,g,'StartPoint',x0,'Algorithm',
      'Levenberg-Marquardt');


      %get results:
      r2s(r(i),c(i)) = - f.b;
      t2s(r(i),c(i)) = -1/f.b;

      s0(r(i),c(i)) = f.a;
      rmse(r(i),c(i)) = gof.rmse;
      rsq(r(i),c(i)) = gof.adjrsquare;
end
clear r c sz ind g s00 r2s0

%Set values outside the range to their min or max value of the range:
t2s = SetImgRange(t2s,ranget2s);

%units to ms:
t2s = t2s*10^(3);
end

function [gzuf, rmseuf, rsquf, s0uf] = GzMapRectTot(te, AllS, thmean, ds, Mask)
%% Description: Estimate Gz using sinc-corrected signal decay function
%Input units:
%[ds] = mm
%[thmean] = ms
%[te] = ms
%Output:
%gzuf = Map of estimated Gz values
%s0uf = Map of estimated S0 values
%rmseuf = Map of RMSE values for the given fits
%rsquf = Map of R^2 values for the given fits


%convert to SI units:
gamma = 42.58*10^(6); %units: Hz/T
te = te*10^(-3); %units: s
thmean = thmean.*10^(-3); %units: s
ds = ds*10^(-3); % units: m

te = cast(te,'double');
```

```
r = Mask(:,1);
c = Mask(:,2);
clear Mask

%Guess a low val:
guessc = 0.01*10^(-6)*gamma*ds;

%allocate matrixes:
rmseuf = zeros([size(AllS,1) size(AllS,2)],'single');
rsquf = zeros([size(AllS,1) size(AllS,2)],'single');
gzuf = zeros([size(AllS,1) size(AllS,2)],'single');
s0uf = zeros([size(AllS,1) size(AllS,2)],'single');

te = te.';

%%Fit functions:
guf = fittype('a.*exp(-x./T).*abs(sin(x.*b./2)./(x.*b./2))','problem',
{'T'},'coefficients',{'a','b'},'independent',{'x'});

lb = double([0 0]); %Lower Bound
maxit = 500;
DiffMaxch = 10^(6);

sr = [size(r,1),size(r,2)];
mr = max(sr);
clear sr

for i=1:mr
   %Initial estimate:
   maxs0 = 1.2*max(AllS(:));
   Num = 0;
   NEm = [size(te,1),size(te,2)];
   NE = max(NEm);
   clear NEm

   for k=1:NE-1
      Num = Num + 2*squeeze(AllS(r(i),c(i),k));
   end
   clear k

   t2s0 = cast(((te(NE)-te(1))/(2*(NE-1))*(squeeze(AllS(r(i),c(i),1))+
   squeeze(AllS(r(i),c(i),NE))+(Num))./(squeeze(AllS(r(i),c(i),1))
   -squeeze(AllS(r(i),c(i),NE))),'single');
   clear NE Num

   s00 = AllS(r(i),c(i),1).*exp(te(1)./(t2s0));
   s00(isnan(s00)) = 0;
   s00(isinf(s00)) = 0;
   s00(s00<0) = 0;
   s00(s00>maxs0) = maxs0;
   clear maxs0 t2s0
   if s00 == 0
      continue
   end

   %fit
   y = cast(squeeze(AllS(r(i),c(i),:)),'double');
```

```
    x0uf = double([s00 guessc]); %unfixed S0
    [fuf, gofuf, opuf] = fit(te(:), y(:),guf,'problem',{thmean},
    'StartPoint',x0uf,'Lower',lb,'MaxIter',maxit,'DiffMaxChange',DiffMaxch)
    ;

    if gofuf.adjrsquare<0
        continue
    end

    %get results:
    gzuf(r(i),c(i)) = fuf.b/(gamma*ds*2*pi); %units: T/m
    s0uf(r(i),c(i)) = fuf.a;
    rmseuf(r(i),c(i)) = gofuf.rmse;
    rsquf(r(i),c(i)) = gofuf.adjrsquare;
end
end


% Intial estimate: Utilizing the expression given in Hageberg:
function [s0, r2s] = InitialEstimate(te, S)
%%Description: Initial guess for s0 and ts* (=1/r2*)
%Parameters:
sizeS = size(S);

% set range of R2* and T2*
minT2s = min(te)/20;
maxT2s = max(te)*20;
rangeT2s = [minT2s, maxT2s];
rangeR2s = [1/maxT2s, 1/minT2s];
clear minT2s maxT2s

maxs0 = 1.2*max(S(:));

Num = zeros([sizeS(1) sizeS(2)]);
NEm = [size(te,1),size(te,2)];
NE = max(NEm);
clear NEm

for k=1:NE-1
    Num(:,:) = Num(:,:) + 2*squeeze(S(:,:,k));
end
clear k

t2s = ((te(NE)-te(1))/(2*(NE-1))*(squeeze(S(:,:,1))+squeeze(S(:,:,NE))+squeeze(Num(:,:)))./
(squeeze(S(:,:,1))-squeeze(S(:,:,NE)));
r2s = 1./t2s;
clear NE Num

s0 = S(:,:,1).*exp(te(1)./(t2s(:,:)));
s0(isnan(s0)) = 0;
s0(isinf(s0)) = 0;

% set range
r2s = SetImgRange(r2s,rangeR2s);
t2s = SetImgRange(t2s,rangeT2s);
s0 = SetImgRange(s0,[0 maxs0]);
end
```

```
%Set images to be values within a defined range
function [res] = SetImgRange(img,range)
   imgMax = range(2);
   imgMin = range(1);
   img(img<imgMin) = imgMin;
   img(img>imgMax) = imgMax;
   img(isinf(img)) = imgMin;
   img(isnan(img)) = imgMin;
   res = img;
end

%Linear fit:

function [Gz,Offset,rmse,rsquare] = GzLinearFit(S,z,Mask)
%%Description: Estimate Gz with linear fit
%%Input units:
%[S] = micro Tesla
%z = [start, end] of slice position, units: mm
[row, col, points] = size(S);
Gz = zeros([row col],'single');
Offset = zeros([row col],'single');
rmse = zeros([row col],'single');
rsquare = zeros([row col],'single');

x = cast(linspace(z(1),z(2),points),'double')*10^(-3); %units: m
r = Mask(:,1);
c = Mask(:,2);
mr = max([size(r,1),size(r,2)]);
yest = zeros([row col],'single');

for i = 1:mr
   y = cast(squeeze(S(r(i),c(i),:)),'double');
   [f,g,g2] = fit(x(:),y(:),'poly1');
   Gz(r(i),c(i)) = f.p1; %units: T/m
   Offset(r(i),c(i)) = f.p2;
   rmse(r(i),c(i)) = g.rmse;
   rsquare(r(i),c(i)) = g.adjrsquare;
   yest(r(i),c(i)) = f.p1.*x(round(points/2))+f.p2;
end

Gz(isnan(Gz)) = 0;
Gz(isinf(Gz)) = 0;

Offset(isnan(Offset)) = 0;
Offset(isinf(Offset)) = 0;

rmse(isnan(rmse)) = 0;
rmse(isinf(rmse)) = 0;

rsquare(isnan(rsquare)) = 0;
rsquare(isinf(rsquare)) = 0;

E = (squeeze(S(:,:,round(points/2))-yest)).^2;
rmseTot = sqrt(mean(E(:)));

end
```

```
%%Other used functions:

function[coords, LR, PA, FH] = ToStandardSpace(Image, afftrans,coordSystem)
% Compute Cartesian coordinates of array of given size
% INPUT:
% nArray    size of array (matrix)
% afftrans  affine transformation matrix [m]; sform
%
% OUTPUT:
% coords    coordinates of the array
%
% Copyright Johanna Vannesjo, FMRIB, Oxford 2015

%LR position left --> right
%PA positions in posterior --> anterior. For given z-coor
%FH position F --> H
%x-dir is phase encoding direction - phasedimension: 1
%y-dir is frequency encoding dir - frequencydimension: 2
%z-dire is slice direction - Spatialdimension: 3

% INFO
% Coords in afftrans matrix, read from nifti-data is defined as:
% L --> R, P --> A, F --> H
% LR = -X, PA = Y, FH = -Z

nArray = size(Image);

if nargin < 3
   coordSystem = 'xyz';
end
if nargin<2 || isempty(afftrans)
   center = floor(nArray/2)+1;
   afftrans = [...
      1 0 0 -center(1); ...
      0 1 0 -center(2); ...
      0 0 1 -center(3)];
end
if length(afftrans) == 3
   center = floor(nArray/2)+1;
   afftrans = [...
      afftrans(1) 0 0 -afftrans(1)*center(1); ...
      0 afftrans(2) 0 -afftrans(2)*center(2); ...
      0 0 afftrans(3) -afftrans(3)*center(3)];
end

vRow = 0:nArray(1)-1;
vCol = 0:nArray(2)-1;
vMat = 0:nArray(3)-1;

[Col,Row,Mat] = meshgrid(vCol,vRow,vMat);
coords = [Row(:) Col(:) Mat(:)];
coords = (afftrans*[coords'; ones(size(Col(:)'))])';

if strcmp(coordSystem,'xyz')
   coords(:,1) = -coords(:,1); %flip x-axis
   coords(:,3) = -coords(:,3); %flip z-axis
end
```

```
% Calculate coordinates in meshgrid style
LR = reshape(coords(:,1),nArray); %Left right
PA = reshape(coords(:,2),nArray); %Posterior Anterior
FH = reshape(coords(:,3),nArray); %Foot head
end


function[slice] = FindSliceStandSpace(slicePos, FH,slicedir)
%%Description: Find correspond slice position in world coordinated between two
↪  subject spaces
[Nr,Nc,Nd] = size(FH);
FHmin = abs(FH - slicePos);
if slicedir == 'dep'
   MeanSlice = mean(FHmin, [1 2]);
elseif slicedir == 'row'
   MeanSlice = mean(FHmin, [2 3]);
elseif slicedir == 'col'
   MeanSlice = mean(FHmin, [1 3]);
end

[slice] = ind2sub(size(MeanSlice),find(MeanSlice == min(MeanSlice(:))));
end

function [y,x,z] = FindZeros(MaskMST,MaskMBone,MaskMAir)
Sus = 1;
[Ny, Nx, Nz] = size(MaskMST);
X = zeros([Ny Nx Nz],'single');
clear Ny Nx Nz

X = FillSus(X,MaskMST,Sus);
X = FillSus(X,MaskMBone,Sus);
X = FillSus(X,MaskMAir,Sus);

[y,x,z] = ind2sub(size(X),find(X ==0));
end

function[X] = FillSus(X,Masked,SusVal)
%%Description: Give voxels in X its susceptibility value for positions given by
↪  the logical mask
X(Masked == 1) = SusVal;
end

function [meanVal] = MeanLim(Matrix,rowlim,collim)
%%Description: Calcuate the mean value of a 2D matrix within defined limits
meanVal = mean2(Matrix(rowlim(1):rowlim(2),collim(1):collim(2)));
end
```

B Experimental Data and Segmentation from Volunteer 1 and 2

Three healthy volunteers were scanned. However, only the results from the last volunteer are presented in the thesis. The anatomical image for the first volunteer obtained from the MP-RAGE sequence, is indicated in the sagittal plane in Fig. 1a. Aliasing effects were observed in the obtained images where the nose is wrongly positioned at the posterior side of the head. The aliasing effect will cause problems in the segmentation step of the tissues, where the nose was segmented as soft tissue at the back of the head (Fig. 1b). Thus, an anatomically wrong susceptibility map was achieved for the given region. In addition, the obtained segmentation of air (the white areas in Fig. 1b) using SPM was insufficient to obtain enough information about the location of the air cavities for the given subject, especially seen for the sphenoid sinus in Fig. 1b. Aliasing effects were also observed in the magnitude image from the field map sequences applied, where the back of the head was wrongly positioned at the anterior side of the human head (Fig. 1c). Thus, the datasets obtained from the measurements applied to the given volunteer were not used.

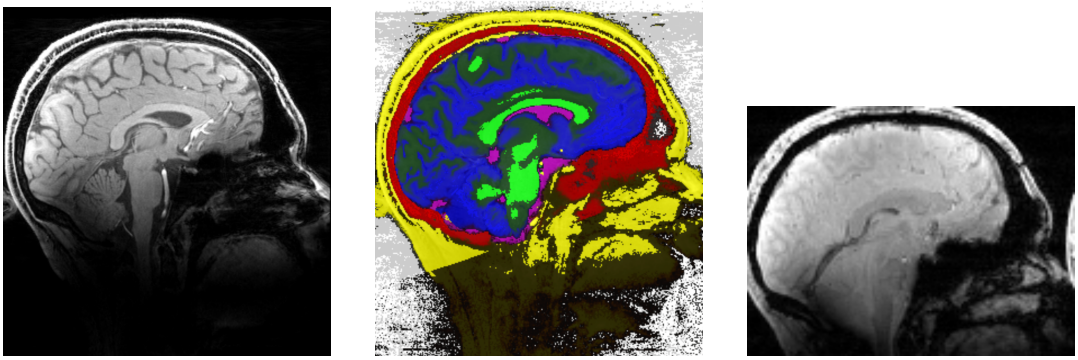

(a) (b) (c)

Figure 1: (a) Sagittal anatomical image obtained from an MP-RAGE sequence and the segmented tissues obtained from SPM12 overlaid on the anatomical MP-RAGE image (b). The blue, green, violet, and red areas represent the segmented location for grey matter, white matter, cerebrospinal fluid, and bone, respectively. (c) Magnitude image in the sagittal plane obtained from a field map sequence.

For the second volunteer, the aliasing of anatomical structures was avoided by changing the placement of the imaging volume and the FOV. In addition, as the SPM12 did not show promising air segmentation, a UTE sequence, which is under development and not in clinical use, was acquired. When comparing the acquired MP-RAGE images with the reconstructed UTE images at similar positions, a geometric distortion of the anatomical structures was observed, where the UTE image seemed to be scaled compared to the MP-RAGE image. Thus, the acquired UTE data could not be used to segment air. The observation was made that the MP-RAGE sequence did not have distortion correction for the spatial gradients turned on, while the UTE sequence did. This may be a part of the reason for the observed geometrical distortion between the anatomical MP-RAGE image and the UTE image. In addition, not all image sequences which were planned got applied due to an unexpected relatively long reconstruction time needed for the UTE images to be constructed.

C Choosing Parameters in the Segmentation Step in SPM12

SPM12 (Statistical Parameter Mapping version 12) is the software tool used to segment the primary tissues in a human brain in this thesis. The goal of the segmentation step was to map air, bone, and soft tissue correctly. In contrast, correct segmentation between grey matter, white matter, and CSF was not of concern due to their relatively identical susceptibility values. The segmentation results were observed to be largely dependent of the input parameters given to the segmentation algorithm.

A significant intensity modulation artifact was prevalent in the anatomical image used as the source channel for the segmentation. The presence of the intensity variation can cause problems for the algorithm to distinguish the intensity variation from being an artifact or due to different tissue classes. Thus, a lower bias regulation should be chosen to tell the algorithm information about the presence of the relatively smooth intensity non-uniformity artifact. In addition, if the intensity modulation is very smooth, a higher FWHM for the gaussian smoothness kernel should be used in the segmentation step.

Fig. 2 indicate the difference in obtained segmentation of bone (Fig. 2a) and air (Fig. 2b) compartments for different parameters settings in the bias correction performed on the image before segmentation. The blue area indicates the obtained segmentation when choosing a medium bias regularisation (0.01) and a full-width-half-maximum (FWHM) of 120 mm for the gaussian bias smoothness filter. The red area indicates the resulting segmentation when choosing very light bias regularisation (0.0001) and a bias FWHM of 60 mm. Choosing low bias regulation and a medium FWHM for the smoothness kernel to account for the intensity modulation artifact gave relatively accurate results in the bone segmentation but close to no air segmentation. Choosing a medium bias regulation and a high bias FWHM gave a noticeably higher amount of air segmentation, especially within the sphenoid sinus. However, a more inaccurate bone segmentation was achieved for these input parameters. A larger part of the brain's frontal area and a relatively large part of the cerebellum were wrongly segmented as bone. Thus, advantages and disadvantages were observed for both results attained using different input parameters.

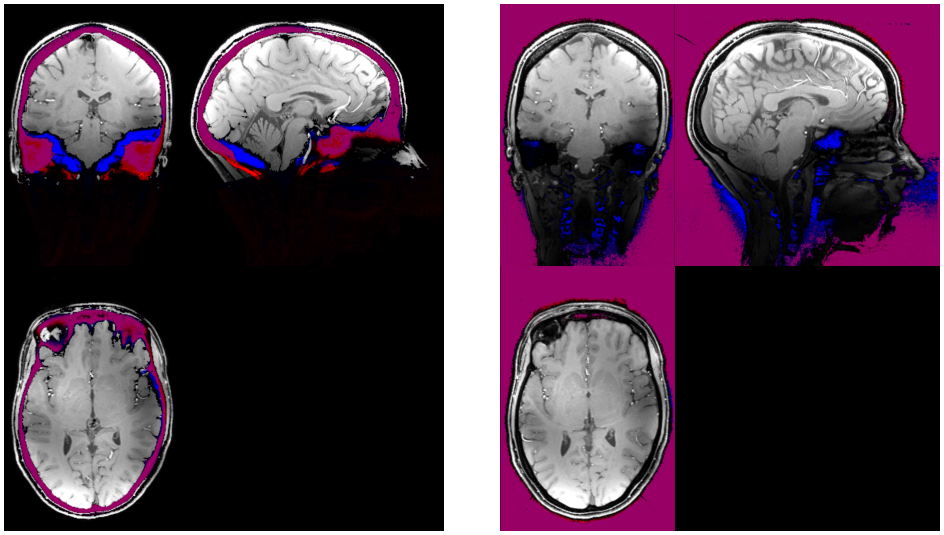

(a) (b)

Figure 2: The resulting segmentation of bone (a) and air(b) from SPM12. The red area indicates the result when choosing a very light bias regularisation (0.0001) and a bias FWHM of 60 mm as parameters in the SPM toolbox, and the blue area when having medium bias regularisation (0.01) and a bias FWHM of 120 mm.

A clear difference in the complete segmentation of the primary tissue types for the two situations mentioned above is observed in Fig. 3. Significantly more accurate tissue segmentation is achieved when taking into account the intensity modulation artifact (choosing lighter bias regulation). How-

ever, as previously emphasized, improved tissue segmentation is achieved at the cost of little to no air segmentation. Thus, a compromise between accurate soft tissue and bone segmentation or increased air segmentation must be made when applying the segmentation algorithm found in SPM12.

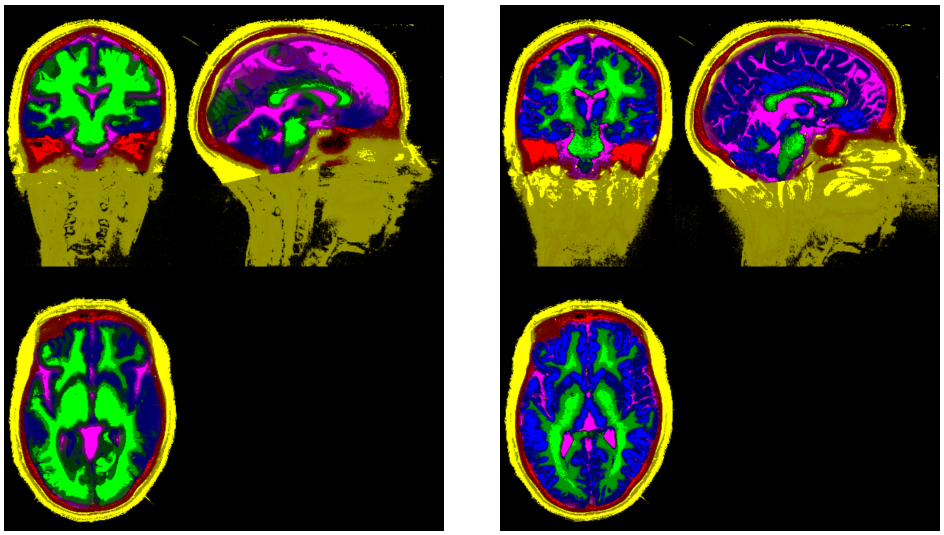

(a) (b)

Figure 3: The resulting segmentation of soft tissue (yellow), bone(red), cerebrospinal fluid(violett), grey matter(blue), and white matter(green) obtained when using medium bias regularisation (0.01) with a bias FWHM of 120 mm (a) and when using very light bias regularisation (0.0001) with a bias FWHM of 60 mm (b).

D Scaling of UTE Data

UTE image was acquired in addition to anatomical MP-RAGE image to achieve better air segmentation. Equal spatial resolution and volume position was set for both imaging sequences to obtain spatial correspondence between the images acquired with the two different sequences. Fig. 4a indicates the reconstructed image from the MP-RAGE (grayscale) and the UTE (redscale) sequence where the distortion correction of the gradients was turned off. The scaling of the UTE image is apparent where the anatomical features in the image are enlarged. As a consequence, correct segmentation of air could not be achieved with the acquired image. The reason for the observed scaling in the UTE images is unknown. However, a re-scaling of the image was performed by changing the value of the isotropic resolution from 0.75 mm to 0.725 mm in the DICOM header of the UTE image.

The resulting image with modified resolution overlaid onto the unchanged MP-RAGE image is indicated in Fig. 4b. A significant improvement in the geometrical correspondence between the images was observed. The same improvement was seen throughout the imaging volume. Thus, the UTE image with a modified DICOM head file can be used for air segmentation due to the adequate correspondence of the position, shape, and size of the structures in the human brain with the structural MP-RAGE image. Small differences are still observed in the alignment between the MP-RAGE and the UTE image at the nose's tip and back of the head.

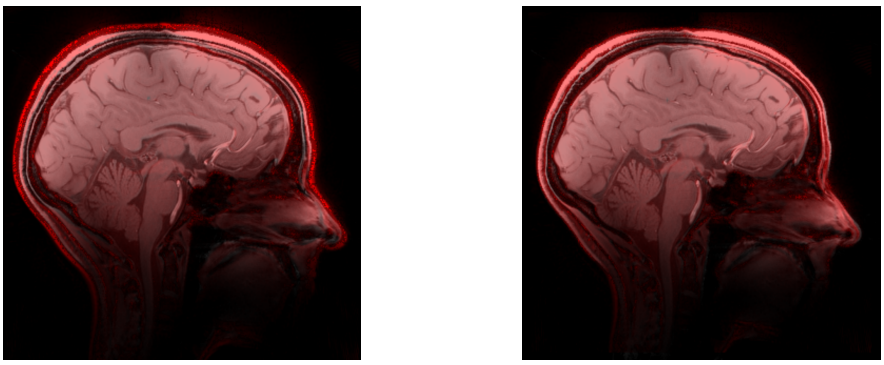

(a) (b)

Figure 4: (a) Obtained UTE image (redscale) overlaid on anatomical MP-RAGE image (grayscale). (b) Rescaled UTE image with changed resolution overlaid on the anatomical MP-RAGE image, which is unchanged.

E Double Versus Single Precision

The values of resolution and FOV that can be used for the input susceptibility map in the Fourier-based model are limited mainly by available computational memory. However, the model wishes to have high resolution and FOV so that discretization and aliasing effects are minimized in the model results. Defining and calculating the induced frequency offset on matrices with single precision takes significantly less computational memory than using matrices with double precision. Using single precision matrices can allow the model to choose higher FOV and/or higher resolutions. The difference in the results of using single versus double precision when simulating the frequency offset with the model in this thesis is presented in Fig. 5. The values were calculated with a matrix of size $450 \times 450 \times 450$, and the results are given in Hz. No clear visual difference is observed between the two results obtained by the matrices with different precision. When evaluating the difference between the results attained using a matrix of single and double precision, insignificant differences are observed on the order of 10^{-4}. Thus, matrices of single precision can be used in the model without significantly affecting the precision of the obtained results.

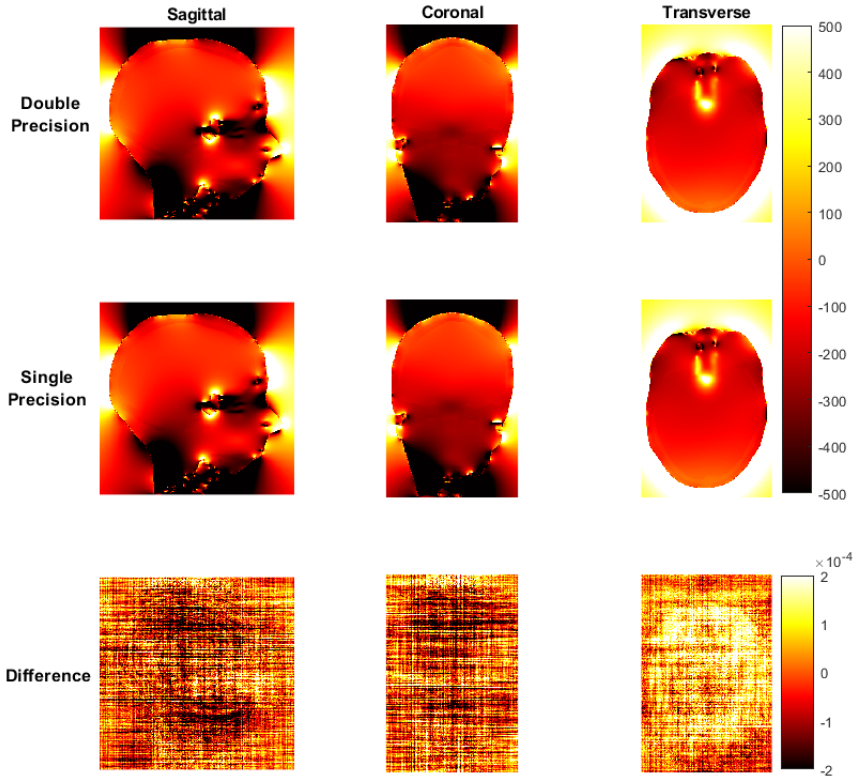

Figure 5: Calculated frequency offset given in Hz obtained from a Fourier-based method. The top row indicates the results when using a matrix of double-precision, the middle row when using a single-precision, and the bottom row indicates the difference between the results from double and single precision.

Using single precision matrices allows the model to define the segmented brain on a matrix of greater size, giving the possibility to increase the FOV and/or the spatial resolution of the susceptibility map. Both parameter changes benefit the model's accuracy as it is sensitive to aliasing and discretization effects. The effect on the calculated frequency offset when increasing the effective FOV is indicated in Fig. 6, where each row shows the obtained results in the sagittal, coronal and transverse image plane, respectively. In addition, the measured frequency offset from a field

map (FM) sequence with Tune-Up shim mode is also indicated. By visual inspection, a better resemblance between the simulated frequency offset and the values in the experimental data is observed when the initial susceptibility map was padded onto larger matrix sizes (MS), effectively increasing the FOV. The results from the matrix with size 340 show an apparent aliasing effect within the anatomical parts of the subject at each dimension of the calculation volume. As observed in Fig. 6, the aliasing effect is greatly removed by increasing the matrix size. The greatest improvement is observed when changing the isotropic matrix size from 340 to 450. However, a slight improvement was also observed when increasing the matrix size from 340 to 570 in the area close to the superior parts of the frontal lobe.

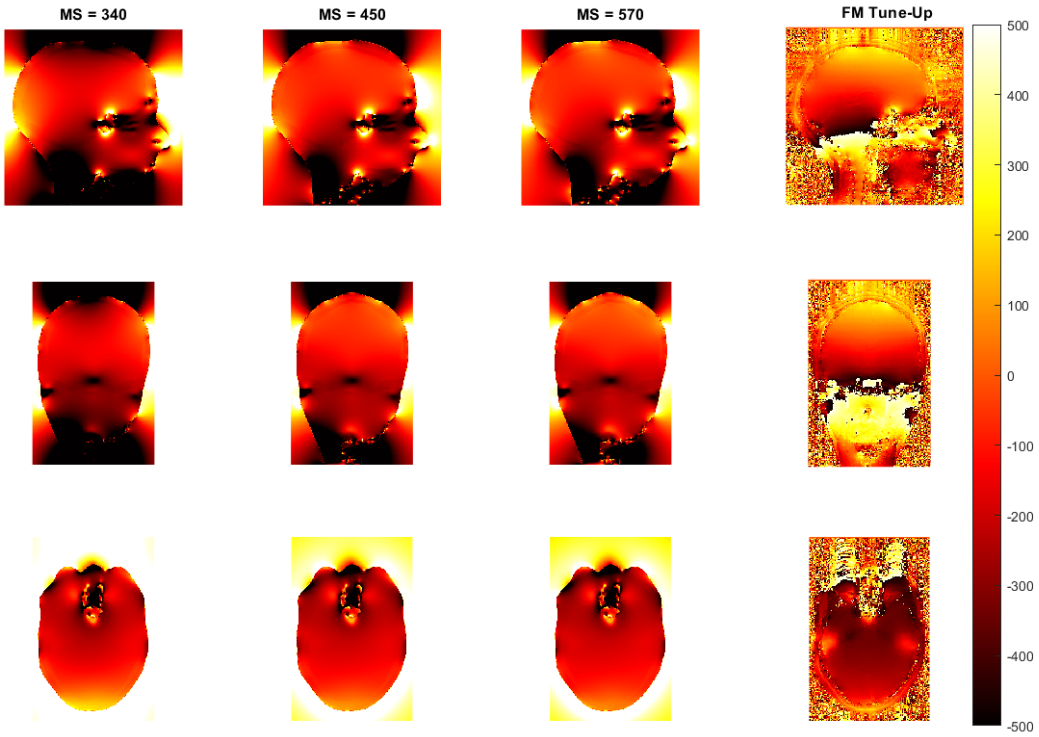

Figure 6: Calculated frequency offset given in Hz obtained from a Fourier-based method when defining the susceptibility map on a uniform matrix with a FOV of 255 mm (MS = 340), 337.5 mm (MS = 450) and 427.5 mm (MS = 570), respectively. In addition, the measured frequency offset from a field map sequence with Tune-Up shim mode is indicated. MS is used as an abbreviation for matrix size.

To conclude, using single precision for the matrices in the model gives the possibility to significantly increase their achievable matrix size, resulting in the advantageous opportunity to minimize the presence of the aliasing effect in the obtained results by increasing the effective FOV. Using single precision can also provide the possibility to significantly increase the spatial resolution of the matrix on which the susceptibility map is described. Increasing the spatial resolution will effectively decrease the discretization effects in the obtained results from the model. However, the improvement achieved by changing resolution is not illustrated, as the resolution is unchanged for the simulation performed in this thesis.

F Testing and Validating the use of a Sinc- and a Gaussian-corrected Signal Decay Function to Map $G_{z,s}$ in a Phantom Measurement

The quantitative measure of through-slice susceptibility-induced gradients, $G_{z,s}$, can be performed by fitting the experimental data from a ME-GRE scan onto a corrected signal decay function. A corrected signal decay function, where a rectangular slice profile was assumed, is given in Eq. 2.10. However, a perfect rectangular slice profile will, in reality, not be achievable due to physical constraints, and the actual slice profiles will have a more bell shape with a tail at the edges. The bell-shaped slice profile will be more prevalent at high resolutions. Thus, a non-linear least square fit was also made to a corrected signal decay function where a gaussian slice profile was assumed to see if it better represents the slice profile than the ideal rectangular function. The corrected signal decay function where a gaussian slice profile is assumed is then given by

$$I = I_0 \cdot exp\left(-\left(\gamma \cdot G_{z,s} \cdot TE \cdot \frac{\Delta z}{4 \cdot \sqrt{ln(2)}}\right)^2\right) \tag{1}$$

where γ is the gyromagnetic ratio, I_0 is the initial signal intensity at a time equal to zero, TE is the given echo time, and Δz is the full-width-half-maximum (FWHM) of the Gauss function, which here was assumed to be equal to the slice thickness (Deichmann, Josephs et al. 2002).

A ME-GRE sequence with standard shim mode was applied to a phantom with a homogeneous composition. An echo train with ten echo times ranging from 4 ms to 38.38 ms were used, and the spatial resolution for each voxel was 1 mm × 1 mm × 1 mm. In addition, a standard B0 shim mode was applied before the imaging acquisition. The obtained images at every third echo time are presented in Fig. 7.

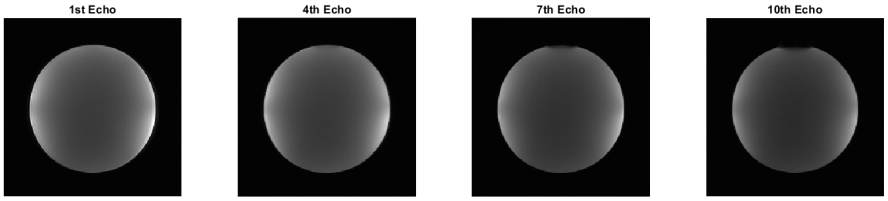

Figure 7: The images obtained at every third echo time from the ME-GRE scan.

A simple monoexponential curve fit of the experimental data was initially performed to the theoretical signal decay function given in Eq. 2.6, for two pre-defined ROIs, to estimate the T_2^* values. ROI1 was chosen in the center of the phantom where a homogeneous field is present, and ROI2 was selected in an area where enhanced signal loss had been observed (close to the surface of the phantom). The results of the estimated T_2^* values from the simple monoexponential fit are presented in Fig. 8. Noticeably more homogeneous distribution of T_2^* values was observed for the ROI taken at the center of the phantom, with a mean calculated value for T_2^* of 118 ms. The mean estimated T_2^*-value is reasonable and in the size order expected for the phantom used. In contrast, a relatively drastic decrease in the calculated T_2^* values was observed close to the phantom's surface. As the material inside the phantom is homogeneously distributed, the intrinsic T_2^* value of the material should be the same throughout the phantom. Thus, the observed signal decay indicates the presence of through-slice susceptibility field gradients ($G_{z,s}$), where its presence leads to an underestimation of the observed T_2^* values in the affected area when making a simple exponential fit of the measured data with Eq. 2.6.

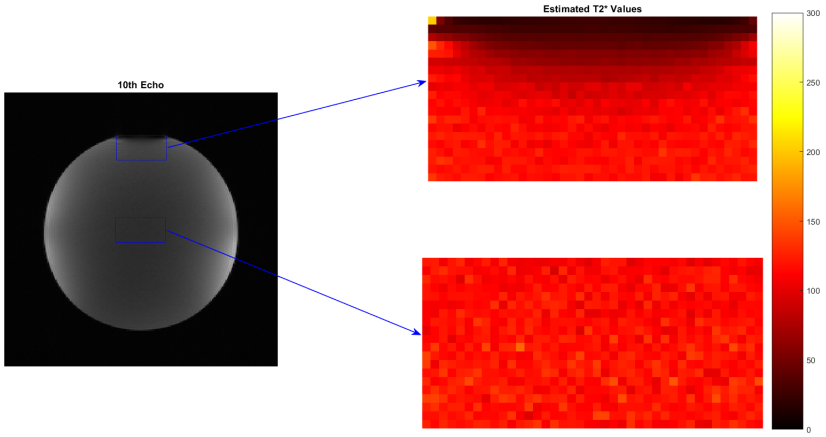

Figure 8: Magnitude image acquired at the 10th echo, together with the calculated T_2^* maps for an area where a signal loss was observed and an area with an approximately homogeneous field. The T_2^* maps are given in ms.

After the value of T_2^* for the phantom was estimated, a non-linear least-square curve fitting of the experimental data to the two corrected signal decay functions and the simple monoexponential decay function was performed for a voxel with a homogeneous field (voxel 1) and one where an induced signal loss was observed (voxel 2). The value of T_2^* was fixated to the mean calculated value T_2^* evaluated over ROI1 for the model fits the corrected signal decay functions. Table 1 presents the RMSE and the R^2 of the different fits made for the two voxels. High goodness-of-fit statistics are shown for most of the performed fits, and the slightly higher RMSE values for voxel 2 are as expected due to its location closer to the phantom's surface. However, worse goodness-of-fit statistics are observed for the monoexponential fit for voxel 2, indicating how the theoretical model for signal decay has limitations in following the signal evolution in a voxel experiencing field inhomogeneity. Insignificant differences were observed in the performance between the sinc- and gaussian-corrected signal decay functions. These results are further highlighted in Fig. 9, and 10, illustrating the curve fits in a single voxel located in ROI1 and ROI2, respectively. The corrected signal decay functions follow the experimentally measured data points noticeably better in voxel 2, where they are able to follow the small shoulder region observed for the first echo times. In contrast, it is clearly observed how the monoexponential curve fit is not able to follow the features of the experimental data points in the given region.

Small oscillations of the measured data points become visual in the narrowed area indicated in Fig. 9b, 9d and 9f. The oscillation in the signal intensity with time seems to be mainly due to a systematic error. In addition, the data points show an unexpected plateau region for the first three echo times before the signal begins to decay in intensity. The same features are most likely present for the voxel in ROI2 but are not visual due to the rapid signal decay induced by $G_{z,s}$. The cause of the noticed properties with the measured data is yet unknown. However, the magnitude of the oscillations is small and does not seem to affect the quality of the fits greatly.

Table 1: The RMSE and R^2 value for the three different fits in a single voxel located in ROI1 and ROI2.

Fit type	**Voxel 1**		**Voxel 2**	
	RMSE	R^2	RMSE	R^2
Sinc-corrected	9	0.96	20	0.99
Gaussian-corrected	9	0.96	22	0.99
Uncorrected (monoexponential fit)	9	0.96	78	0.93

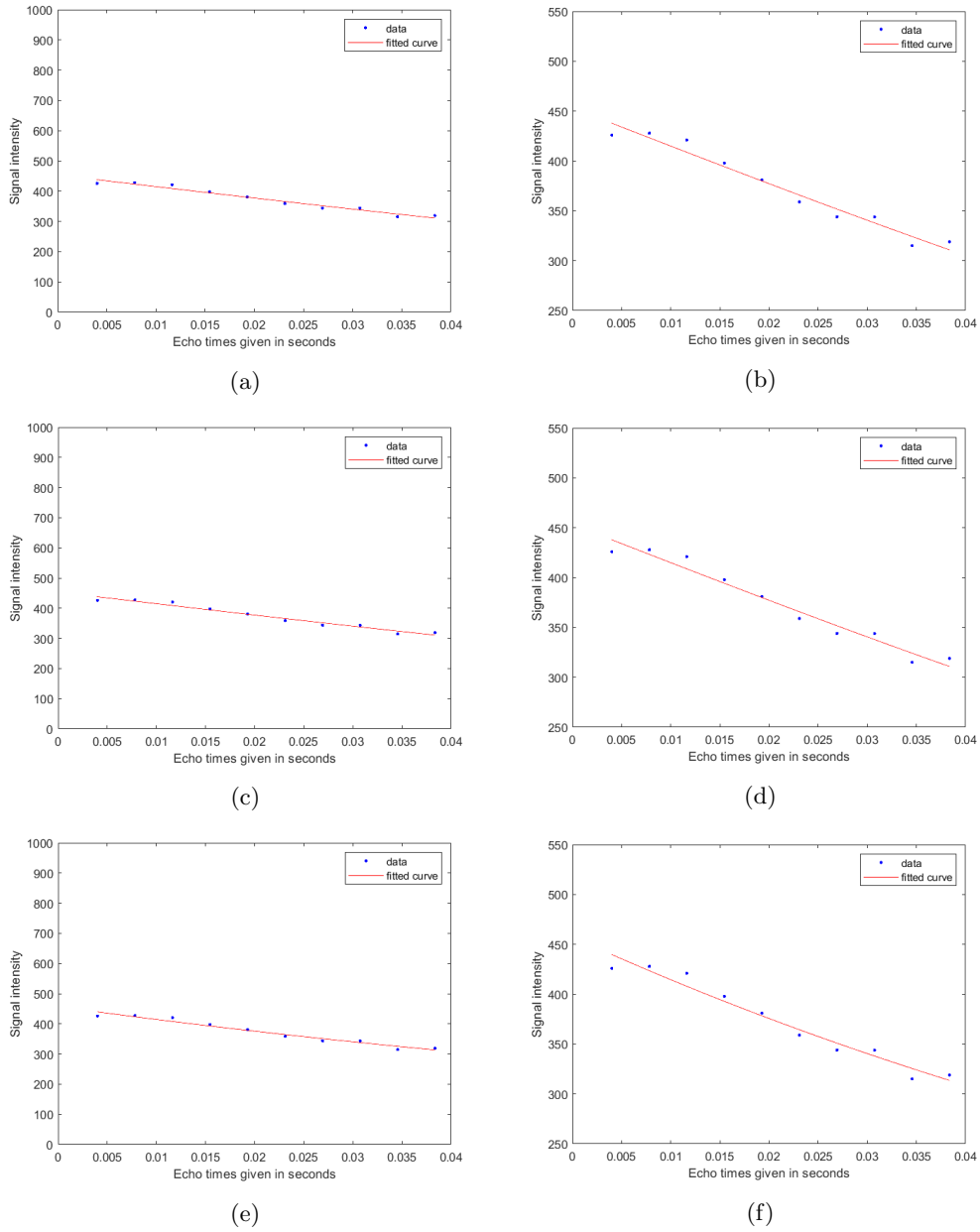

Figure 9: The three images indicate the curve fit of the experimental data onto a sinc-corrected (a-b) and a gaussian corrected (c-d) signal decay function, in addition to the fit made onto a simple monoexponential decay function (e-f). The curve fit is performed for a voxel in ROI1 where a homogeneous field is assumed.

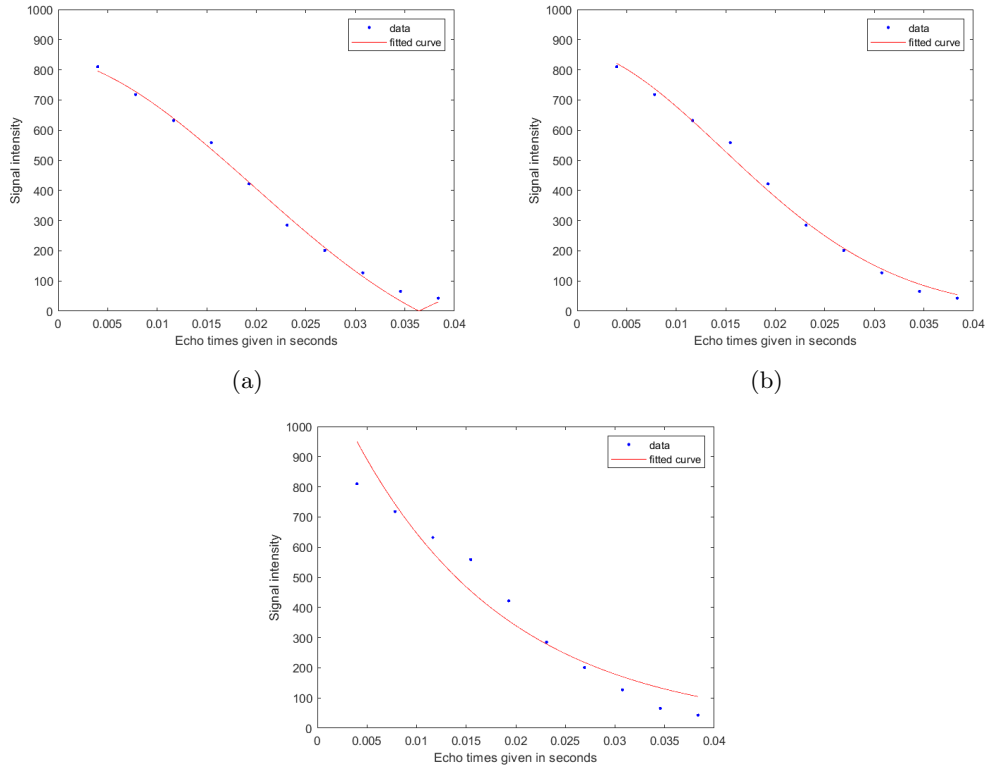

Figure 10: The three images indicate the curve fit of the experimental data onto a sinc-corrected (a) and a gaussian corrected (b) signal decay function, in addition to the fit made onto a simple monoexponential decay function (c). The curve fit is performed for a voxel in ROI2 where enhanced signal loss is present.

The quantification of $G_{z,s}$ was achieved within ROI1 and ROI2 by performing the model fit to the corrected signal decay functions with T_2^* fixated, over the entire regions. The results of the $G_{z,s}$ maps are indicated in Fig. 11a and 11b for the situation where a rectangular and a gaussian slice profile are assumed, respectively. The resulting maps of estimated $G_{z,s}$ values in ROI2 showed a pattern similar to the observed enhanced signal loss seen in the experimental measurements. The highest quantified $G_{z,s}$ values in ROI2 are located in the areas where the strongest signal loss was observed. In addition, relatively weak susceptibility gradients were estimated in ROI1. The mean value of the goodness-of-fit statistics are indicated in Table 2, and show noticeably good values for both performed fits. No significant difference is observed between the two model fits, for both ROI1 and ROI2, indicating that the models seem to operate equally well. A minor difference was observed in ROI2, where a slightly better R^2 value was observed for the sinc-corrected model fit. The superior goodness-of-fit statistics implies that the corrected signal decay functions, accounting for the presence of $G_{z,s}$, represent the system properly and can thus be used to quantify the presence of $G_{z,s}$ if the T_2^* value of the tissue is known.

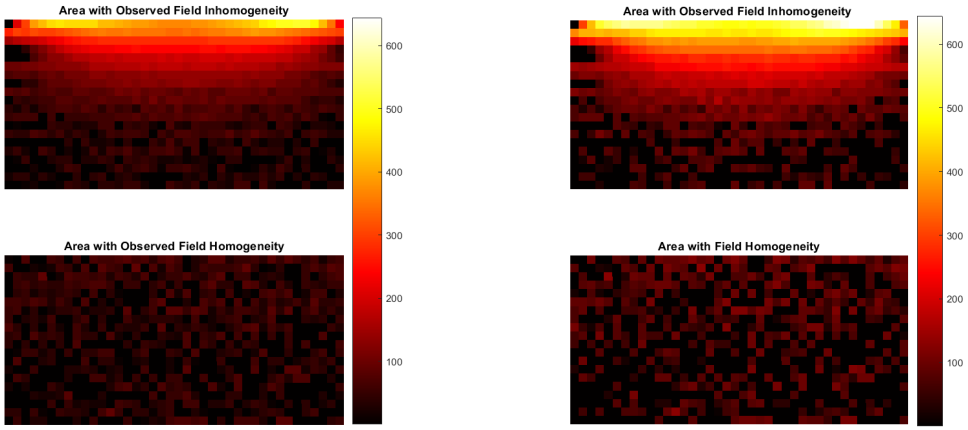

(a) (b)

Figure 11: Calculated $G_{z,s}$ maps for an area with observed signal intensity and an area with an approximately homogeneous field. (a) indicates the estimated $G_{z,s}$ values from fitting the data onto a gaussian-corrected signal decay, whereas (b) indicate the values of $G_{z,s}$ from the fit to the sinc-corrected signal decay. The values of $G_{z,s}$ is given in μT/m.

Table 2: The mean value of the RMSE and R^2 values for the two different fits made to corrected signal decay functions in ROI1 and ROI2.

Fit type	**ROI1**		**ROI2**	
	RMSE	R^2	RMSE	R^2
Sinc-corrected	10	0.94	14	0.97
Gaussian-corrected	10	0.94	14	0.96

By qualitative analysis of Fig. 11 slightly higher values of $G_{z,s}$ seem to be estimated for the sinc-corrected model fit compared to the gaussian-corrected model fit. This was further observed in both ROIs when looking at the histogram plots of the estimated $G_{z,s}$-values, shown in Fig. 12 and 13, for the gaussian- and sinc-corrected model fits, respectively. The distribution of estimated $G_{z,s}$ values reaches a maximum of 90 μT/m for the gaussian-corrected model and 130 μT/m for the sinc-corrected model in ROI2. In addition, the estimated values of $G_{z,s}$ for both regions and model fits are observed to be of reasonable size. Relatively low values of $G_{z,s}$ are observed for bot fits in ROI1, where a value of zeros has been estimated for the majority of the voxels.

The sinc-corrected model fit has a noticeably higher amount of voxels with a quantified value of $G_{z,s}$ equal to zero. However, an unexpected bell-shaped distribution of higher $G_{z,s}$ values was observed in ROI2. The same feature, but less apparent, was also seen for the histogram plots for ROI2, indicating that it is most likely a systematic error either in the models or the experimental data.

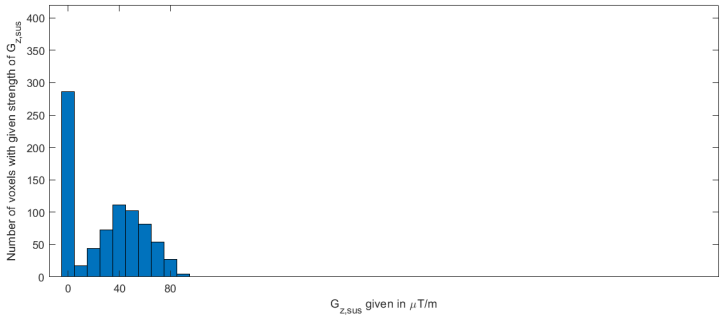

(a)

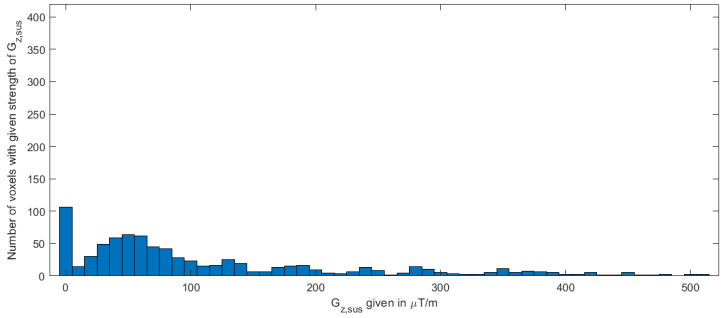

(b)

Figure 12: Histograms indicating the number of voxels with a given values of the estimated $G_{z,s}$ for ROI1 (a) and ROI2 (b) by fitting the data to a gaussian-corrected signal decay function. The values of $G_{z,s}$ are given in $\mu T/m$.

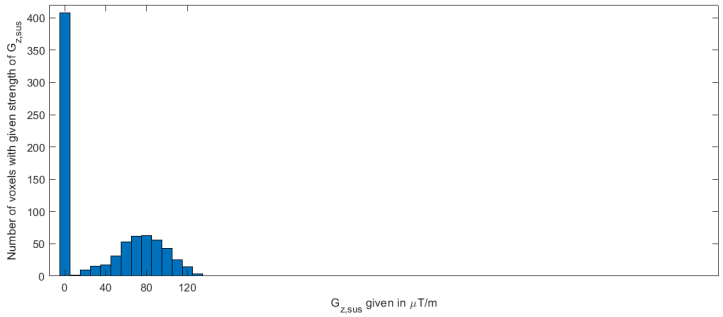

(a)

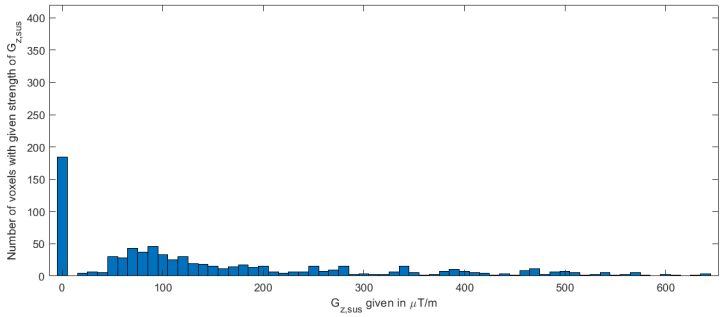

(b)

Figure 13: Histograms indicating the number of voxels with a given value of the estimated $G_{z,s}$ for ROI1 (a) and ROI2 (b) by fitting the data to a sinc-corrected signal decay function. The values of $G_{z,s}$ are given in $\mu T/m$.

Despite the observed unexpected trends in the results, the main features are as expected. In addition, the models have significantly high goodness-of-fit statistics, indicating that the models describe the signal evolution for the given system well and can be used to estimate the presence of $G_{z,s}$. Only minor differences were observed in the performance of the sinc- and the gaussian-corrected signal decay functions in modeling the experimentally measured data. The relatively similar performance on the fit to the data is most likely due to the small slice dimension chosen. As previously mentioned, a perfectly rectangular slice profile cannot be achieved, and the slice profile will become more and more similar to a gaussian function for higher resolutions (smaller voxel dimensions). As a relatively high spatial dimension in the slice-direction is used, the true slice profile is most likely strongly bell-shaped, which can explain why the gaussian-corrected signal decay model seems to operate equally as well as the sinc-corrected signal decay model.

For later measurements performed in this thesis, a high in-plane resolution and a lower through-slice spatial resolution will be used to ensure that the through-slice susceptibility-induced gradients are the dominant effect on the signal modulation compared to the presence of in-plane susceptibility-induced field gradients. A larger slice thickness will make the assumption of a rectangular slice profile more reasonable than a gaussian slice profile. Therefore, the sinc-corrected signal decay function will be used to estimate and quantify the presence of $G_{z,s}$ in the further ME-GRE measurements.

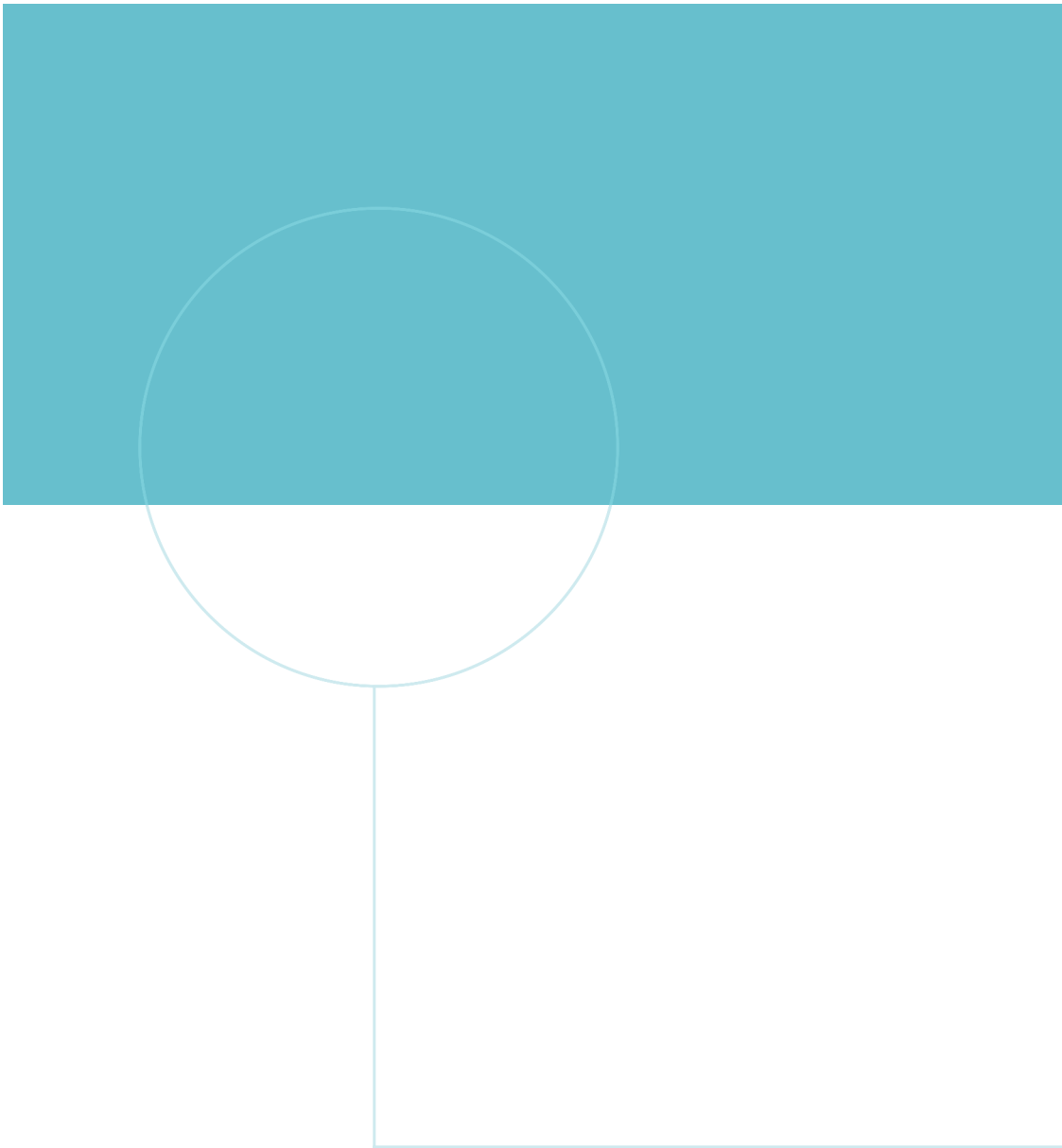

NTNU

Norwegian University of
Science and Technology